DIPLOMA THESIS

NANOINDENTATION OF ULTRAFINE GRAINED AND SINGLE CRYSTALLINE CHROMIUM AND TANTALUM AT ELEVATED TEMPERATURES

Josef Pörnbacher

Adviser
Assoc. Prof. Dr. Daniel Kiener
Montanuniversität Leoben, Austria

Co-Adviser
Assoc. Prof. Dr. Peter Hosemann
University of California, Berkeley, USA

This work has been carried out at the Department of Materials Physics, Montanuniversität Leoben, Austria, in cooperation with the Department of Nuclear Engineering, University of California, Berkeley, USA

September 29, 2015

Eidesstattliche Erklärung

Ich erkläre an Eides statt, dass ich diese Arbeit selbstständig verfasst, andere als die angegebenen Quellen und Hilfsmittel nicht benutzt und mich auch sonst keiner unerlaubten Hilfsmittel bedient habe.

Affidavit

I declare in lieu of oath, that I wrote this thesis and performed the associated research myself, using only literature cited in this volume.

_____

September 29, 2015 Josef Pörnbacher

Acknowledgements

Foremost, I would like to express my deepest gratitude to my supervisor Assoc. Prof. Daniel Kiener for giving me the opportunity to write this work on the Department of Materials Physics, his strong encouragement to independently scientific work and his strong support and advice during the whole course of this work.

I am of course deeply grateful to the entire Erich-Schmid-Instiute. My special thanks goes to Dr. Verena Maier for providing her professional knowledge in nanoindentation, Dr. Stefan Wurster and Dr. Anton Hohenwarter for their great advice during the sample preparation time in Leoben, Silke Modritsch for her technical assistance and my close friends Raphael Esterl and Dipl.-Ing. Alexander Leitner for countless discussions and their encouraging attitude.

Needless to say, I am highly obliged to Assoc. Prof. Peter Hosemann for the opportunity to use the nanoindentation system at the Department of Nuclear Engineering at UC Berkeley and his scientific advice. Moreover, I consider it an honor to have worked within his group. I am especially grateful to Dr. Manuel Abad for the strong technical support at the nanoindenter and David Frazer, Ashley Reichardt and Hi Tin Vo for their assistance at the FIB facility.

Finally, I want to deeply thank the Austrian Marshall Plan Foundation for their generous financial support without this work could not have been realized.

Abbreviations and Symbols

A_{proj}	projected area
ARB	accumulative role bonding
b	Burgers vector
bcc	base centered cubic
BSE	back scattered electrons
c	concentration
c^*	constraint factor
C_f	frame compliance
cg	coarse grained
C_{total}	system compliance
D	diffusion coefficient
d_G	average grain size
DSI	depth-sensing indentation
E	Young's modulus
EBSD	electron back scattered diffraction
ECAP	equal channel angular pressing
E_a	activation energy for diffusion
E_r	reduced modulus
fcc	face centered cubic
H	hardness
h	(indentation) depth
H_0	macroscopic hardness
h_c	contact depth
h_{el}	elastic depth
h_{max}	maximum depth
h_{pl}	plastic depth
ISE	indentation size effect

k	Hall-Petch strengthening coefficient
k_B	Boltzmann constant
m	strain rate sensitivity
nc	nanocrystalline
P	load
Q_a	activation energy for deformation
R	universal gas constant
S	stiffness
SE	secondary electrons
SRJ	strain rate jump tests
SRS	strain rate sensitivity
sx	single crystal, single crystalline
T	absolute temperature
T_c	critical temperature
ufg	ultrafine grained
V^*	activation volume
ε	strain
$\dot{\varepsilon}$	strain rate
ν	Poisson's ratio
τ	shear stress
σ_0	critical flow stress (single crystal)
σ_f	flow stress
σ_y	yield strength

Abstract

Society's ever growing demands regarding the abilities and performances of products led materials scientists to explore new materials with outstanding properties. Ultrafine grained materials were subject to intense investigations over the last decades. This rose from the extraordinary characteristics, such as high strength, hardness and further functional features that type of materials offer. The objective of this works was to determine the mechanical behavior of less investigated body centered cubic materials, comparing ultrafine grained chromium and tantalum samples with their single crystalline counterparts, regarding their temperature dependent strength and deformation mechanism.

In order to test the mechanical properties of the different materials below and above their specific critical temperature, nanoindentation tests were conducted at room temperature and at up to 300 °C. The resulting indents were investigated by means of atomic force microscopy mode analysis and light microscopy for pile-ups and sink-ins. The actual measurement procedure was load controlled and based on a load and partial unload principle, which enables the determination of hardness and Young's modulus at several different depths for one indent. These data were fitted with the Nix-Gao model for the indentation size effect, yielding macroscopic hardness and internal length scale values. The macroscopic hardness was further compared with microhardness tests and results from a different nanoindentation system. The ultrafine grained material, both owning an average grain size of ≈ 100 nm, exhibited hardness increases by a factor of 3.5 - 4 at room temperature compared to the single crystals.

Tantalum samples of both microstructures exhibited a significant hardening phenomenon at 250 °C and above. Cross sections of the according indents were made using a focused ion beam workstation and examined by scanning electron microscopy to obtain possible oxide growth. Since no significant oxygen layer was found, a theoretical model was developed proposing oxygen diffusion and solid solution hardening as cause for the phenomenon, which describes the experimental data well.

Except for the described tantalum hardening, hardness decreased with increasing temperature. While the hardness of ultrafine grained material further decreased between the assumed critical temperature of approximately 200 °C and 300 °C, the single crystalline sample exhibited no further hardness decrease.

Load displacement data were also used to analyze incipient plasticity in the case of the single crystals. The shear stress at the onset of plasticity was calculated to be a significant fraction of the theoretical shear stress. Due to the pronounced distribution, however, it was concluded that several mechanisms such as homologous and heterogeneous dislocation nucleation or activation of preexisting dislocations might be accountable.

Creep tests were conducted to obtain strain rate sensitivity and activation volume, both feasible parameters to investigate the governing deformation mechanism. Whereas the strain rate sensitivity at room temperature was found to be significantly decreased for the ultrafine grained materials (≈ 0.01) compared to the single crystals (≈ 0.05), the activation volume was similar (≈ 10 b^3). This activation volume range is linked to the predominance of the kink-pair nucleation, typical for bcc metals. At 100 °C the strain rate sensitivity decreases for the single crystals, whereas it is raised for the ultrafine grained samples. This was assumed to be the result of diminishing contribution from the Peierls stress in terms of the single crystal, and additionally, the increasing importance of grain boundary contributions in terms of the ultrafine grained sample. However, at 200 °C and above results are assumed to be influenced by thermal drift, exacerbating conclusions from these creep tests.

Kurzfassung

Der Wunsch nach immer weiter verbesserten und leistungsgesteigerten Produkten veranlasst die Materialwissenschaft zur Erforschung neuer Werkstoffe mit herausragenden Eigenschaften. Ultra-feinkörnige Materialien sind aufgrund ihrer Vorzüge im Bereich Festigkeit, Härte und weiteren funktionalen Eigenschaften in den letzten Jahrzehnten intensiv erforscht worden. Das Ziel der vorliegenden Arbeit ist, die Charakterisierung der mechanischen Eigenschaften von wenig untersuchten kubisch-raumzentrierten Materialien. Dazu wurde die Temperaturabhängigkeit von Härte und dominierenden Verformungsmechanismen von ultra-feinkörnigem und einkristallinem Chrom und Tantal verglichen.

Zur Erhebung der mechanischen Eigenschaften unter- und überhalb der spezifischen kritischen Temperatur wurden Nanoindentierungsversuche zwischen Raumtemperatur und 300 °C durchgeführt. Die Form der Indents wurden mittels Rasterkraft- und Lichtmikroskop auf Pile-ups und Sink-ins untersucht. Das Messverfahren selbst beruht auf einem Belastungs- / partielle Entlastungs- Schema, um für einen Indent mehrere Härte und Elastizitätskonstanten zu erhalten. Diese werden anschließend mit Hilfe des Nix-Gao Modells analysiert, um die charakteristischen Größen makroskopische Härte und interne Längenskala für den Indentierungs-Größeneffekt zu erhalten. Diese Ergebnisse wurden weiters mit Ergebnissen von Vickers-Härteprüfung und einem weiteren Nanoindenter verglichen. Beide ultrafeinkörnigen Materialien, bei denen sich eine durchschnittliche Korngröße von ca. 100 nm durch Hochdruck-Torsionsverformung eingestellt hatte, zeigten eine rund 4-fache Steigerung der Härte bei Raumtemperatur verglichen mit den Einkristallen.

Tantalproben beider Mikrostrukturen zeigten ein signifikantes Aufhärtungsverhalten ab Temperaturen von 250 °C. Mittels Rasterionenmikroskop hergestellte Indentquerschnitte zeigten allerdings kein auffälliges Wachstum der natürlichen Oberfläschenoxidschicht der entsprechenden Proben. Deshalb wurde ein theoretisches Modell, basierend auf Sauerstoff-Diffusion und anschließender Mischkristallhärtung, entwickelt, welches sowohl die Temperatur- als auch die Zeitabhängigkeit der experimentell gefundenen Aufhärtung sehr gut beschreibt.

Bei allen anderen Proben zeigte sich der erwarteten Härteverlust bei erhöhten Temperaturen. Während die Härte des ultrafeinkörnigen Materials zwischen der kritischen Temperatur und 300 °C weiter sank, wurde keine weitere Reduktion bei einkristallinem Material gefunden.

Last-Verschiebungskurven wurden verwendet, um das Einsetzten von Plastizität von einkristallinen Materialien zu untersuchen, wobei sich zeigte, dass die dazu nötige Scherspannung einen signifikanten Teil der theoretischen Festigkeit ausmacht. Durch die Streuung der Werte wird vermutet, dass verschiedene Mechanismen wie, homogene und heterogene Versetzungsnukleation oder Versetzungsaktivierung, beigetragen haben.

Um die dominierenden Versetzungsmechanismen zu evaluieren wurden mittels Kriechversuchen Dehnratenempfindlichkeit und Aktivierungsvolumen erhoben. Es zeigte sich bei Raumtemperatur eine stark verminderte Dehnratenempfindlichkeit für die ultrafeinkörnigen Materialien (≈ 0.01), verglichen mit den einkristallinen Proben (≈ 0.05). Das Aktivierungsvolumen blieb allerdings für beide im Bereich von 10 b^3, welches mit der Dominanz des Kinkenpaarmechanismus verbunden wird. Bei 100 °C wurde eine Senkung der Dehnratenempfindlichkeit für einkristallines Material gefunden, während jenes der ultrafeinkörnigen Proben anstieg. Dies wird auf einen sinkenden Beitrag der Peierlsspannung zur Fließspannung im Fall des einkristallinen Materials zurückgeführt, während beim ultrafeinkörnigen Material der Zuwachs durch Korngrenzprozesse überwiegt. Ab 200 °C zeigte sich ein starker Einfluss durch thermischen Drift, wodurch eine sichere Interpretation der Ergebnisse bezüglich Dehnratenempfindlichkeit erschwert wurde.

Table of Contents

1 Introduction

Nowadays, metals and their properties are well understood since most of the underlying physical mechanisms have been ascertained. With this knowledge, it is possible to customize them so that their properties can be adapted to their application demands. There are for example many different ways to improve or alter the mechanical properties of metals. This is often connected to at least a certain degree of using alloying elements such as it is the case for solid solution or dispersion hardening. Different to that, work hardening is not in need of any alloying system to work, but is otherwise well known to cause embrittlement of the material which is subjected to it. Therefore a subsequent annealing process is usually applied to increase the ductility. However, the only known technique to increase mechanical properties such as hardness and strength and not in general causing reduced ductility, is grain refinement [1]. This is usually achieved by either applying a fast cooling rate to solidify melts, or by recrystallization through deformation and heat treatment. A more novel technique leading to a wider horizon in terms of accessible grain sizes and therefore properties and applications is severe plastic deformation (SPD). Before it came up in the early 1990s [2], the only chance to produce ultrafine grained (< 1000 nm), or even nanocrystalline materials (< 100 nm) was powder consolidation with all its drawbacks such as residual porosity, impurities from ball milling etc.

Since then ultrafine grained (ufg) and nanocrystalline (nc) materials have been subject to numerous scientific studies focused on revealing their unique properties. Besides the mentioned outstanding strength potential of ufg materials, diverse studies revealed also interesting properties in terms of conductivity, magnetic properties [2], radiation tolerance [3, 4] etc. One of the most interesting questions which has arisen, is about the dominating deformation mechanisms. While for face-centered cubic (fcc) materials a significant body of research is available the knowledge about those of body-centered cubic (bcc) and hexagonal close-packed (hcp) materials is still not as extensive [5]. However, it is known that the high Peierls potential leads to a thermal part of the flow stress which can be activated by temperature. This part is decreasing with temperature and vanishes at a material specific critical temperature T_c. While under T_c the deformation mechanism of bcc single crystalline (sx) and coarse grained (cg) material is believed to be dominated by the motion of screw

dislocations through the kink-pair mechanism [6], for ufg material there might be further contributors [7]. Furthermore, due to the expiring influence of the Peierls potential above T_c, the mechanisms, dominating plastic deformation at elevated temperatures, are expected to be different as well.

In order to determine the mechanisms governing the plastic deformation, material properties such as the strain rate sensitivity (SRS) or the activation volume (V^*) are often considered. These are time-dependent and are thus well suited to obtain limiting steps in the process of plastic deformation. These quantities can be determined by different testing methods and especially nanoindentation became a very popular technique to access them. This is due to several reasons such as the ability of probing very small volumes and therefore gaining a large number of data for limited test sites. The possibility of automatizing the testing procedure as well as the simultaneous measurement of indentation depth and time make it a favorable technique to obtain time dependent values.

Since the difference between coarse grained or even single crystalline materials compared to ufg materials is of special interest, one focus of this work is to compare the mechanism of plastic deformation for these types of microstructures. Another aspect will be the determination and comparison of the hardness of these materials. The single crystalline materials used in this work potentially show further interesting properties such as the indentation size-effects (ISE) which will be discussed later in detail. Furthermore these experiments are not only conducted at room temperature. But in order to test the metals below and above their T_c, at several elevated temperatures as well.

2 Theoretical Background

2.1 Mechanical Properties of Single Crystalline and Ultrafine Grained Body-centered Cubic Materials

Mechanical properties such as hardness, strength and ductility of crystalline materials (e.g. metals) at a given temperature are governed by different distinctive features. Besides others, these are primarily the chemical composition (i.e. the element or alloy) and the microstructure. Both are affecting the movability of dislocations, which are linear lattice defects and the major source of crystal plasticity, in different ways. When two or more different sorts of atoms form an alloy, solid solutions are built which lead to an elastically distorted lattice of the crystal. The interaction between the lattice's and the dislocation's area of distortion is affecting the mobility of the dislocation. However, the microstructure, on which the focus is put in this work, describes the size, shape and arrangement of grains in a polycrystalline material. The boundaries between the grains display severe obstacles for the movement of dislocations [1]. This is obviously the case when different grains with grain boundaries are present, but is not the case for single crystalline material, which consist only out of a single grain. The properties of a single crystal are thus mainly governed by the mentioned chemical composition and additionally the density of dislocations.

2.1.1 Hardness and Yield Strength

Presumably the most used parameter for the description of materials is the hardness. This is due to the fact that it can be easily obtained by cheap standardized measuring procedures such as microhardness testing as for instance Vickers, Brinell or Rockwell hardness testing. The mathematical definition of the hardness is the ratio between the maximum load of an indenter P_{max} and the area A of the created indent after a specified dwell time as shown in Eq. (1). Hence it allows a fast comparison of different materials which were tested at similar conditions [8].

$$H = \frac{P_{\max}}{A} \tag{1}$$

It needs to be said that different techniques of hardness testing observe different projected areas based on their measurement principles. Whereas conventional microhardness testing methods such as those mentioned above are usually equipped with an optical microscope to determine the residual imprint of the indent after unloading, modern nanoscale testing techniques such as nanoindentation (see chapter 2.4) measure load displacement curves and derive the projected contact area from the unloading slope.

Another commonly used parameter describing the strength of a material is the yield strength σ_y. This is the stress which needs to be applied to introduce plastic flow, or, more specifically, to move dislocations. The flow stress σ_f is the strength of a material at a given strain. Both are commonly determined by tensile or compression yield tests. The mentioned parameters are correlated by the constraint factor c^*such as shown in Eq.(2) [9].

$$c^* = \frac{6_f}{H} \tag{2}$$

In practical use, a value of $c^* = 3$ is often applied, although the value is governed by the nature of deformation. The higher the ratio of Young's modulus to flow stress, the more plastic is the character of the deformation. To take that into consideration, Johnson [10] suggested the distinctions in Table 1:

Table 1 : Overview of constraint factors for different characters of deformation.

• Fully elastic deformation		$c^* \leq$	1.07
• Elastic and plastic deformation	1.08	$< c^* <$	2.80
• Fully plastic deformation	2.80	$\leq c^*$	

Microstructural Influence

Grain refinement of crystalline materials leads to an enhanced flow stress. This behavior was, among others, investigated by Hall and Petch in the 1950s [11, 12]. Their proposed mechanism explains this behavior based on dislocation pile-ups at grain boundaries. These act, due to the orientation mismatch between the grains, as obstacles for dislocation movement. The relation between the flow stress and the grain size was found as shown in Eq.(3), where *k* is the

strengthening coefficient and σ_0 is the friction stress of the material, which includes contributions from solutes and particles but not from dislocations [13].

$$\sigma_y = \sigma_0 + \frac{k}{\sqrt{d_G}} \quad (3)$$

Since the hardness and strength of pure metals is mainly caused by microstructure and dislocation density, Eq.(3) leads to a considerably increased hardness and strength for ufg polycrystalline materials, compared to their chemically equivalent single crystalline or coarse grained counterparts. This is especially true when the measurement length scale is above a certain value, where no size effect (see chapter 2.1.4) for sx and cg material is occurring. While this equation was confirmed countless times for a broad variety of materials, its validity in the lower end of the accessible nanocrystalline regime (d_G ≈ 10nm) was discussed over the last decades [14, 15, 16]. For this grain size regime, a strength plateau or even a softening was reported. However, this is not of concern for this work, since the average grain size of the used samples is situated well above that (see chapter 3.5).

Cubic crystal lattices, such as bcc, show in general anisotropic behavior with a 90° symmetry. This means that materials properties of single crystals are changing with the lading angle, but reach the same values for steps of 90°. For randomly distributed grain orientations in polycrystalline materials, this effect is obviously compensated.

Temperature Influence

A single crystal containing no further defects (dislocations, impurity atoms, grain boundaries, etc.) possesses a specific flow stress, the intrinsic flow stress. When a dislocation moves, the atomic bonds to one adjacent crystallographic plane are stretched, those on the opposite plane are pushed together. This mechanisms demands energy, respectively stress. At a certain stress level the atomic bonds of the dislocation plane switch and the dislocation moves forwards by one atom spacing. The stress level needed to overcome this potential is called “Peierls stress” [1].

For crystal structures which possess dense packing, such as fcc and hexagonal systems with basal slip, the contribution of the Peierls stress to the entire flow stress is minor. For bcc sx and cg materials, however, the Peierls stress is a major contributor to the flow stress at low temperatures. On the other hand, the influence of this Peierls stress for polycrystalline bcc material is less pronounced compared to bcc sx material due to the contribution of grain boundary strengthening to the overall flow stress. According to that, the flow stress of bcc materials is often separated in an athermic part, which is primarily governed by microstructure

and solid solution hardening (for non-chemically pure materials), and an strongly temperature dependent thermal part which's dominant contributor is the Peierls stress [7].

If the stress applied is not sufficient to enable dislocations to overcome obstacles and move, thermal activation can provide the required energy. The probability p of a dislocation to overcome an obstacle by means of thermal activation is shown in Eq.(4).

$$p = \exp\left(-\frac{Q - 2 \cdot \lambda \cdot b \cdot d^* \cdot \tau^*}{k_\mathrm{b} \cdot T}\right) \tag{4}$$

The numerator in the exponential function represents the energy gap between obstacle potential Q and available work done by the movement of a dislocation. λ is the half obstacle spacing, b the dislocations Burgers vector, d^* the average width of the obstacle potential and τ^* is the effective stress on the dislocation. k_B is the Boltzmann constant and T the absolute temperature.

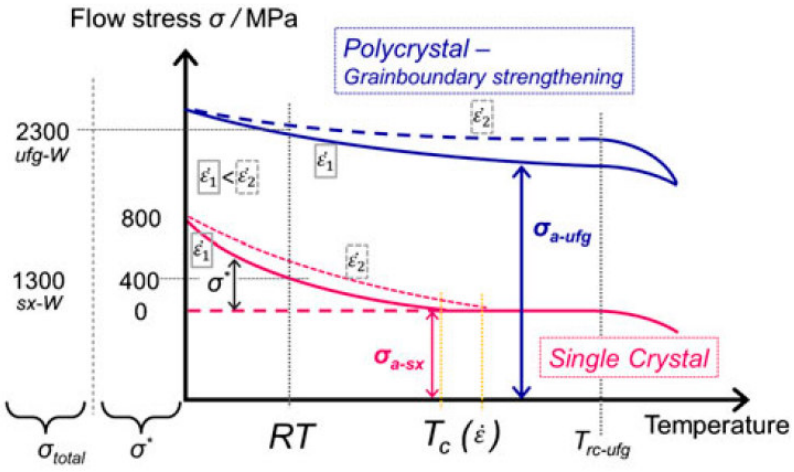

Fig. 2.1: Flow stress dependence of sx and polycrystalline tungsten as an example for the temperature dependence of bcc polycrystalline and single crystalline or coarse grained metals [17].

If the Peierls stress is assumed to be a special kind of barrier, its contribution to the overall flow stress is decreasing with increasing temperature and finally vanishing at a material specific critical temperature T_c [1]. An overview of this behavior for bcc sx and ufg material is shown in Fig. 2.1 for the case of tungsten [17]. For the single crystal the Peierls stress, σ', is strongly contributing to the overall flow stress at lower temperatures, though it vanishes at a strain rate dependent critical temperature, T_c ($\dot{\varepsilon}$). Above this temperature the single crystals flow stress is completely governed by its athermic part $\sigma_{a\text{-}sx}$. Because of the grain boundary strengthening, the Peierls stress plays a reduced role for the flow stress in terms of ufg materials. This is the reason for the predominance of the athermic part $\sigma_{a\text{-}ufg}$ in this case [17].

2.1.2 Young's Modulus

Hook's Law is relating mechanical stress σ with strain ε. The relation factor used is the materials constant Young's modulus E. This is a direct consequence of the interaction between the atoms in the crystal lattice and the assumption that a small displacement of atoms from its lattice position is reversible and the force needed to do so is in a linear relation to the displacement. It can be interpreted as the resistance of a material to elastic deformation.

Microstructural Influence

As mentioned for the strength above, the elastic properties of sx cubic materials are in general anisotropic as well. Otherwise there is no major influence of the microstructure on the Young's Modulus.

Temperature Influence

The Young's Modulus is corresponding to the curvature of the potential versus atomic spacing relation. For each temperature a certain equilibrium bonding distance between the atoms exists, which is increasing with temperature. Higher distances are linked to smaller curvatures of the potential curve and thus to lower values of the Young's modulus. This relation is shown schematically in Fig. 2.2. An overview of the temperature dependence of the Young's modulus for different metals is given in Fig. 2.3

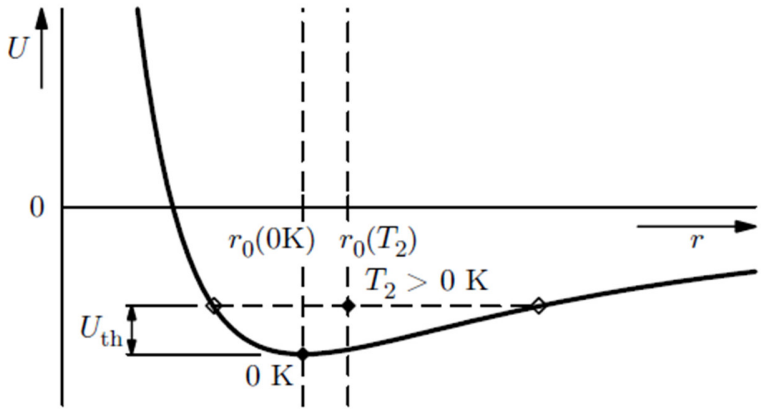

Fig. 2.2: Dependence of potential energy between two atoms on the bonding distance. Two different temperatures (0 K & T_2) and corresponding bonding distances r_0 are shown [1].

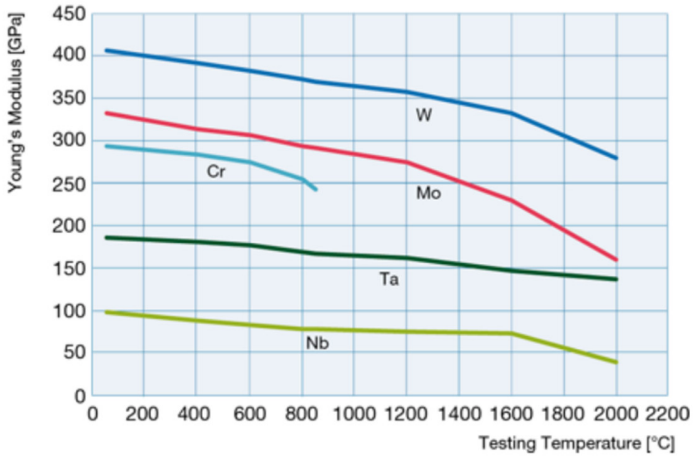

Fig. 2.3: Temperature dependence of the Young's Modulus for different body centered cubic metals [18].

2.1.3 Strain Rate Sensitivity and Activation Volume

Some materials' flow stress shows a significant dependence on strain rate they are subject to. This behavior can be described with a power-law relation such as shown in Eq.(5). Here σ_f is the flow stress, K is an auxiliary variable, $\dot{\varepsilon}$ the strain rate and m the strain rate sensitivity (SRS). By reassembling Eq.(5) with respect to m the mathematical expression for the SRS can be found such as shown in Eq.(6) [19].

$$\sigma_f = K \cdot \dot{\varepsilon}^m \tag{5}$$

$$m = \left(\frac{\partial \ln(\sigma_f)}{\partial \ln(\dot{\varepsilon})}\right)_T \tag{6}$$

The reason for the appearance of SRS can be explained by time dependent processes such as diffusive processes. Thermally activated mechanisms can be used to explain the influence of temperature and differences between bcc and fcc materials. As shown in Eq.(4) the probability of a dislocation to overcome an obstacle by thermal activation is increased by elevating temperature. Furthermore, P from this equation might be interpreted as the chance to overcome obstacles for each (temperature caused) oscillation of the atom from its lattice position. Therefore, it is obvious that due to a higher strain rate the amount of possible attempts in a certain time to overcome obstacles is decreased, which directly leads to a higher flow stress [1]. Especially the double-kink mechanism in bcc metals, which thermally enables

the movement of screw dislocations, is believed to have a major share on the plastic flow properties of bcc materials.

Opposite to fcc, bcc metals show a decreasing SRS with decreasing grain size [20]. An overview of this trend for different bcc metals in the nc, ufg and coarse grained regime is shown in Fig. 2.4a (including Tantalum) and in Fig. 2.4b (including Chromium). Whereas Fig. 2.4a shows results from tensile (T) and compression (C) tests received from ECAP and partially cold rolled specimens, those from Fig. 2.4b were obtained from electro deposited samples by nanoindentation. Though the production route as well as the testing procedure are different, the evaluated data follow the same trend of decreasing SRS with decreasing grain size in the ufg and coarse grained regime. However, it needs to be mentioned that for the lower end of accessible grain sizes – a few 10 nm – this trend is discontinued. Some investigations reveal a steep increase of SRS with decreasing grain size in this regime [21]. However, since the samples used in this work are ufg (> 100 nm) this possibly reversed trend is not for any further concern for our studies.

Though the SRS is already a major indicator for the governing mechanism of plastic flow, there is another distinctive variable which is often used in literature: The activation volume V^*. It is defined as shown in Eq.(7).

$$V^* = \sqrt{3} \cdot k_B \cdot T \cdot \frac{\partial \ln \dot{\varepsilon}}{\partial 6} \tag{7}$$

Here, k_B is the Boltzmann constant and T the absolute temperature. This number is usually divided by the cube of the Burgers vector b, which leads to the approximate amount of unit cells which contribute to the rate limiting step of plastic deformation.

For both, the strain rate sensitivity and the activation volume, one can imagine that for single crystalline and coarse grained materials which are supposed to show an indentation size effect for the hardness, this might influence these values and make them, in terms of nanoindentation, depth dependent. Maier et al. [22] could show that this is in fact only true for the activation volume, which is increasing with indentation depth till a large share of the macroscopic hardness is reached, but not for the SRS, which was found to be independent of the indentation depth.

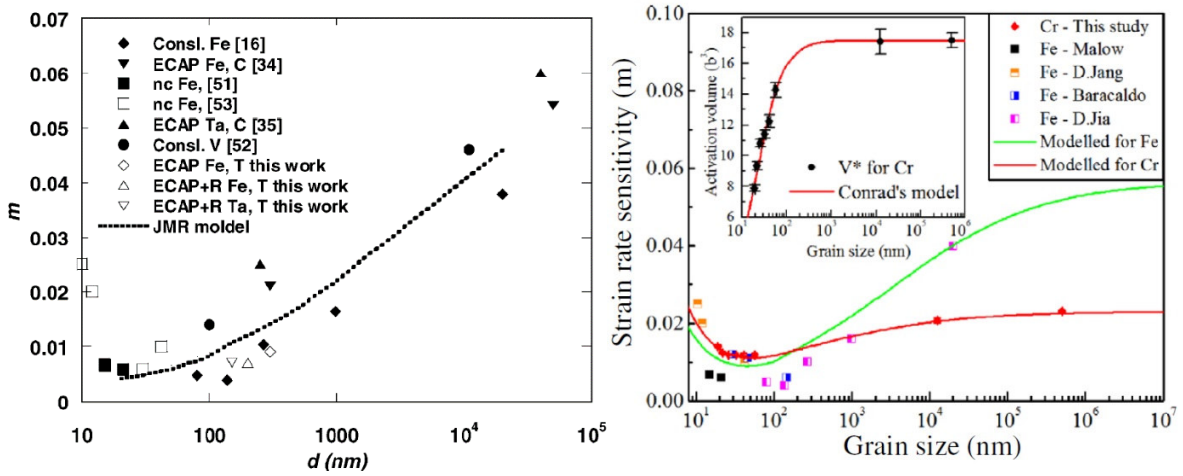

Fig. 2.4a.: Overview of the grain size dependence of the strain rate sensitivity for different bcc metals including Tantalum [23]. Production route: ECAP and partially cold rolling; testing procedure: tensile or compression tests. b.: including Chromium [21] production route: electrodeposition; testing procedure: nanoindentation.

2.1.4 Size Effect

Besides the overall differences in terms of strength for different grain sizes, there is one unique feature of coarse grained and single crystalline materials: Their yield strength and hardness are size dependent. This means that with decreasing indentation size the mentioned numbers increase. One of the first comprehensive explanations for that phenomena [24] revealed that the high strain gradients in small indents lead to a high number of geometrically necessary dislocation which harden the sample, as depicted in Fig. 2.5.

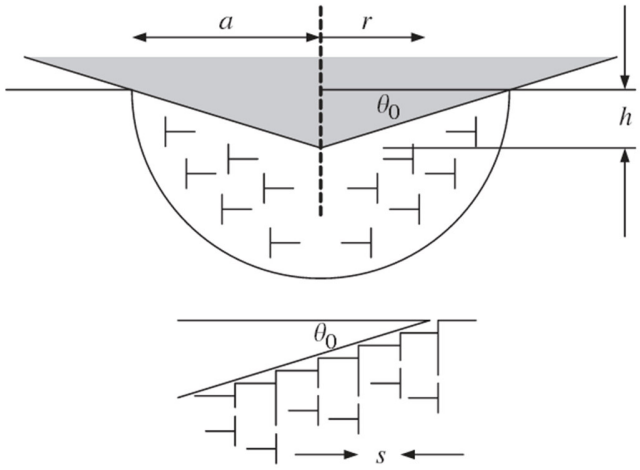

Fig. 2.5: A schematic description of geometrically necessary dislocation building circular loops with Burgers vector perpendicular to the plane of the surface to realize the ideal geometry [25].

The geometrically necessary dislocations form closed loops with Burgers vector perpendicular to the plane of the surface. Such length scale dependent behavior can not only be obtained with nanoindentation (ISE), but also with other mechanical testing procedures such as micropillar compression [26] or tensile testing [27]. Nix and Gao [24] also found a law, see Eq.(8), based on their strain gradient plasticity theory which allowed them to accurately model the size effect measured by means of nanoindentation.

$$\frac{H}{H_0} = \sqrt{1 + \frac{h^*}{h}} \tag{8}$$

Here, H is the hardness at a certain indentation depth h and H_0 is the macroscopic hardness of the material. h^* is an internal length scale which describes the increase of hardness with shallower indentation depths and is depending on the chemical composition of the material and its microstructure.

2.2 Production of Bulk Ultrafine Grained Materials

2.2.1 Technique Overview

Basically, there are two possible routes for the production of ultrafine grained or nanocrystalline materials. These are namely the top down route, which means the refinement of an already existing more or less coarse grained microstructure, most often by means of severe plastic deformation (SPD), and the bottom up route, using techniques where nano-sized powders, produced by sputtering or ball-milling, are consolidated. The later one is chosen particularly when the aimed grain size is below a certain limit accessible with the techniques of SPD. Table 2 shows a summary of commonly used methods for the production of bulk ufg materials according to [2, 21, 28].

Table 2: A summary of commonly used methods for the production of bulk nanostructured materials separated in top-down and bottom up techniques.

top-down - methods of severe plastic deformation	bottom-up - methods of consolidation
• high pressure torsion (HPT) • equal channel angular pressing (ECAP) • accumulative roll bonding (ARB)	• electrodeposition • pressing and sintering

2.2.2 High Pressure Torsion

Similar to other SPD techniques, high pressure torsion (HPT) introduces a high amount of plastic deformation in the sample in order to refine the grain structure. This is achieved by torsional movement of one out of two plungers (see Fig. 2.6) while applying a high hydrostatic pressure onto the usually disc-shaped sample. This is located in a cavity formed by the dies of the plungers. In theory it is not absolutely necessary that the sample thickness decreases during the deformation process. This is only required to assure a constant traction between the sample and the rotating plunger to avoid slipping and therefore insufficient deformation. This would, for example, work with perfectly constrained deformation conditions for the sample (Fig. 2.6a). In practical use, the deformation conditions are only partly constrained and to guarantee a steady traction between the sample and the plungers, it is feasible to use a sample with a higher thickness than the dies are able to accommodate. This leads to an emerge of excess material at the beginning of the deformation process, as it is shown in Fig. 2.6b.

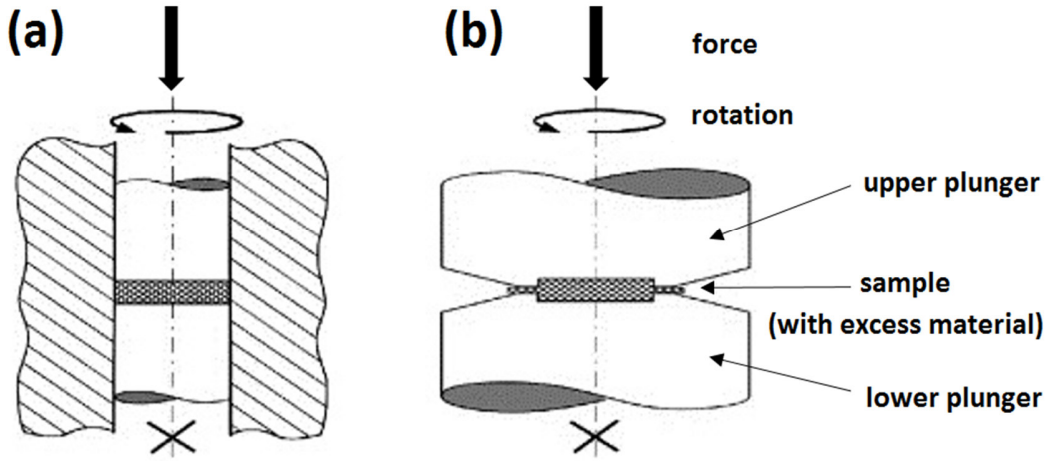

Fig. 2.6: Schematic representation of a high pressure torsion setup with mounted sample. (a) Idealized with perfect constraint conditions and (b) practical with partially constraint conditions. Adapted from [29].

Due to the rotation of the plunger, the shear strain in the sample is not equally distributed, but a function of the radius as shown in Eq.(9). Therein, *n* is the number of revolutions, *t* the thickness of the specimen and *r* the radial position along the sample.

$$\gamma(r) = \frac{2 \cdot \pi \cdot n}{t} \cdot r \tag{9}$$

It needs to be mentioned that, though this equation is often used [29, 30], an alternative formulation, also including non-shear type strain and a transformation into van Mieses strain,

can be found in the work of Zhilyaev and Langdon [31]. This relation is depicted in Eq. (10), wherein ε is the van Mieses strain. t and t_0 are the final and the initial sample thickness, respectively.

$$\varepsilon(r) = \ln\left(\frac{2 \cdot \pi \cdot n \cdot t_0}{t^2} \cdot r\right) \tag{10}$$

As a consequence, the grain size in the center of rotation should be quite unaffected and is decreasing with the radius or more specifically with strain. This is true till a certain material and processing parameter depended minimum grain size is reached at high strain levels. This typical behavior is shown in Fig. 2.7 for austenitic steel and different numbers of rotation regarding the HPT process.

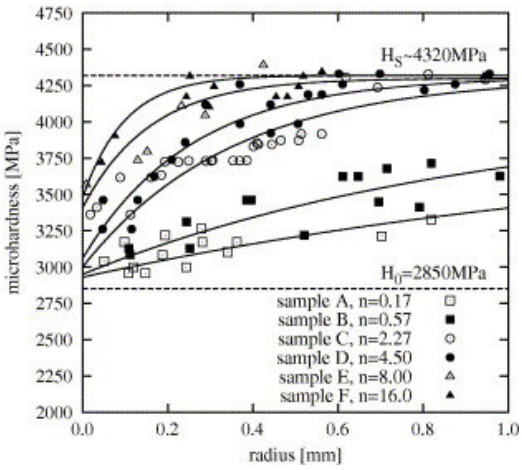

Fig. 2.7: Function of microhardness to the respect of the radius of the sample measured on austenitic steel for different numbers of rotation [29].

At a certain radial point, the hardness (which is an indicator for grain size due to grain size hardening) reaches a maximum level and is not increasing with the radius and strain anymore. Since some authors were not able to detect a significant decrease of hardness when approaching the center of their disc-shaped HPT specimens [32, 33], Pippan et al. [29] is providing possible explanations for the disappearance, which are summarized in Table 3.

Table 3 : Different reasons for the real and only seemingly disappearance of a only slightly deformed center of the HPT specimens.

actual disappearance
• Additional compressive deformation caused by the loading of the plunger • A gap between the centers of rotation for the upper and the lower plunger • Badly aligned axes of the plungers
seeming disappearance
• Hard detectability of small regions with microhardness testing • Sample preparation (badly positioned center cut for cross section measurements)*

* not **[29]**

2.3 Microhardness

These are a group of widely used techniques to observe the hardness while penetrating the sample in a depth of several micrometers. This means that features in materials which are below a certain size cannot be measured independently from other parts of the microstructure. However, it allows a precise measurement of the average hardness of the microstructure present in the sample.

A typical measurement procedure for microhardness testing is as follows: Shock-free loading of the specimen, load holding for a specific amount of time, releasing the load and optically measuring the residual plastic projected area of the indent. A complete result of such tests does not only include the calculated number (load divided by the area, see Eq.(1)) but also the measurement technique, the applied load and for not standardized dwell times these as well.

For the Vickers hardness a diamond pyramid with a square cross section and an opening angle of 136° is used as indenter. The projected diagonal lengths d_1 and d_2 of the residual indent are measured by means of light microscopy and are averaged to the variable d. The Vickers microhardness HV is finally calculated by using Eq.(11) [34].

$$HV = 0.189 \cdot \frac{P}{d^2} \tag{11}$$

2.4 Nanoindentation

In the last decades the popularity of nanoindentation techniques increased dramatically for different reasons. Besides the unique possibility of testing very thin films, it is primarily the ability to determine a wide variety of mechanical properties such as Young's Modulus, hardness, creep and relaxation behavior, and many more, in the deep sub-micron regime [35]. As for the microhardness testing, several different indenter shapes, such as Berkovich, spherical, Cube Corner, and conical are used. However, since the experiments of this work where all carried out with Berkovich indenters, the following explanations will be focused on this type.

Nanoindentation is referred to as depth-sensing indentation (DSI). This means that during the process of indentation the penetration depth and the corresponding load are continuously recorded, which leads to load displacement curves such as shown in Fig. 2.8. These are the very basis of every DSI type analysis. Instead of any optical or electron-microscopic measurements of the projected indentation area after the indentation, as it is typical for microhardness testing, is derived from the recorded depth and the known indenter geometry. Since many materials, but especially ceramics and metals, show a significant elastic recovery when unloading, there is a need to specify the different depths which can be measured and particularly the depth which is used to calculate the projected indentation area. Fig. 2.9 shows the shape of the loaded indent and the residual plastic deformation after unloading. The maximum reached depth h_{max} is consisting of an elastic depth h_{el} and a plastic depth h_{pl}. When the indenter penetrates the sample, the surface is bending away in such a way that the actual contact depth h_c is smaller than the maximum depth in the load displacement curve. h_c is derived from the maximum depth and the derivation of the unloading curve, see chapter 2.4.1.

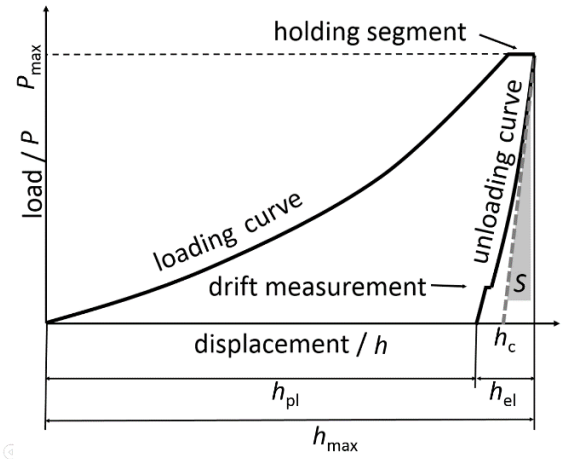

Fig. 2.8: Typical load displacement curve including the loading, holding and unloading part as well as the most important displacements.

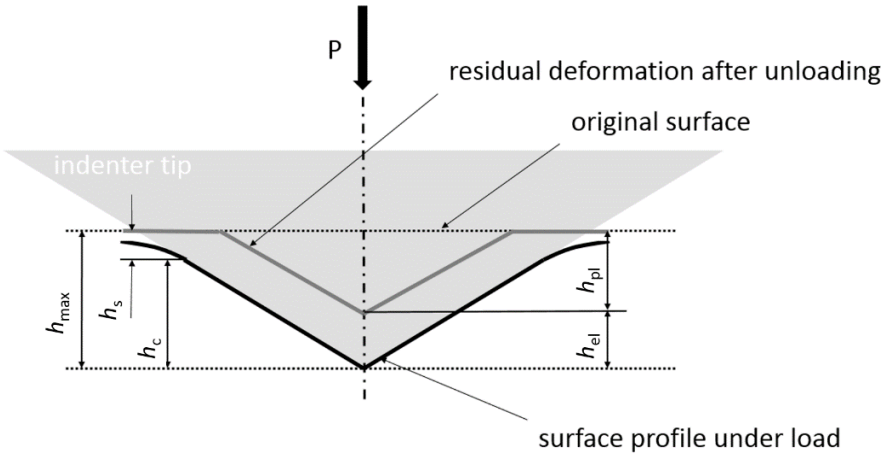

Fig. 2.9: Schematic illustration of the different displacements for a surface under load (black line) and after the unloading (grey line).

2.4.1 Load Schemes

As discussed in chapter 2.1.3, the materials hardness and strength are to a certain degree influenced by the strain rate at which the sample is loaded. Therefore it is obvious that in order to enable the comparison of results, the strain rate needs to be kept constant. Basically there are two different options. The first one is two use static experiments where during the loading $\dot{P}/P$ is held constant as proposed by [36] and shown in Eq.(12). Here P and $\dot{P}$ are the loading and the rate of loading respectively. The other option is to hold just the loading rate constant at a certain level which leads to a quasi-static strain rate. For the latter one, the strain rate can be again calculated with Eq.(12).

$$\dot{\varepsilon} = \frac{\dot{P}}{P} \tag{12}$$

Since the unloading part of nanoindentation experiments is fully elastic, it is possible to unload at a certain force, gaining an unloading curve for the determination of the stiffness, and load again. This cyclic procedure leads to several hardness and Young's modulus versus depth couples per indent. The different peak loadings can be calculated by Eq.(13), were P_n is the peak load at a certain cycle number n, P_{max} is the maximum peak load, N the maximum cycle number and q a spreading factor [22].

$$P_n = P_{\max} \cdot \frac{q^{n-1}}{q^N} \tag{13}$$

By combining Eq.(12) and (13) the quasi static strain rate can be determined only depending on loading time t_{load}, spreading factor and the share of unloading a. This means that for all cycles, though they have different peak loads, the strain rate is equivalent.

$$\dot{\varepsilon} = \frac{q + a + 1}{q \cdot t_{\text{load}}} \tag{14}$$

2.4.2 Determination of Hardness and Young's Modulus

Nanoindentation experiments provide primarily the load-displacement curves as output data. In the past there were different approaches to use these to determine the mechanical properties of the samples material. In 1992 Oliver and Pharr [37] suggested a procedure which instead of assuming a linear unloading curve, uses a power function to fit it.

$$P(h) = A \cdot (h - h_{\text{f}})^q \tag{15}$$

A, h_f and q are fitting parameters. The stiffness S_{total} of the sample frame combination is obtained by differentiating Eq.(15) with respect to h and setting h equals h_{max}, as shown in Eq. (16).

$$S_{total} = \frac{dP}{dh} = A \cdot q \cdot (h_{\max} - h_{\text{f}})^{q-1} \tag{16}$$

In order to separate the stiffness of the machine and the sample itself, the frame compliance C_f is subtracted from the total compliance C_{total}, which is the inverse of the overall stiffness S_{total}. This approach (Eq.(17)) provides the stiffness S of the sample.

$$S = \frac{1}{C_{\mathrm{total}} - C_{\mathrm{f}}} \tag{17}$$

The elastic deformation around the indenter tip h_s is a function of P_{max}, S and a variable called ε ($\varepsilon_{Berkovich}$ = 0.75) taking the tip geometry into account (Eq. (18))

$$h_{\mathrm{s}} = \varepsilon \cdot \frac{P_{\mathrm{max}}}{S} \tag{18}$$

The contact depth is calculated by subtracting h_s from h_{max}. Combining this with Eq. (18) leads finally to Eq.(19), which is commonly used to determine the contact depth from nanoindentation experiments.

$$h_{\mathrm{c}} = h_{\mathrm{max}} - \varepsilon \cdot \frac{P_{\mathrm{max}}}{S} \tag{19}$$

To evaluate the contact area A_c from the contact depth, it is crucial to know the exact relationship between these two numbers, the so called area function. For this task Oliver and Pharr [37] proposed an approximation by means of a polynomial equation (Eq.(20)) in which C_1 to C_9 are the coefficients. For the sake of simplicity in practice usually only the first three terms are used. The error caused by skipping the last six terms is considered to be less than the inaccuracy of the area function calibration (see chapter 2.4.3).

$$A_{\mathrm{c}}(h_{\mathrm{c}}) = \mathrm{C}_1 \cdot h_{\mathrm{c}}^2 + \mathrm{C}_2 \cdot h_{\mathrm{c}} + \mathrm{C}_3 \cdot h_{\mathrm{c}}^{\frac{1}{2}} + \mathrm{C}_4 \cdot h_{\mathrm{c}}^{\frac{1}{4}} + \cdots + \mathrm{C}_9 \cdot h_{\mathrm{c}}^{\frac{1}{128}} \tag{20}$$

Finally, the hardness can be calculated as the quotient of the maximum load and the calculated contact area, which leads to Eq. (21).

$$H = \frac{P_{\mathrm{max}}}{A_{\mathrm{c}}} \tag{21}$$

The reduced modulus E_r, which is a property of the sample and the indenter, can be obtained by Eq.(21). β is a geometry factor which takes into account that the Berkovich indenter tip is not a body of revolution ($\beta_{Berkovich}$ = 1.034).

$$E_r = \frac{\sqrt{\pi}}{2 \cdot \beta} \cdot \frac{S}{\sqrt{A_c}} \tag{22}$$

Since the contact between sample and indenter tip is very similar to a series of springs with a certain stiffness, the relation between reduced modulus E_r, the modulus of the indenter E_i and the sample modulus E, is very close to such equations as well. Only the lateral contraction needs to be further taken into account by the Poisson's ratio of the indenter material ν_i and of the sample material ν.

$$\frac{1}{E_r} = \frac{1 - \nu_i^2}{E_i} + \frac{1 - \nu^2}{E} \tag{23}$$

2.4.3 Calibrations

As a consequence of the dependency of both, hardness and Young's modulus on the frame compliance and the area function, the need for a precise calibrations of both values arises. In order to do so a material with isotropic mechanical properties is used for the calibration indents. Commonly used is fused silica with a hardness of 8.8 GPa, a Young's modulus of 69.6 GPa and a Poisson's ratio of 0.17 [38]. Moreover, fused silica shows only very little tendency to form "pile-ups" (see chapter 2.4.8), which might falsify results when not concerned. Although recent publications [39] report that the area function measured on fused silica is not an inherent property of the tip alone but rather of the fused silica as well, it still remains a very suitable reference material.

For the actual calibration about 100 indents with different loads and therefore different depths are made. Since the mechanical properties hardness and Young's modulus are well known for fused silica, one can calculate the area function for different loads using Eq. (21) and Eq. (22). By the use of a least square method the frame compliance is varied till a minimum mismatch between the results from the two mentioned equations is reached.

Likewise is the procedure for the area function determination: A least square method is again used to obtain a minimal mismatch between A_c derived from Eq. (21) and Eq. (22), this time varying the coefficients of the first three terms of Eq. (20).

2.4.4 Analysis of the Indentation Size Effect

As mentioned in chapter 2.1.4, the ISE is only pronounced in coarse grained or sx materials. In Fig. 2.10a three hardness versus depth curves showing a clear ISE are plotted for the single crystalline bcc metals tungsten, molybdenum and niobium.

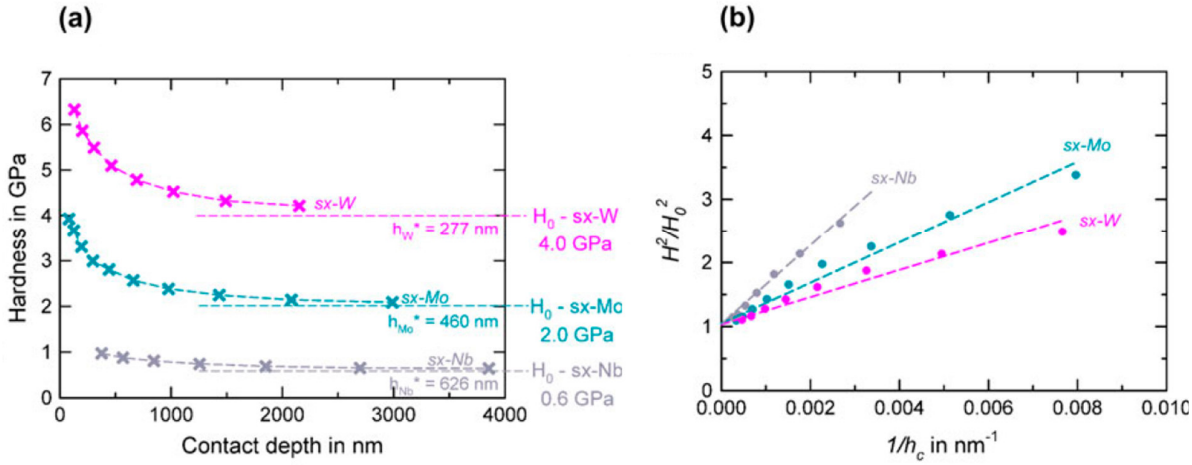

Fig. 2.10 (a) shows an overview of the size effect measured on different bcc single crystals, namely Tungsten, Molybdenum and Niobium. (b) The relating Nix-Gao plots [17].

For the actual evaluation of the ISE the model of Nix and Gao is used (Eq.(8)). Since the hardness values H at certain depths h are known, the macroscopic hardness H_0 as well as the internal length scale h^* can be computed. For that task the original equation is rewritten to Eq.(24), which is obviously linear and thus offers the possibility of using linear regression methods.

$$H^2 = H_0^2 + H_0^2 \cdot h^* \cdot \frac{1}{h} \tag{24}$$

With the y-interception of the regression line H_0 can be determined which is further required to calculate h^*. The gained data are usually shown in a so called Nix-Gao plot where the ordinate is $H^2/H_0^2$and the abscissa is the reciprocal value of h. This is to enable a direct display of h^* via the slope of the regression line (Fig. 2.10b)

Of special concern for the interpretation of the gained data is the fact that the ISE is not every time easily distinguishable from other effects. Fischer-Cripps [35] reports of several non-ISE related influences observed which can really, or only seemingly increase the hardness of a material at shallow depths and might be misinterpreted as ISE (Table 4).

Table 4 : Summarization of different reasons to obtain an actual or only and seeming increase of hardness values at shallow indentation depths.

actual hardness increase	seeming hardness increase
• Indentation size effect	• Bad area function
• Oxide layer on the surface	• Friction between indenter and surface
• Strain hardening from preparation	

2.4.5 Determination of Strain Rate Sensitivity and Activation Volume

There are several different methods to obtain SRS with nanoindentation. These are mainly nanoindentation strain rate jump tests (SRJ) [23], which apply different distinctive strain rates during one indentation cycle. The constant strain rate method (CSR) proposed by Lucas [36] is based on several indents with different but constant strain rate. Finally, the constant load (CL) method suggested by Mayo et al. [40] uses relaxation during a constant load segment to obtain the required hardness and strain rate data. Since for the strain rate jump test special equipment is required and for the CSR method already problems have been reported from the past with the used setup, especially arising from issues with very low strain rates, the experiments carried out in this work are all CL method based. Thus, this chapter is focused on this approach to determine SRS.

The basic idea of the CL method is that one is, due to the creep of the material, able to obtain time dependent hardness and strain rate numbers. This results in a major difference compared to the other techniques mentioned above. Whereas the CL method offers continuous hardness and strain rate data, those for CSR and SRJ are point by point. The hardness for nanoindentation experiments was already determined in Eq. (21). A_c is a function of h_c (Eq.(20)), which is increasing over time as a result of the creeping material when using the CL method. Hence, the hardness becomes a time dependent number as well. The strain rate $\dot{\varepsilon}$ on the other hand is defined as shown in Eq. (25). Here, h_a is the absolute depth consisting of a time dependent part h_r and the depth h_0 reached during the loading of the indenter right before the holding segment starts (Eq.(26)). Consequently, $\dot{h}_a$ is it the derivative of h_a with respect to time, which is required to calculate the strain rate.

$$\dot{\varepsilon} = \frac{\dot{h_\mathrm{a}}}{h_\mathrm{a}} \tag{25}$$

$$h_\mathrm{a}(t) = h_\mathrm{r}(t) + h_0 \tag{26}$$

Different to usual nanoindentation tests, which are targeted on evaluating hardness and Young's Modulus, experiments with long dwell times often lead to a considerable depth gain by creeping. h_s calculated with Eq.(18) using the slope of the unloading curve gives the accurate contact area for the end of the holding segment, whereas h_s for the start of it is somewhat smaller. However, this is a systematic drawback of this method which can only be avoided by using constant stiffness measurement (CSM) techniques [41]. For the present experiment, the whole range of h(t) has been subtracted by the same h_s calculated from the unloading slope to obtain a quasi-contact depth h_a(t).

It is common practice to fit the received depth versus time data [42, 43]. This simplifies the differentiation with respect to time which is required for the calculation of $\dot{h_\mathrm{a}}$. The fitting was eventually done according to Eq. (27).

$$h_\mathrm{r}(t) = a \cdot (t - b)^c + d \cdot t \tag{27}$$

In Fig. 2.11 an illustration of the original raw data of a nanoindentation experiment as well as the related fitting curve are shown. It is evident that the creep rate is decreasing over the dwell time, which provides the required range of different strain rates for later evaluation. This enables, finally, the SRS to be determined for every couple of hardness and strain rate assessable with utilizing Eq.(6).

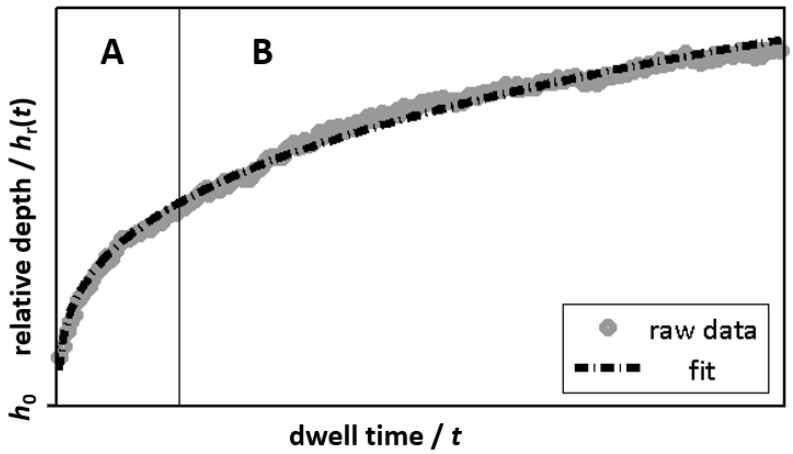

Fig. 2.11: Illustration of the time dependent part of the creep curve $h_r(t)$ and the related fit. Furthermore, the plot is schematically separated into Stage A and B.

Owing to the mentioned continuous data of hardness and strain rate, there is also not one SRS but rather as many as hardness and strain rate data couples. This leads to the question of comparability of the measured SRS to different techniques. Recently, there are two major approaches. Peykov et al. [42] suggested to separate the creep curve into two distinctive regions, namely stage A and B (see Fig. 2.11) and calculate an average SRS for both. This idea is primarily driven by the assumption that stage B might be stronger influenced by drift issues than stage A, and that the received m-values from stage A where fairly consistent with those obtained by discontinuous methods. Opposite to that, Maier et al. [41] proposed to interpret the different values as dependency of the SRS to the flow stress, consistent to Eq.(6). Both approaches will be involved in the calculation and the following discussion, see chapter 4.4.3.

In order to calculate the activation volume a slight alteration of Eq. (7) is used. Since the SRS and the hardness are already known, Eq. (28) is a practical approach in determining V^*. Since the flow stress needs to be derived from the hardness, it is necessary to estimate the constraint factor, which was finally determined as 2.8 for all samples [10].

$$V^* = \sqrt{3} \cdot k_B \cdot T \cdot c^* \cdot \frac{1}{m \cdot H} \tag{28}$$

2.4.6 Activation Energy

Another number being characteristic for the dominating plastic deformation process is the activation energy Q_a. It can be determined by the use of hardness numbers H and Young's moduli E at different temperatures as described in Eq. (29) [44]:

$$\frac{H}{E} = G \cdot \exp\left(\frac{Q_a}{n \cdot R \cdot T}\right) \tag{29}$$

Further on, G is the pre-exponential coefficient, n is the stress exponent, R is the universal gas constant and T is the absolute temperature. The activation energy itself can be observed by plotting the data in an Arrhenius type diagram, were Q_a can be determined by calculating the slope. Eventually a literature comparison with the calculated activation energies enables an estimation of the dominant deformation mechanism [45].

2.4.7 Incipient Plasticity – "Pop-Ins"

The load displacement curves of nanoindentation tests carried out on well-polished and non-deformed materials (e.g. fully annealed or single crystalline materials) show a remarkable feature. The transition between purely elastic to plastic deformation is accompanied by a depth excursion of the indenter while the load keeps constant in a load-controlled test. The so called "pop-in" marks the onset of plasticity, or, put differently, the moment where dislocations start to move. A typical load displacement curve for such a behavior is shown in Fig. 2.12.

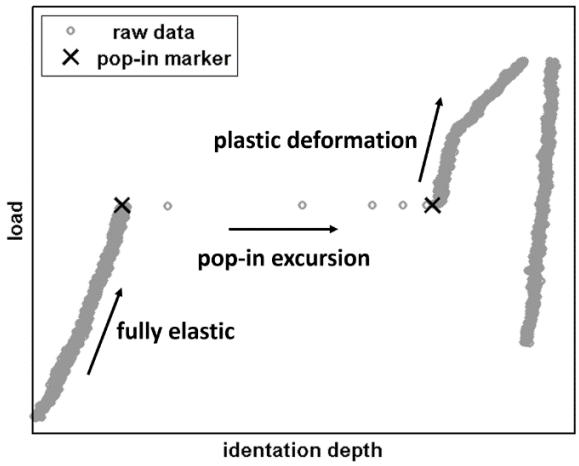

Fig. 2.12: Schematic illustration of a typical load displacement curve of a load controlled test, including a pop-in event. The ranges of the elastic as well as of the plastic part (separated by the pop-in excursion) are shown.

It has been reported numerous times that regarding to contact mechanical considerations the shear stress sustained before yielding is in the order of the theoretical shear strength [46]. Furthermore the very small probed volumes of nanoindentation experiments are often assumed to be free of dislocations and other sorts of defects. Taking these thoughts into consideration, it seems feasible to attribute homogeneous dislocation nucleation (in particular

the formation of a closed loop) to the pop-in event, as it was suggest among others by Chiu and Ngan [47]. First doubts to this theory where mentioned by Mason et al. [48] who found higher rate and temperature dependencies (lower activation energies and volumes) than expected for homogeneous dislocation nucleation. In 2008, Shim et al. [49] reported a significantly decreased shear strength, when the indenter tip radius was increased. They suggest that the higher the tip radius and hence the stressed volume beneath it, the higher is the probability to activate preexisting dislocations, rather than nucleating new. This situation is illustrated in Fig. 2.13.

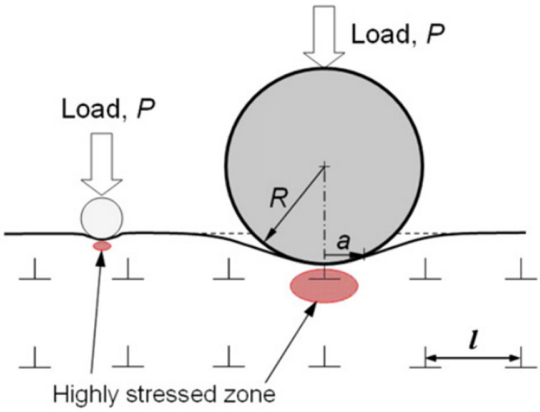

Fig. 2.13: Interaction of stress fields with preexisting dislocations caused by tips with different radii [49].

Furthermore, a current report [50] obtains proper accordance of the theory of homogenous dislocation nucleation for small tip radii (< 210 nm), but not for larger ones. Consequently, it is supposed that for very small volumes the homogenous dislocation nucleation governs the incipient plasticity, whereas for larger ones the activation of already existing dislocation might be predominant. This is underlined by Fig. 2.14, in which the cumulative probability of pop-in events versus the load is displayed for radii ranging from 60 nm to 759 nm [50]. While (a) shows a comparison with a prediction (solid line) only based on homogenous dislocation nucleation, (b) shows a new prediction involving activation of already existing dislocations as well, which gives a much better fit, in particular for large tip radii.

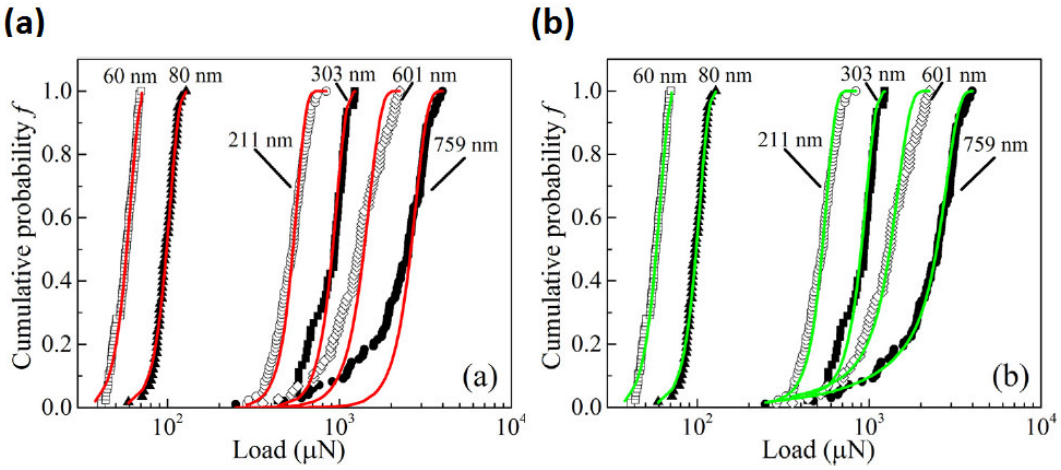

Fig. 2.14: Comparison of measured and predicted cumulative probability of pop-in events for (a) a model based only on homogenous nucleation of dislocations and (b) for a model including the activation of preexisting dislocations as well [50].

For the analysis of the incipient plasticity data gained from nanoindentation, usually the assumption is made that the contact between indenter tip and the surface of the sample can be approximated with Hertz' contact relation between a sphere and a flat surface. This is not only assumed for actual spherical, but also for Berkovich indenters with a rounded tip [51]. The equation for the depth dependence of the load is shown in Eq.(30).

$$P = \frac{4}{3} \cdot E_{\mathrm{r}} \cdot R^{1/2} \cdot h^{3/2} \tag{30}$$

P is the load, E_{r} the reduced modulus of the contact, R the tip radius and h the elastic depth. By fitting the elastic part of the loading curve, either the tip radius can be estimated from a known reduced modulus (which was done in this work) or vice versa. To trigger the depth recording of the used nanoindenter, a load of 0.05 mN is required. For logical reasons the load data start at this number as well. Nevertheless, the exact depth at this load, which is assumed to be higher than zero, cannot be known precisely. In the light of that, Hertz' contact equation was modified by an additional fitting parameter h_0 which represents the starting depth, as well as with an additional constant P_0 = 0.05 mN representing the trigger load. This leads to Eq.(31), which was used to fit the elastic loading part of the sx materials, where a is a proportional constant considering the tip radius and the reduced modulus of the sample tip contact.

$$P = P_0 + a \cdot (h + h_0)^{3/2} \tag{31}$$

The maximum shear stress τ_{max} under the indenter at pop-in load can be calculated with Eq.(32).

$$\tau_{\max} = 0.31 \cdot \left(\frac{6 \cdot P \cdot E_{\mathrm{r}}^2}{\pi^3 \cdot R^2} \right)^{1/3} \tag{32}$$

This number can be compared to the theoretical shear strength of the material which can be calculated according to Eq. (33). The shear moduli reported in literature are 115 and 69 GPa for chromium and tantalum, respectively [52].

$$\tau_{\mathrm{th}} = \frac{G}{2 \cdot \pi} \tag{33}$$

2.4.8 Pile-ups and Sink-ins

Plastic deformation under the indenter might lead to plastic distortions, either called sink-ins or pile-ups, of the material around it. Both of them are not considered by the Oliver-Pharr procedure [22]. Which one of those actually occurs is expected to be dependent on the ratio of yield strength to Young's modulus and the strain hardening properties of the material. According to [35], materials with a high strain hardening potential (e.g. well annealed or sx metals) might be more likely subject to sink-ins. This is caused by a strength gain of plastically deformed material which leads to a favored flow of the residual material around it. Thus material farther away from the indenter has a bigger share on the overall plastic deformation and the material close to indenter tends to sink in. On the other side materials with low strain hardening potential (e.g. highly deformed metals such as ufg materials produced by SPD) and a high ratio of young's modulus to yield strength are showing a higher susceptibility for pile-ups. This is for the simple reason that most of the plastic deformation takes place close to the indenter. In Fig. 2.15a, a schematic cross-section of an indent shows sink-in behavior on the left side and piling up on the right side. Fig. 2.15b illustrates the actual contact areas of indents which are influenced by a sink-in (left) and a pile-up (right), respectively.

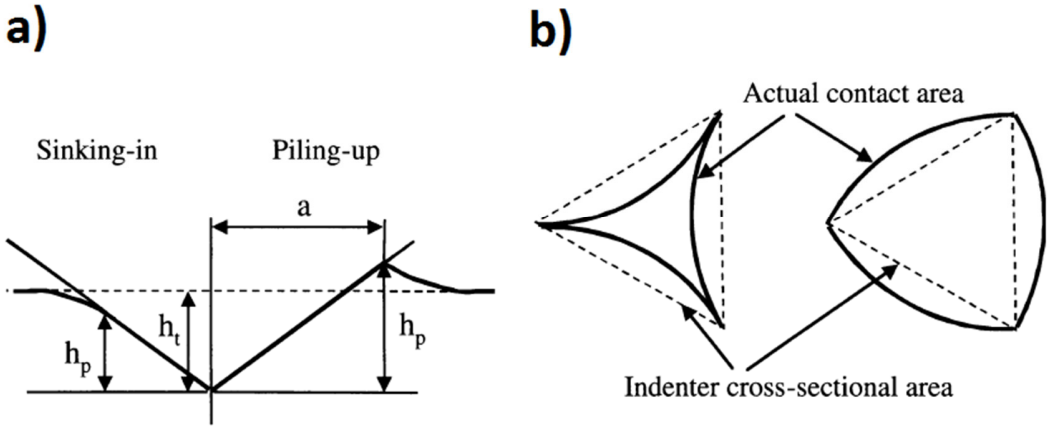

Fig. 2.15: A schematic cross-section of an indent with a sinking-in on the left side and a piling-up on the right side (a). Actual contact are of indents which are subject to sink-in (left) and pile-up behavior (right) (b). Adapted from [35].

As a result of such distortion, the contact area is either underestimated (sink-in) or overestimated (pile-up). Since A_c is influencing all further analysis results, unnoticed sink-ins or pile-ups might falsify the final experimental results considerably. For indents with a sufficient size, strong distortions are potentially detectable with light microscopy. Otherwise the use of a scanning electron microscope (SEM) is feasible, though only the use of an atomic force microscope (AFM) or similar devices delivers sophisticated information about the distortion's exact geometry. In the past, several different procedures had been suggested to take these issues into consideration [53, 54]. However, a very simple procedure to correct the influence of pile-ups and sink-ins is to estimate their heights or depths, by means of atomic force microscopy or similar techniques. The ratio of h_p to h_t (Fig. 2.15a) can then be used to adjust the contact depth.

3 Experimental Procedure

3.1 Starting Material

The starting material for this work were single crystalline chromium and tantalum rods with a diameter of 10 mm, obtained from Mateck GmbH, Jülich, Germany. Their purities are 5N and 4N for chromium and tantalum, respectively. These were cut by means of a diamond wire saw into about 1 mm thick disc-shaped samples. Since sx and ufg samples were required, one sample of each material was kept in the sx state, whereas three others were processed by HPT to achieve an ufg microstructure without any changes in purity. After the surface preparation, each disc was finally cut into four segments to achieve a higher amount of individual samples for later high temperature experiments.

3.2 High Pressure Torsion

For the production of the ufg samples from the sx discs, the HPT facility at the Erich- Schmid-Institut, Leoben, Austria with a maximum load equivalent to 40 t was used. To enable the processing of different materials (e.g. single crystals, powders, etc.) and different sample sizes, the upper and the lower plunger are exchangeable. Before mounting the sample in the lower plunger, the dies and the sample were sandblasted. This was done to increase friction in order to avoid slipping between the rotating upper plunger and the samples.

The HPT runs itself were carried out with the maximum available load of 40 t (≈390 kN), which resulted in an approximate hydrostatic pressure of 4.95 GPa. In total, 10 revolutions were conducted at a rotational speed of 0.2 min^{-1} on each sample. Due to the high strengths of the final ufg material, the abrasion of the plunger dies was considerably high. Therefore, after every second run, the dies of both plungers were reshaped by lathing and subsequently sandblasted. Altogether, three chromium and three tantalum discs were processed, which all had a thickness between 0.6 and 0.7mm.

3.3 Sample Preparation

The preparation of the surface plays a major role for the accessibility of very fine microstructures to methods of electron microscopy such as BSE and EBSD imaging. Moreover the thorough preparation is crucial for the reliability and homogeneity of nanoindentation experiments. The sx as well as the ufg samples were prepared according to Table 5. In detail, for the microstructural investigations the disc cross-sections for radius-dependent examination were prepared, for the nanoindentations the top surfaces, respectively (Fig. 3.1).

Table 5 : Overview of the preparation methods for sx and ufg chromium and tantalum. Numbers written in brackets represent the graining of the used polishing method.

methods	chromium	tantalum
• mechanical grinding	- SiC 500-4000	- SiC 800-4000
• mechanical polishing	- MD-Dur (9 µm) - MD-Dac (3 µm) - MD-Nap (1 µm) - MD-Chem (0.04 µm)	- MD-Largo (9 µm) - MD-Dac (1 µm) - MD-Chem (0.04 µm)
• electrolytic polishing	- electrolyte: A2 (Struers) - voltage: 20 V - time: 10 s	-
• VibroMet	-	MD-Nup (0.04 µm)

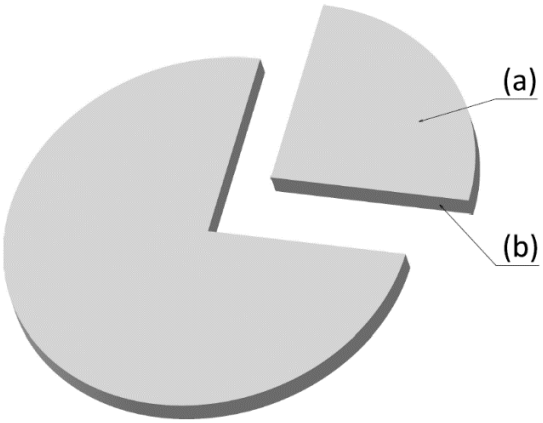

Fig. 3.1: Schematic illustration of the origin of the final sample shape from the HPT processed disc. On the light grey area (a) nanoindentation experiments were conducted, the dark grey cross section area (b) was used for microhardness tests as a function of sample radius.

3.4 Microhardness Measurements

Microhardness measurements were conducted on halved HPT-samples (ufg) (Fig. 3.1b) over the whole radial range of their cross-sections for both materials. This was done to obtain the radius dependency of the hardness and hence the onset of the HPT grain size refinement limit. The middle of the cross-sections was used as a starting point, measurements with a spacing of 0.5 mm along the radius of the specimen were subsequently performed, resulting in about 21 indents per sample.

The measurements were conducted on a BUEHLER MicroMet 5100. The used loads were 500 g (HV 0.5) for chromium and 1000 g (HV 1) for tantalum, respectively.

3.5 Microstructural Investigations

In order to gain detailed information about the evolved microstructure of the HPT samples, EBSD and BSE imaging was used. This is of major interested because the grain structure exceptionally contributes to the mechanical properties of the material as discussed in chapter 2.1.1. The used SEM was a LEO Gemini 1525 (Zeiss, Oberkochen, Germany) equipped with BSE and EBSD detectors.

As for all techniques based on backscattered electrons, EBSD and BSE signals increase with the atomic number (Z) of the material [55]. Since for the EBSD pattern only the part of electrons satisfying Bragg's law are contributing, this method is particularly delicate to a lack of backscattered electrons. Due to the higher atomic number of tantalum (Z_{Ta} = 73) compared to chromium (Z_{Cr} = 24), it was expected to obtain higher quality EBSD maps from tantalum. For this reason, the microstructural investigation of chromium was eventually carried out by means of BSE imaging. Since this technique does not allow for an automatized determination of the average grain size, a manual grid method was used. Thereby, a grid is superimposed to a BSE image and the number of grain boundaries on a grid line are counted, enabling the calculation of the average grain size. For the EBSD analysis a minimum grain size of ten pixels and a minimum misorientation of 15° where set. For both materials different radial distances from the center of the cross-section were chosen to investigate the dependency of the microstructure and especially the average grain size with respect to the radial position of the sample. In Table 6 the exact positions of the microstructure measurements are shown.

Table 6 : Radial positions of the microstructural investigations of chromium and tantalum.

chromium ufg (BSE) [mm]	tantalum ufg (EBSD) [mm]
0.0 – 1.0 – 2.0 – 3.0 – 4.0	0.0 – 0.5 – 1.0 – 1.5 – 2.0 – 2.5 – 3.0 – 3.5 – 4.0 – 4.5

3.6 Annealing Experiments

Since the nanoindentation tests were performed at several different elevated temperatures, the chance of a recrystallization of the ufg microstructures had to be investigated prior. The widely known Tammann's law [56] suggests that for highly deformed pure metals, the recrystallization temperature is at about 40 % of the melting temperature. Although this is only a very rough estimation (not including the exact degree of deformation, impurities, alloy elements, etc.), it shows the importance of the melting point for recrystallization. Both materials used in this work are refractory metals which are well known for their high melting points. However, chromium ($T_{m,Cr}$ = 1907 °C) is quite a bit lower than tantalum ($T_{m,Ta}$ = 3020 °C) [52]. Therefore, only chromium was subject to the performed vacuum annealing tests regarding microstructure stability.

The annealing runs were carried out from 100 to 500 °C with 100 °C steps in between in a XERION vacuum furnace. The temperature profile was set accordingly to a heating rate of 10 °C/min and a dwell time of 60 min. After each annealing the microstructure of the chromium sample was investigated by electron microscopy (BSE) at a radial positons of 4 mm with respect to the center of the sample.

3.7 Nanoindentation

In order to obtain mechanical properties such as hardness, Young's modulus, SRS and activation volume, nanoindentation experiments were conducted. In the following chapter the instrumental setup, as well as the different tests and corresponding parameters are explained. The data processing and plotting was carried out with the manufacturer's software NanoTest Platform Three ®, Microsoft Excel®, and largely using self-written MATLAB® scripts.

3.7.1 Experimental Setup

The used nanoindentation facility Micro Materials NanoTest Platform3, Micromaterials, UK (Fig. 3.2a) was located at the Department of Nuclear Engineering, University of California, Berkeley. The setup consisted of the nanoindenter, the vibration damping table it was placed on, and the chamber it was housed in. The latter is required to enable the implementation of the purging gas system. This is intended to keep an extremely low oxygen content atmosphere in the chamber to avoid oxidation and similar undesired influences. For high temperature experiments the nanoindenter was equipped with a high temperature option with heated indenter tip and sample configuration (Fig. 3.2b). This allows a separate controlling of indenter and sample temperature. Because of their high reactivity with transition metals such as chromium and tantalum, respectively, diamond indenters are fairly sensitive to high temperature contact with this type of metals [57]. However, since the maximum temperature for the experiments carried out in this work was only around 300 °C, a diamond indenter ($E_{diamond}$ = 72 GPa, $\nu_{diamond}$ = 0.07) was used for room temperature, as well as for elevated temperature indentation experiments.

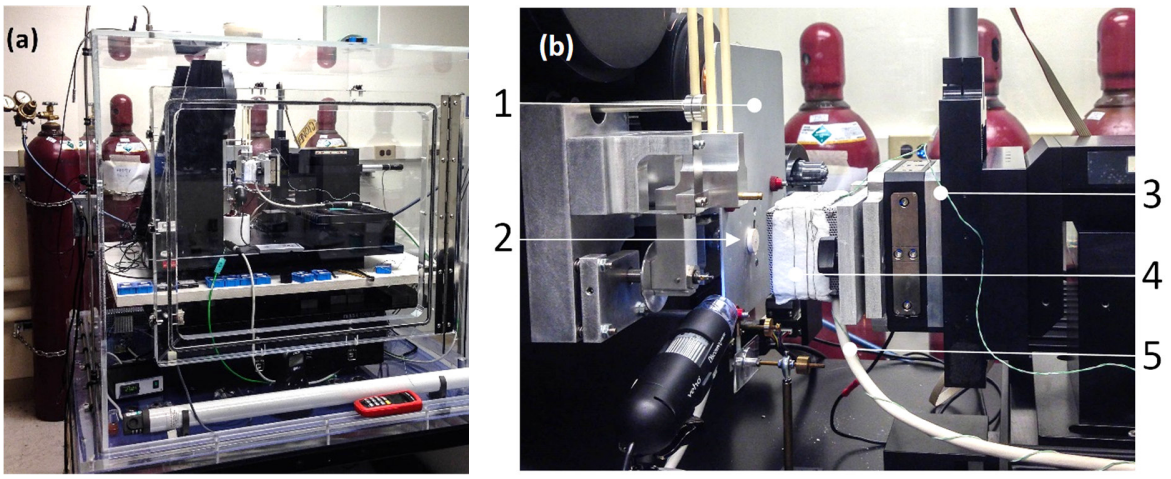

Fig. 3.2: Overview of the nanoindenter in the chamber (a). Details of the actual high temperature indentation set-up (b) showing heat shield (1), indenter (2), stage (3), high temperature sample holder and heating system (4) and wiring for the sample heater's power supply and the thermocouple (5).

3.7.2 Preparation for Nanoindentation

For the room temperature experiments, the samples where fixed to a shaft-shaped aluminum sample holder with super glue. For elevated temperatures a heatable sample holder was used instead (Fig. 3.3). Furthermore high temperature cement (Omega Bond 600) was applied instead of the glue to avoid degradation issues. On the surface of the heated area of the sample

holder, the actual specimen and a dummy sample with an attached thermocouple were mounted. While the specimen surface was kept free, the thermocouple was fixed to the surface of the dummy sample with cement. In order to guarantee consistent drying of the wet deployed cement, a waiting time of approximately one day was used. After attaching the sample holder onto the nanoindenter stage, another hour was waited with the chamber door closed for thermal equilibration.

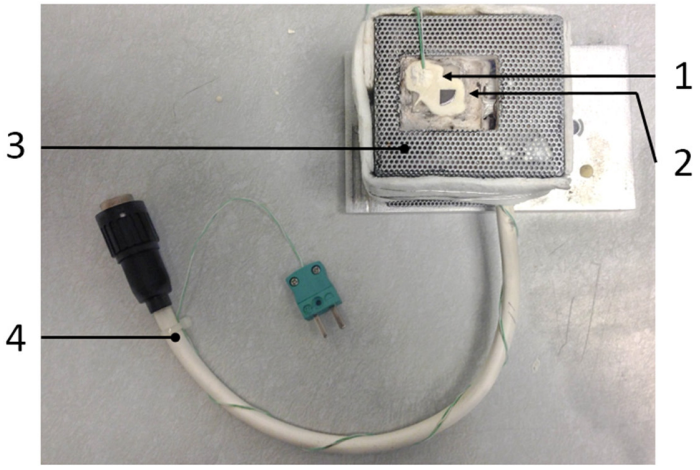

Fig. 3.3: Dummy sample for temperature control (1) and indentation sample (2) on the heatable sample holder ("hot stage") (3) with the according wires for power supply and the thermocouple (4).

3.7.3 Experimental Parameters

Though microhardness measurements and microstructural investigations show a fairly wide radial range with similar sample properties for the ufg specimens, a radius of 3.5mm to the former disks center was chosen as testing area. For the single crystalline samples no such limitations were applied. The required maximum loads for each material were determined by test indents. The loading time was chosen to provide a comparable strain rate, whereas the unloading time was set empirically. Though it needs to be mentioned that this leads to different loading and unloading strains. The used set-up provides an automatic drift correction measurement at the end of the (last) unloading curve. This can be seen in Fig. 3.4 and Fig. 3.5.

Basically two different types of experiments were conducted. The first one was to obtain hardness and Young's modulus with short dwell times to avoid distortion caused by creep or thermal drift. These were carried out with a cyclic loading scheme consisting of eight consecutively increasing peak loads and thus eight unloading curves such as shown in Fig. 3.4. A further use of these tests was to observe pop-in events on the sx samples. An overview of

the parameters for these experiments can be seen in Table (7). The different peak loads for this kind of tests were calculated with Eq. (13).

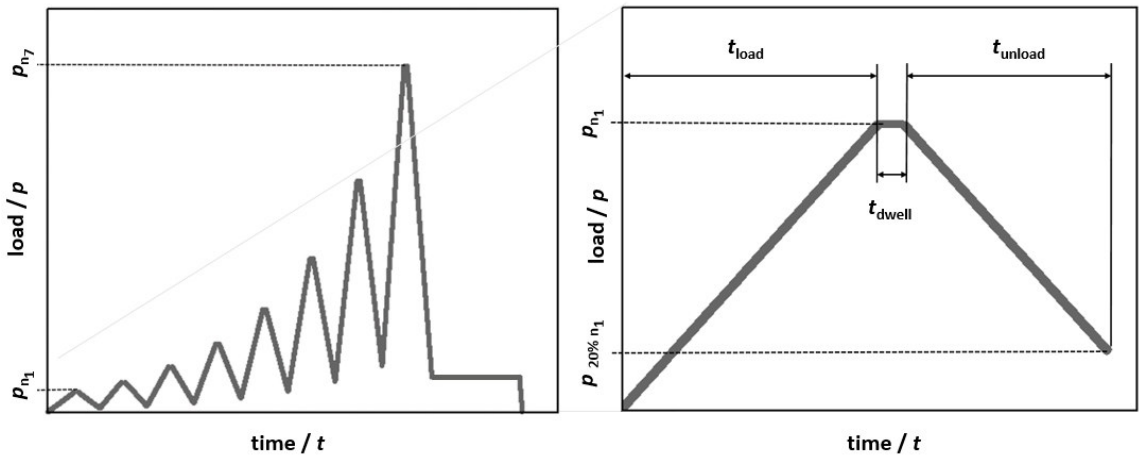

Fig. 3.4: Load – time scheme used for the cyclic test runs. On the left-hand side an overview is illustrated. The right-hand side is showing the load, dwell and unloading time as well as different loads for one segment of the scheme in detail.

Table 7: Chromium load-time schemes for the cyclic indentation runs for all used materials.

Load Controlled Experiment	load-profile (I) [mN]	load-profile (II) [mN]	loading time [s]	unlading time [s]	dwell [s]
Chromium ufg	• 8.85 • 13.25 • 19.85 • 29.65 • 44.45 • 66.75 • 100.00 • 150.00	-	15	5	5
Chromium sx	• 1.41 • 2.11 • 3.16 • 4.74 • 7.11 • 10.66 • 16.00 • 24.00	-	15	5	5

Table 8: Tantalum load-time schemes for the cyclic indentation runs for all used materials.

Load Controlled Experiment	load-profile (I) [mN]	load-profile (II) [mN]	loading time [s]	unlading time [s]	dwell [s]
Tantalum ufg	• 7.00 • 10.50 • 15.80 • 23.70 • 35.60 • 53.30 • 80.00 • 120.00	• 14.63 • 21.85 • 32.92 • 49.38 • 74.07 • 111.11 • 166.67 • 250.00	15	5	5
Tantalum sx	• 1.17 • 1.76 • 2.63 • 3.95 • 5.93 • 8.89 • 13.33 • 20.00	• 1.31 • 2.35 • 4.23 • 7.62 • 13.72 • 24.69 • 44.44 • 80.00	15	5	5

The second type of tests was focused on the determination of SRS and V^*. Owing to that, a long dwell time at peak load should guarantee a sufficient creep depth. A schematic load-time schemes for these tests is shown in Fig. 3.5, used parameters are depicted in Table 9.

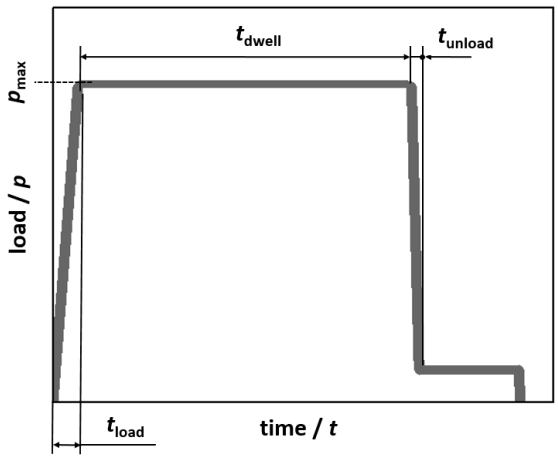

Fig. 3.5: Schematic load – time schmeses used for the long dwell time runs.

Table 9: Load-time schemes for the long dwell time runs and for all used materials.

Load Controlled Experiment	max. load (I) [mN]	max. load (II) [mN]	loading time [s]	unlading time [s]	dwell [s]
Chromium ufg	100	-	15	5	200
Chromium sx	24	-	15	5	200
Tantalum ufg	80	120	15	5	200
Tantalum sx	20	80	15	5	200

The temperatures at which the experiments were carried out were slightly different for chromium and tantalum. The reason for that was to ensure, based on the numbers of Sestak and Seeger [58], that the second elevated temperature is above T_c for the according materials. However, regarding to findings of Maier et al. [7] and Schneider et al. they [59] might in fact be very similar (≈ 450 K). The used experimental temperatures in absolute and homologous style manner can be found in Table 10 and 11 for chromium and tantalum, respectively.

Table 10: Experimental temperatures for chromium samples.

***T* [°C] Chromium**	**25**	**100**	**200**	**300**
T [K]	298	373	473	573
T / T_c [K/K]	0.66	0.83	1.05	1.27
$T_{c, Cr}$ = 450 K				
T/ T_m [K/K]	0.14	0.17	0.22	0.26
$T_{m, Cr}$ = 2180 K				

Table 11: Experimental temperatures for tantalum samples.

***T* [°C] Tantalum**	**25**	**100**	**250**	**300**
T [K]	298	373	523	573
T / T_c [K/K]	0.66	0.83	1.16	1.27
$T_{c, Cr}$ = 450 K				
T/ T_m [K/K]	0.09	0.11	0.16	0.17
$T_{m, Cr}$ = 3020 K				

3.8 Post Indentation Experimental Investigations

3.8.1 Comparison Nanoindentation Experiments

In order to verify the reliability of the originally measured data, room temperature comparison measurements on an Agilent G200 (Agilent Technologies, Chandler, AZ, USA) were performed. A similar cyclic loading procedure with the same maximum loads, as describe in chapter 3.7.3, was used to gain hardness versus contact depth data. For comparison of the *m*-values a different approach to this work was used. A description of the so called nanoindentation strain rate jump-tests can be found in [60].

3.8.2 Pile-ups and Sink-ins

In order to estimate the possible influence of pile-ups and sink-ins on the contact depth and therefore the hardness, the indents were investigated by different techniques. Light microscopy images were made for all different materials and temperatures. Moreover, indents made at room temperature were also investigated by means of SEM and AFM images. The results are presented in chapter 5.5.

3.8.3 Indent Cross-Sections

To verify a possible change of the microstructure due to grain growth at elevated temperatures and/or the plastic deformation caused by indentation, cross-sections of the 300 °C indentation runs on ufg chromium and tantalum were made using a focused ion beam workstation. These cross-sections also provide reliable information about the potential formation of an oxide layer on the surface of the material. In order to receive a distinctive and clean surface, a platinum deposition was applied on top of the indent before the milling step.

4 Results

The very focus of this chapter is to present the gained results in the clearest way possible. Hence, the most significant numbers are presented and obvious trends are described in a brief manner. In the case of unexpected results or other obvious issues the chapter numbers where to look for an in-depth discussion are named. A general discussion and comparison of the gained data with literature results is presented in the discussion chapter.

4.1 Microhardness Measurements

The ufg samples were tested such as described in chapter 3.4. The chromium specimen shows a hardness minimum of 289 HV 0.5 at the center. Measurements at a radial position of 1mm show hardness numbers of about 500 HV 0.5. After this steep increase, the further curve's slope is flatter, reaching maximum values of approximately 550 HV 0.5 at 4.5 mm off the center (Fig. 4.1a).

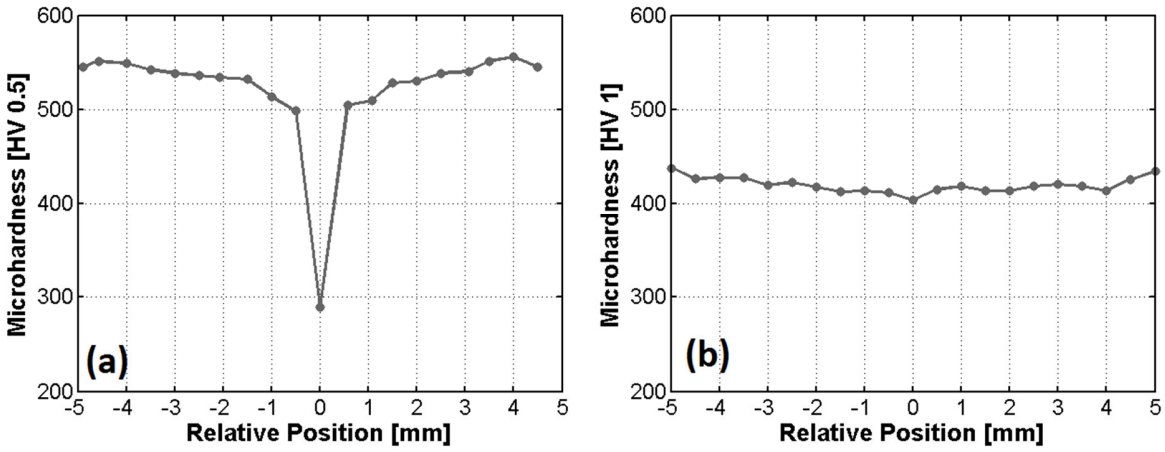

Fig. 4.1: Microhardness versus radial position of the measurements for ufg chromium (a) and tantalum (b).

The tantalum sample on the other hand does not show a hardness minimum towards the center, but instead a very evenly distributed microhardness of about 420 HV 1 with a peak value of 438 HV 1 (Fig. 4.1b). These different characteristics will be further discussed in chapter 5.1.

4.2 Microstructural Investigations

To provide sophisticated information about the evolved microstructure of the HPT processed samples, BSE investigations were performed on a chromium and EBSD investigations on a tantalum sample. As described in chapter 3.5, the BSE data were manually analyzed with a grid method, whereas the EBSD imaging allowed for an automated calculation of the grain size distributions. It needs to be pointed out, that due to the different analysis methods mentioned above, the error bars in Fig. 4.4 have different meanings. In case of the manual analysis, see Fig. 4.4a, they represent the standard deviation of the different average grain sizes measured at three different regions of the according micrographs. Whereas for the automatic analysis in Fig. 4.4b, they display the variety of different grain sizes in the entire EBSD micrograph.

The chromium sample shows an ufg microstructure (Fig. 4.2a–e) with a peak average grain size of 263 nm ± 32 nm which steadily decreases towards the edge, finally revealing a minimum of 120 nm ± 10 nm. This trend can also be seen in Fig. 4.4a. The standard deviations for the different radii where calculated using three varying spots of one according BSE image.

For the automatic grain size analysis, the minimum angle difference between two neighbors was set to 15° and the minimum size of a grain to 20 pixels. The average grain size of ufg tantalum is 138 nm ± 70 nm at the center, followed by a decrease to 114 nm ± 50 nm at radial position of 1 mm. At radial positions greater than 1 mm, the grain size is stable and in the 100 – 110 nm regime, as it is shown in Fig. 4.4b. The according EBSD micrographs are depicted in Fig. 4.3a-f.

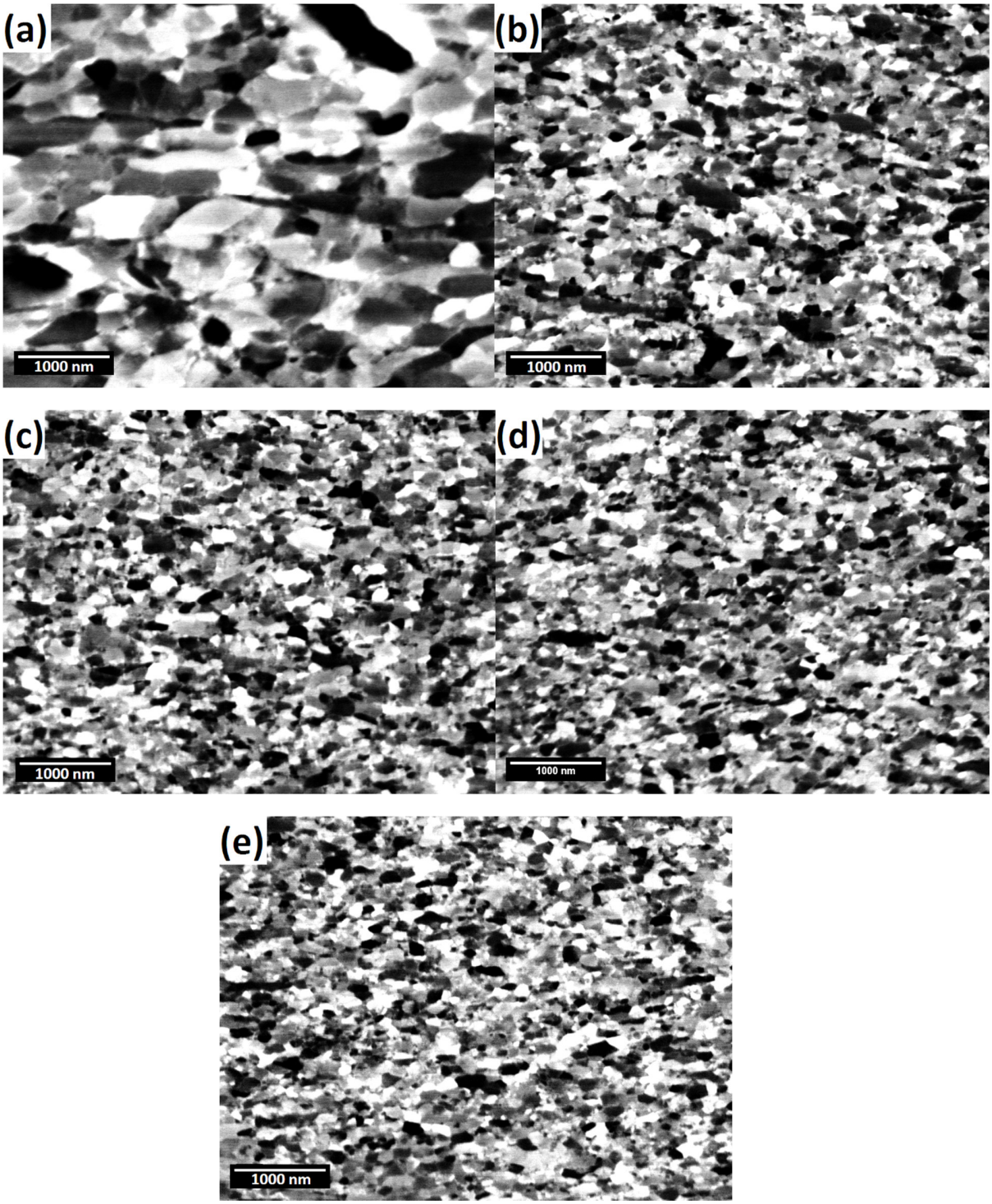

Fig. 4.2: Overview of chromium ufg microstructures determined by BSE imaging at 0.0 mm (a), 1.0 mm (b), 2.0 mm (c), 3.0 mm (d) and 4.0 mm (e).

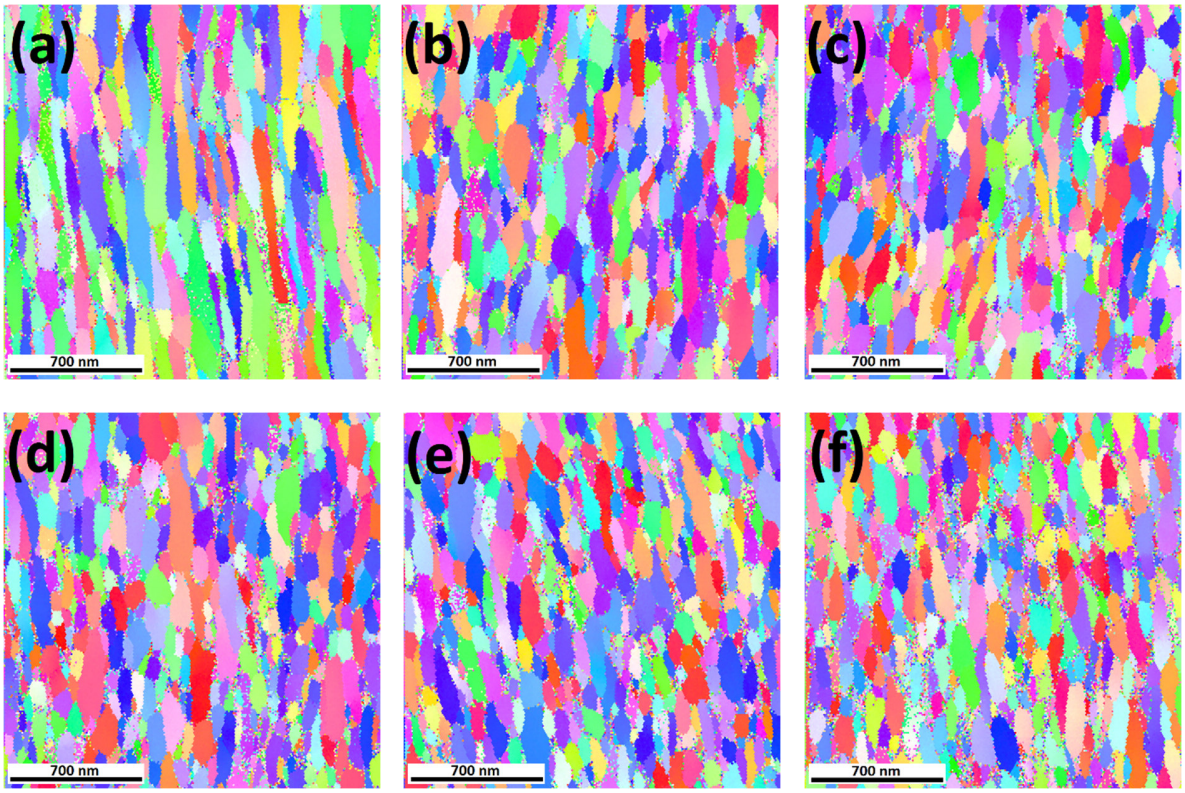

Fig. 4.3: Overview of tantalum ufg microstructures determined by EBSD at 0.0mm (a), 1.0mm (b), 2.0mm (c), 3.0mm (d), 4.0mm (e) and 4.5mm (f).

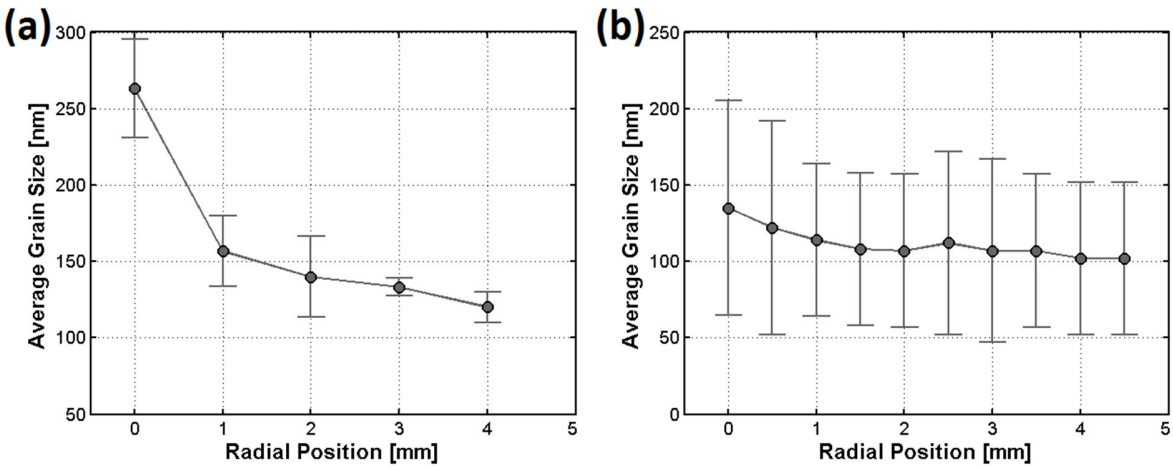

Fig. 4.4: Graphs showing the average grain sizes and corresponding deviations at different radial positions for chromium (a) and tantalum (b).

4.3 Annealing Experiments

In order to determine a possible grain growth during nanoindentation experiments at elevated temperatures, annealing runs on a chromium ufg sample where carried out. The average grain size determined as comparison number without any annealing steps was 117 nm ± 23 nm, see Fig. 4.5a, which is in good agreement to the numbers obtained at 4 mm in chapter 4.2. After a slight increase up to 140 nm at 100 °C is measured, the average grain size stays nearly constant till the 400 °C annealing step, at which it is increasing up to 167 nm ± 32 nm. Finally, after annealing at 500 °C the average grain size was determined to be 243 nm ± 15 nm. The sample was subsequently polished and its microstructure evaluated again, now showing a significantly higher number of 373 nm ± 49 nm as shown in Fig. 4.5b. The conclusion made from this annealing treatment is discussed in chapter 5.3.1.

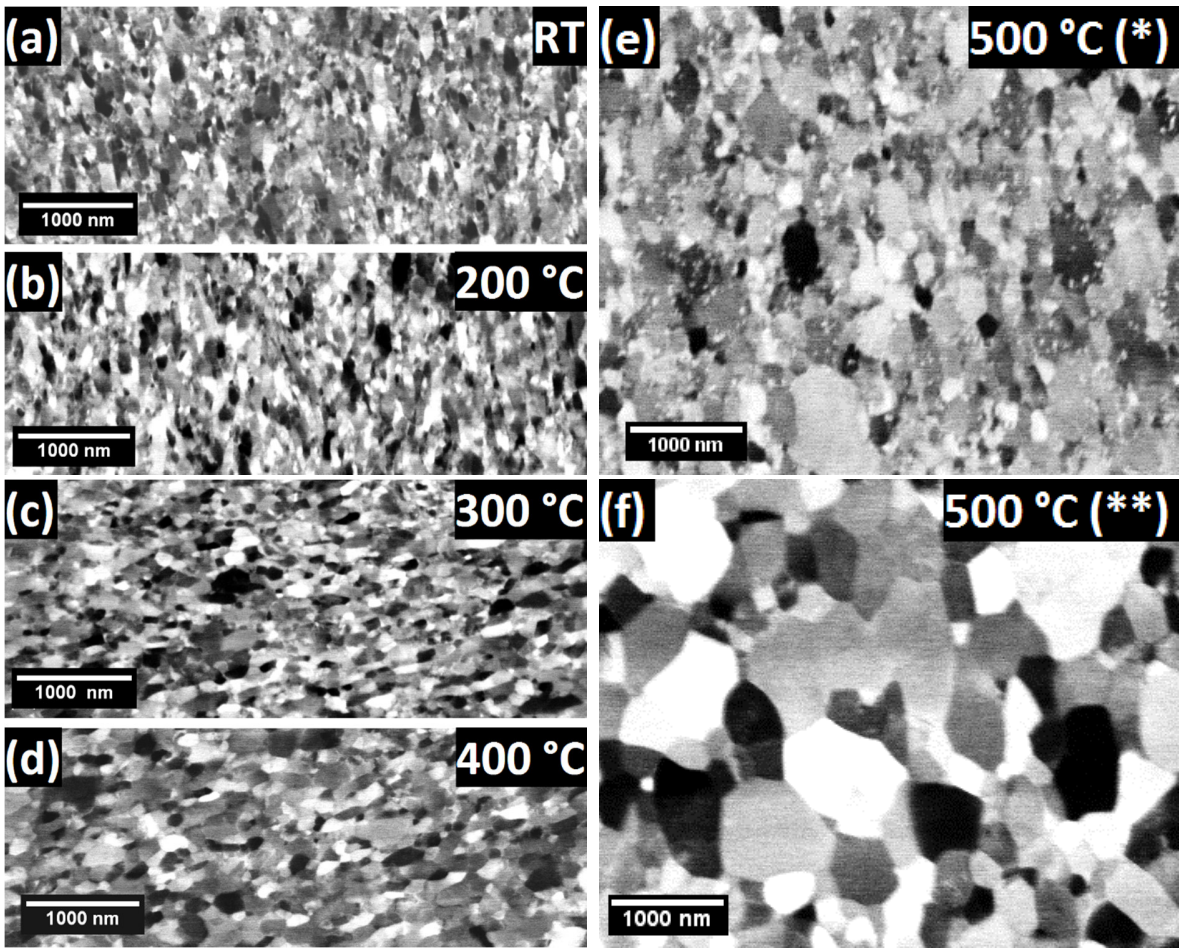

Fig. 4.5: Comparison of original (a) with microstructure after annealing treatment at different temperatures (b-f). The 500 °C annealing results are presented in non-polished (*) and newly polished (**) condition.

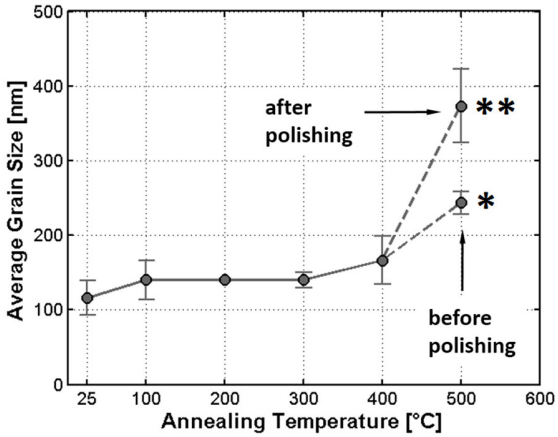

Fig. 4.6: Average grain sizes of ufg chromium ufg after annealing runs at different temperatures. Results from the 500 °C treatment are shown in non-polished (*) and newly polished (**) condition.

4.4 Nanoindentation

The nanoindentation tests were carried out according to chapter 3.7. For each material and temperature several indents were made with the cyclic loading scheme, see Table 7, to evaluate hardness and Young's modulus as well as pop-in data in terms of the single crystals. With the 200 s dwell time scheme, see Table 9, creep data were generated in order to access time dependent properties such as strain rate sensitivity and activation volume. To accommodate for the high number of indents and for the sake of clarity, in the following chapter averaged numbers with standard deviation or especially representative behavior of individual indents is presented in terms of the hardness and the creep data, respectively.

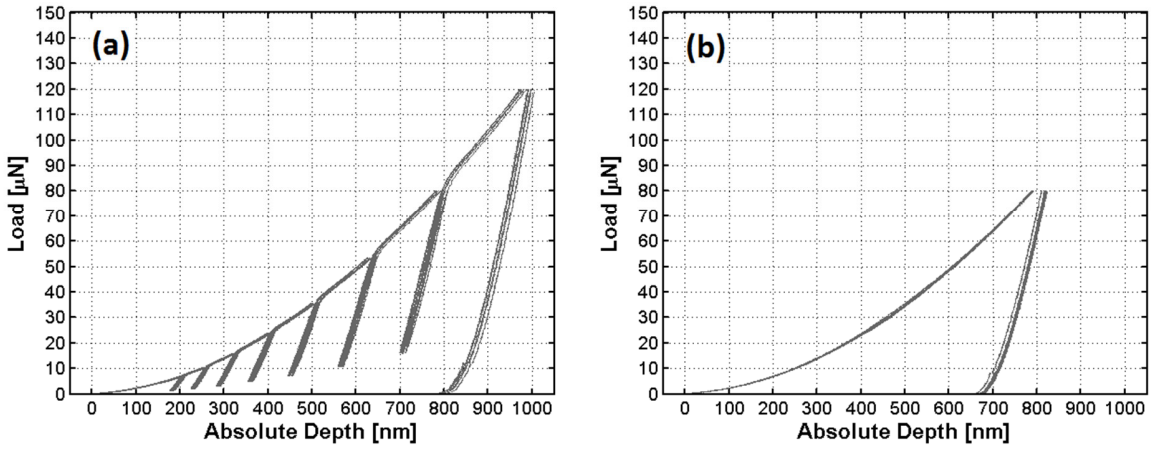

Fig. 4.7: Materials load-displacement response of ufg tantalum at room temperature to a cyclic (a) and to a 200 s loading scheme (b).

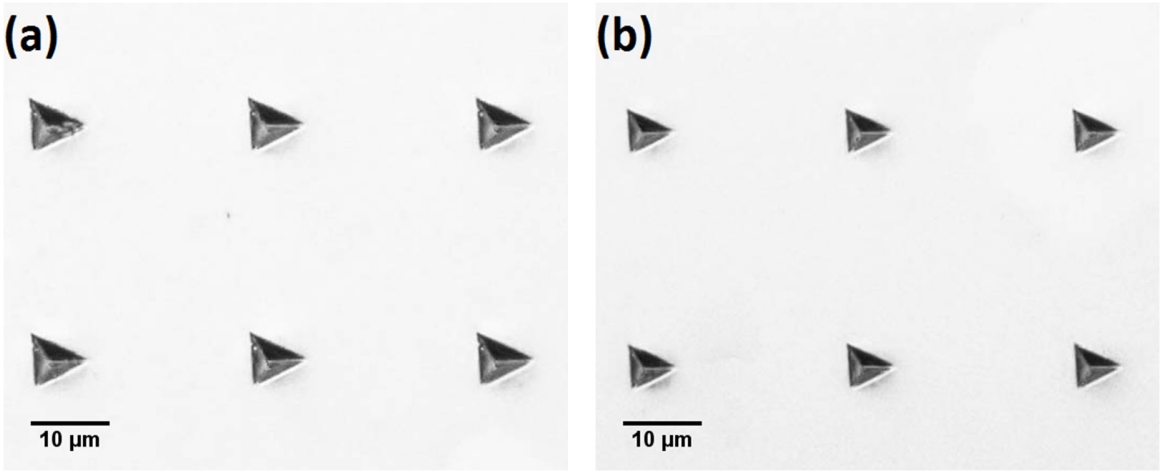

Fig. 4.8: Light microscopy images of residual indents after a cyclic (a) and a 200 s loading scheme (b).

All the indents were made with a minimum lateral distance of 30 µm among each other to guarantee that plastic deformation introduced by indentation does not influence the measurements of subsequent indents. Fig. 4.7a and b show the load depth response of the material to the different loading schemes for a tantalum ufg sample at room temperature consisting of six indents each. Fig. 4.8a and b show the corresponding light microscopy images of these indents.

At the end of every unloading step, a 60 s thermal drift correction segment was attached in order to obtain the drift rate which is caused by a non-isothermal contact of the tip and the sample. The derived corrections were applied to all data presented. In some cases issues occurred with this type of drift correction. The most notably were inconsistent drift measurements and excessive correction values. If one indent of the set was predominantly affected by obvious errors caused by the drift correction, it was precluded from the further calculation procedure.

Furthermore, in chapter 5.5 results of a pile-up and sink-in analysis are presented, which indicate the presence of such contact depth altering material behavior. Nevertheless, the following results presented in this chapter are, due to the lack of a sophisticated correction method, non-pile-up corrected.

Finally, it needs to be mentioned that, though hardness and Young's modulus numbers beneath a contact depth of 200 nm are presented in chapter 4.4.1, these might be influenced by an imprecise area function of the indenter tip in this low depth regime. Since especially hardness numbers at low contact depths exert a strong influence on the indentation size effect analysis, presented in chapter 4.4.2, these were neglected for this kind of analysis.

4.4.1 Hardness and Young's modulus

In this chapter the harndnesses for different depths at several different temperatures are shown next to similar plots of the Young's modulus. Unless otherwise stated, the results are observed from loading profiles denoted as "(I)", see Table 7 and Table 9. At least three indents per temperature were used to calculate the average and standard deviation values. The focus of this chapter is rather to present the gained results than compare and discuss them in detail. A comparison with literature values and data gained from microhardness testing, as well as an in depth discussion about possible error sources and their influence on the results is given in chapter 5.6.1 and 5.6.2

Chromium: Ultrafine Grained State

The hardness of ultrafine grained chromium is steadily decreasing with increasing temperature, as it can be seen in Fig. 4.9a. Moreover, all curves show a differently strong pronounced descend of hardness with increasing contact depth, which gets in general more prominent at elevated temperatures. The hardness numbers range from 6.76 ± 0.19 GPa to 6.32 ± 0.15 GPa at ambient temperature and from 5.17 ± 0.27 GPa to 4.14 ± 0.12 GPa at 300 °C.

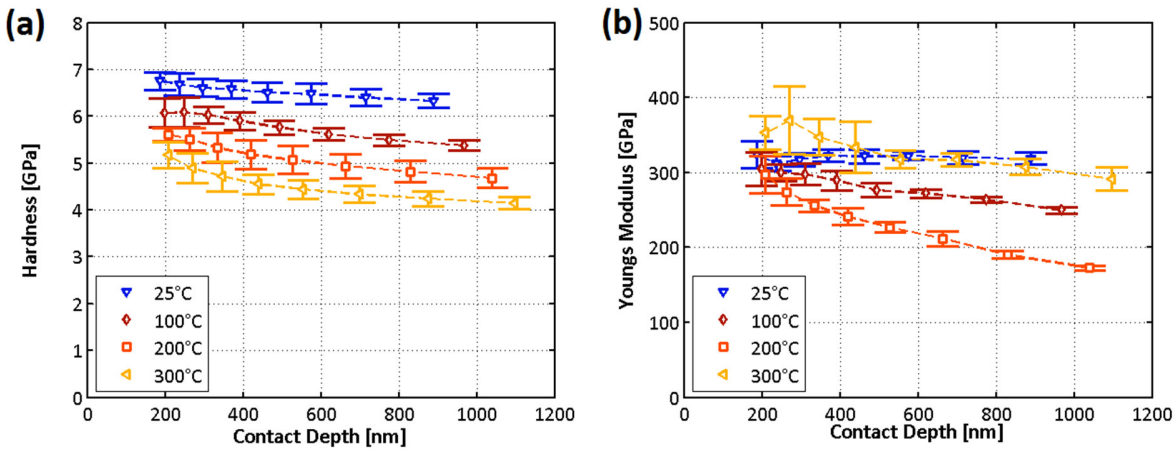

Fig. 4.9: Hardness and Young's modulus of ultrafine grained chromium versus contact depth measured at 25, 100, 200 and 300 °C.

The Young's modulus - shown in Fig. 4.9b – is approximately constant over depth for the room temperature and 300 °C measurements with average values of 320 ± 10 GPa and 330 ± 33 GPa, respectively. The 200 and 300 °C curves show decreasing numbers with increasing contact depth, starting at 282 ± 21 GPa and 234 ± 31 GPa, respectively. This unexpected dependence of the Young's modulus on the contact depth will be further discussed in chapter 5.6.3.

Chromium: Single Crystalline State

Depth-dependent hardness with different slopes is observed for all curves as shown in Fig. 4.10a. At room temperatures the numbers are ranging from 2.01 ± 0.09 GPa to 1.82 ± 0.06 GPa, at 300 °C from 1.25 ± 0.04 GPa to 1.04 ± 0.03 GPa. The general trend of decreasing hardness with increasing temperatures holds true except for the measurements at 300 °C, showing marginally higher numbers compared to those measured at 200 °C.

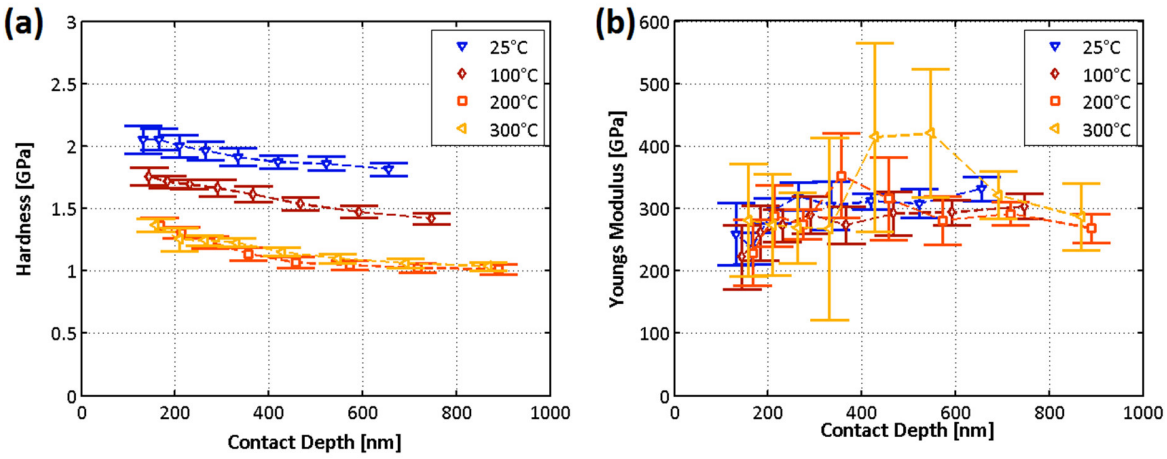

Fig. 4.10: Hardness and Young's modulus of single crystalline chromium versus contact depth measured at 25, 100, 200 and 300 °C.

The Young's modulus results are presented in Fig. 4.10b. They exhibit slightly lower values for all temperatures in a contact depth regime beneath 300 nm, compared to values obtained above. Furthermore, the numbers gained at 200 and 300 °C show the highest standard deviations in terms of Young's modulus of all measurements. The averaged numbers are 312 ± 26 GPa, 287 ± 28 GPa, 297 ± 49 GPa and 330 ± 112 GPa at room temperature, 100, 200 and 300 °C, respectively.

Tantalum: Ultrafine Grained State

The slopes of the hardness curves steadily increase from room to the maximum temperature of 300°C, as shown in Fig. 4.11a. Whereas the hardness numbers at high contact depths are, at least up to the 250 °C measurement, decreasing as expected, those at lower contact depths are unexpectedly high for 250 and 300 °C. This behavior is so distinctive that at low depths, the hardness at 300 °C exceeds those measured at room temperature by approximately 1.4 GPa. The values range from 5.19 ± 0.17 GPa to 4.80 ± 0.13 GPa at room temperature and from 6.62 ± 0.34 GPa to 3.70 ± 0.31 GPa at 300 °C. This hardening behavior at elevated temperatures, but particularly from 250 °C on, is unexpected and demands an in-depth discussion in order to find a sophisticated explanation. This will be attempted in chapter 5.7.

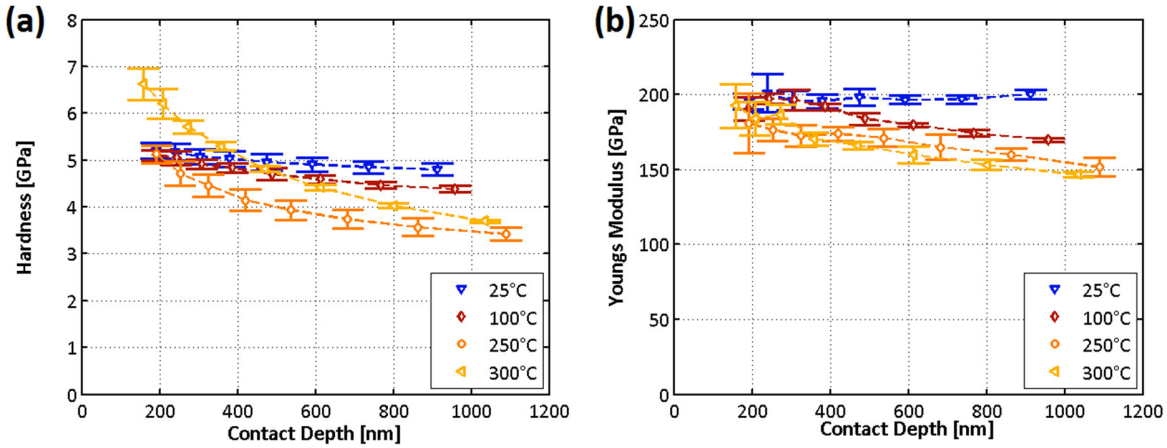

Fig. 4.11: Hardness and Young's modulus of ultrafine grained tantalum versus contact depth measured at 25, 100, 250 and 300 °C.

The Young's modulus, see Fig. 4.11b, is continuously decreasing from room temperature to 300 °C, where all results, except for those obtained at room temperature, show a certain depth dependence. The averaged values range from 197 ± 6 GPa at room temperature to 170 ± 17 GPa at 300 °C

Tantalum: Single Crystalline State

Similar to the behavior of tantalum ufg, the single crystalline samples show a very prominent hardness increase when measured at 250 and 300 °C. Towards higher depths, the hardness at those temperatures is strongly decreasing, as shown in Fig. 4.12a. The hardening even seems to diminish at certain depths of over 1500 nm, which is the reason why the 250 and 300 °C numbers presented are from load profile (II) measurements. The values range from 1.87 ± 0.08 GPa to 1.32 ± 0.03 GPa at room temperature and from 5.51 ± 0.15 GPa to 1.06 ± 0.04 GPa at 300 °C. As for the ufg tantalum, this behavior will be discussed in detail in chapter 5.7.

An overview of the tantalum sx Young's Moduli can be found in Fig. 4.12b. Though showing different depth-dependent behavior, the average values are, except for the 100 C measurement, quite close. The numbers are 184 ± 17 GPa at room temperature, 157 ± 14 GPa at 100 °C, 184 ± 24 GPa at 250 °C and 182 ± 23 GPa at 300 °C.

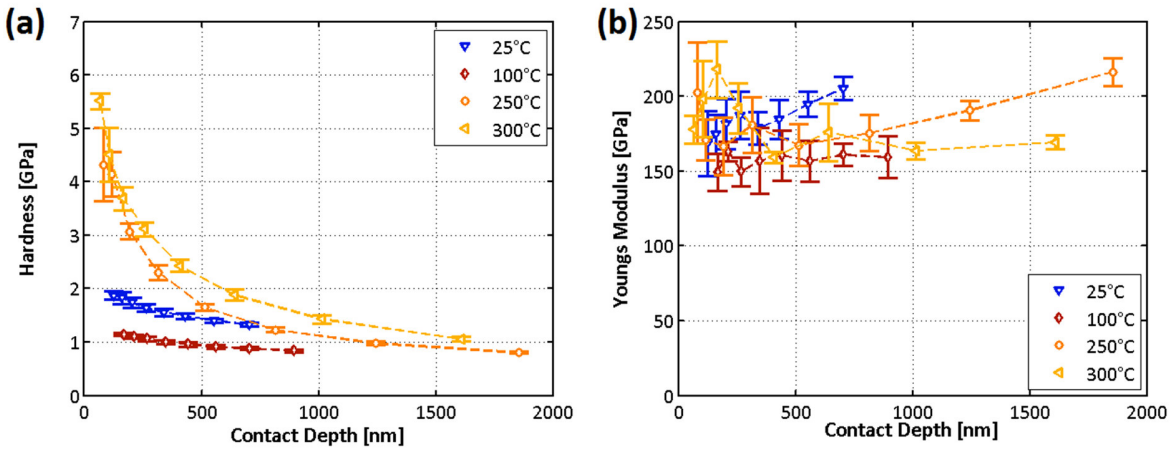

Fig. 4.12: Hardness and Young's modulus of single crystalline tantalum versus contact depth measured at 25, 100, 250 and 300 °C. The 250 and 300 °C results are observed from indents made with load profile (II).

4.4.2 Indentation Size Effect

The size effect was directly obtained from hardness and contact depth data presented in the previous chapter. The macroscopic hardness H_0 and the internal length scale parameter h^* were calculated using data fitting according to Eq.(24). An overall overview of the results is given in Fig. 4.13. However, in the following chapter Nix-Gao fits are presented for all temperatures in terms of chromium and at room temperature as well as 100 °C in terms of the tantalum. This approach is made since the already mentioned tantalum hardening effect, which is discussed in chapter 5.7, prevents a meaningful analysis regarding indentation size effect of the 250 and 300 °C data of ufg and sx tantalum.

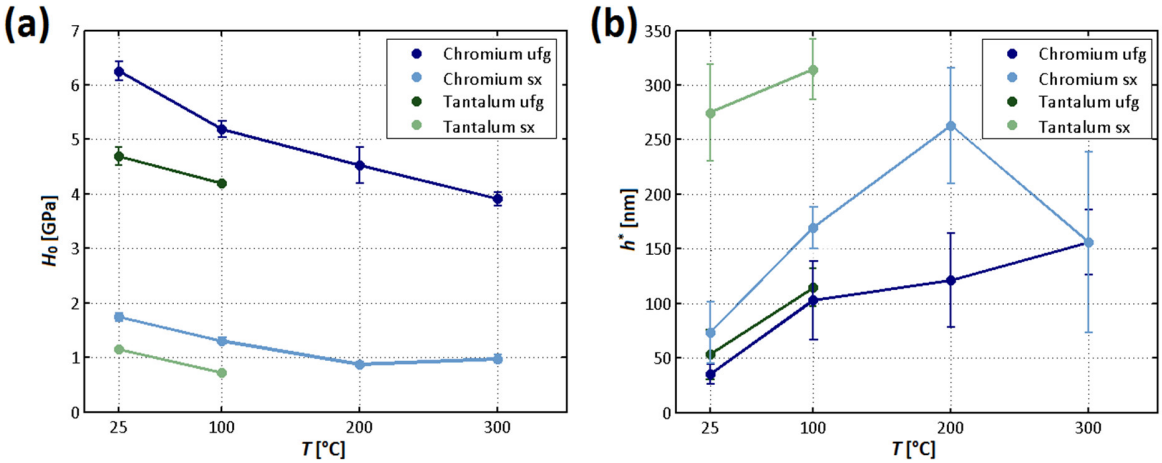

Fig. 4.13: H_0 (a) and h^* (b) results overview for all microstructural constitutions and temperatures.

Chromium

The macroscopic hardness for the ultrafine grained chromium, see Fig. 4.14a, is continuously decreasing from 6.25 GPa at room temperature, to 3.91 GPa at 300 °C. This is accompanied by increasing numbers of h^*, which are 32 nm and 156 nm at ambient temperature and 300 °C, respectively.

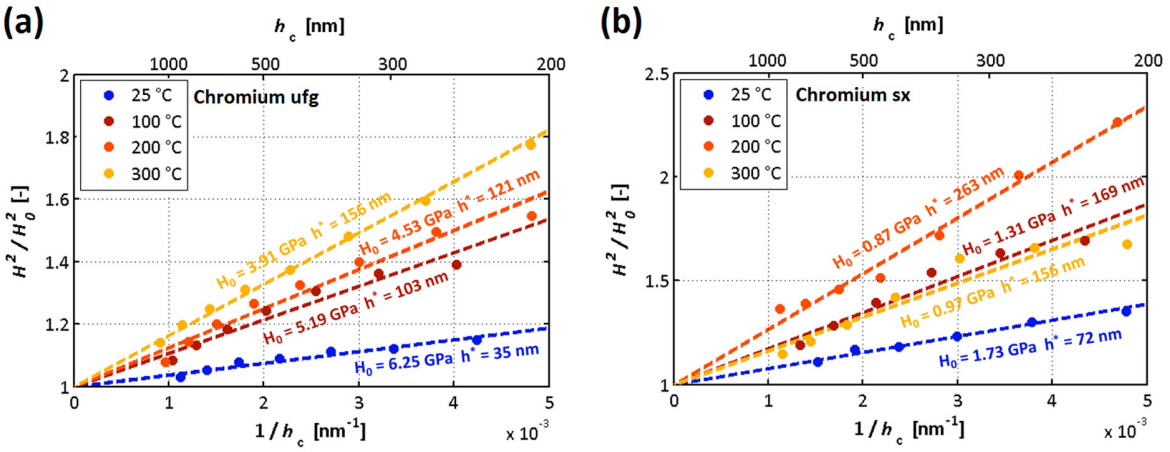

Fig. 4.14: Nix-Gao plots for different temperatures of chromium ufg (a), and chromium in sx state (b).

The results for the single crystalline chromium are presented in Fig. 4.14b. Except for the 300 °C results, the general behavior is likewise to the ufg chromium. The macroscopic hardness is decreasing beginning from 1.73 GPa at room temperature, to 0.87 GPa at 200 °C. This is again coupled with an increase of h^* from 72 and 263 nm, respectively. The data at 300 °C reveal an increase in hardness to 0.97 GPa and an decrease in h^* to 156 nm. The increase of hardness is rather unexpected and will be discussed in chapter 5.6.2.

Tantalum

The tantalum samples with different microstructural constitutions behave, in the temperature range of room temperature to 100 °C, similarly to the chromium – see Fig. 4.15a. For the ufg sample H_0 is decreasing from 4.70 to 4.19 GPa, whereas h^* is increasing from 52 to 115 nm.

Macroscopic hardness for the single crystalline tantalum is 1.14 and 0.73 GPa for room temperature and 100 °C, respectively. The internal length scale parameter increases from 273 to 314 nm for the mentioned temperatures as shown in Fig. 4.15b.

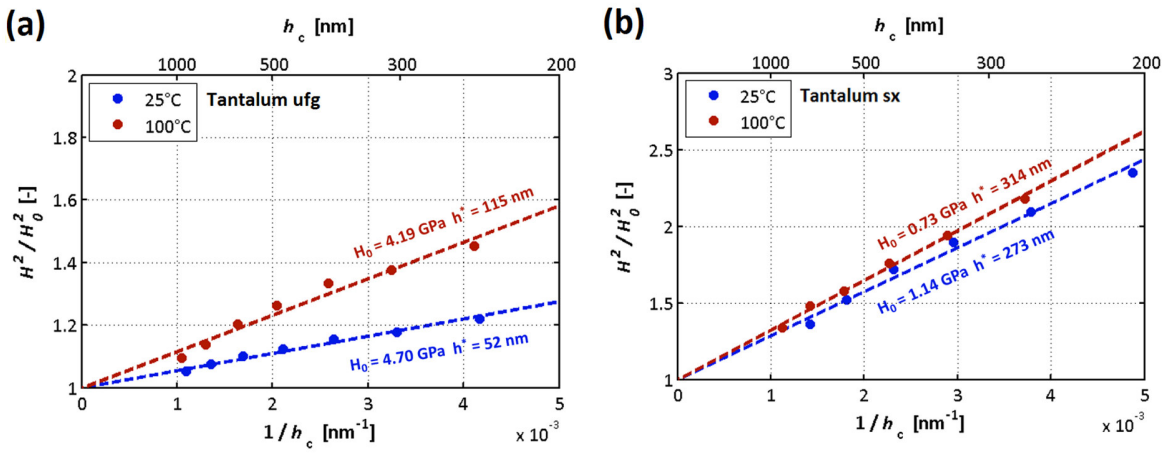

Fig. 4.15: Nix-Gao plots for different temperatures of tantalum ufg (a), and tantalum in sx state (b).

4.4.3 Strain Rate Sensitivity and Activation Volume

Strain rate sensitivity and activation volume were derived from creep data measured with 200 s dwell time load profiles as shown in chapter 3.7.3. An overview of the time dependent data used to calculate the SRS and activation volume is given exemplarily for ufg chromium in Fig. 4.16. The further results in this chapter are presented as Norton plots (double logarithmic strain rate versus stress plots), SRS versus strain plots and as activation volume versus stress plots, in two different ways. On one hand the mentioned plots are presented in a continuous manner where the whole creep curve is used. On the other hand as particular stage A analysis was used, which is described in chapter 2.4.5. For each material and temperature, at least three valid indents were obtained. However, contrary to the previous chapter, the results shown are obtained from single representative indents, rather than from a set of indents. This is since plotting the averaged numbers with the according standard deviations would strongly exacerbate a clear presentation of the results.

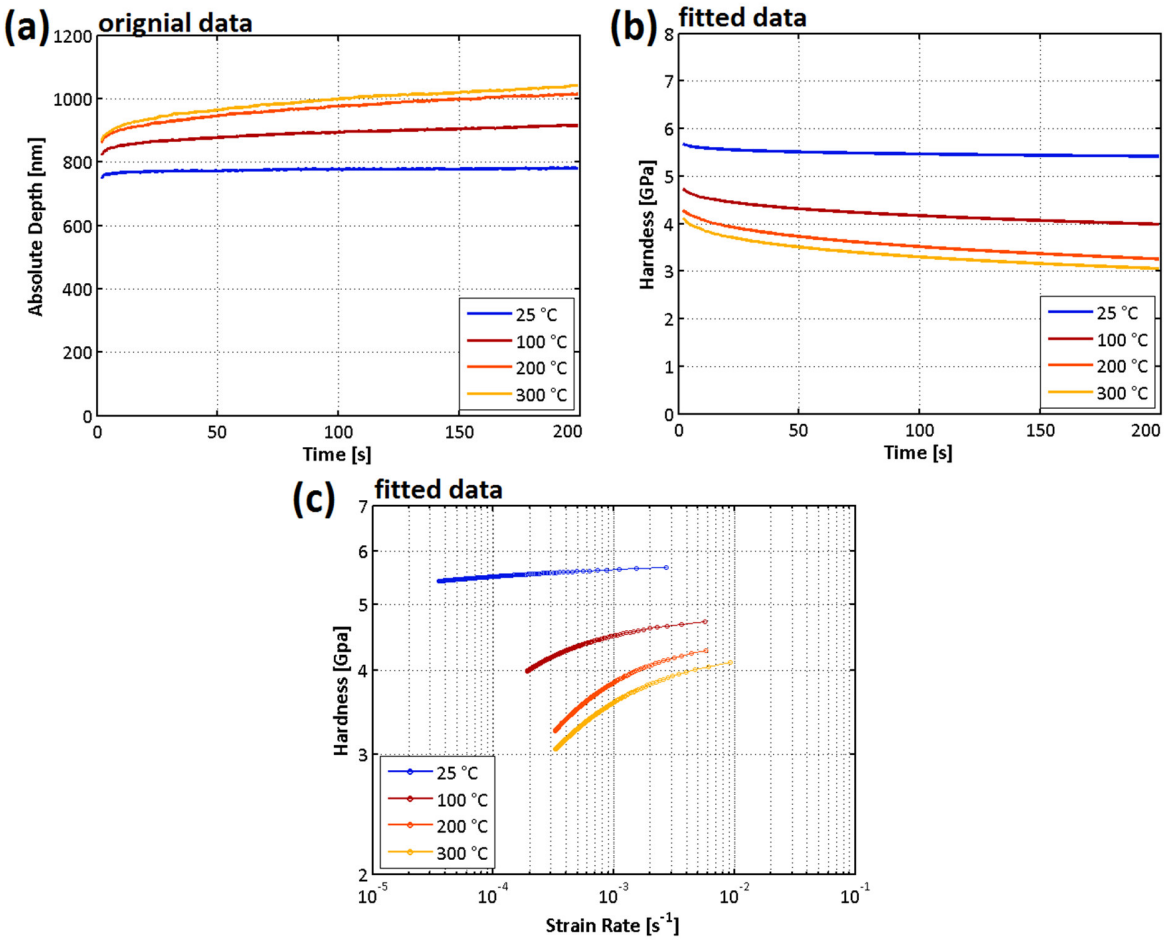

Fig. 4.16: Creep depth and Hardness versus time (a, b), as well as the corresponding hardness versus strain rate plot (c) for chromium ufg.

Chromium: Ultrafine Grained State

Creep rates start in the magnitude of 10^{-3} s^{-1} whereby there is a trend of increased starting and end creep rate with the elevation of temperature as shown in Fig. 4.17a,d.

Experiments conducted at ambient temperature provided SRSs spanning from 0.007 to 0.016 at approximately 1.96 GPa. The according values at 300 °C include numbers from 0.033 to 0.186 at averaged 1.20 GPa stress. The 100 and 200 °C numbers - see Fig. 4.17b,e - are situated in between, demonstrating the general trend of increasing SRS with increasing temperature.

The activation volume at room temperature ranges from 14 to 33 b^3 and at 300 °C from 4 to 18 b^3. Whereas the 100 °C and 200 °C numbers are well comparable with those gained at 300 °C as presented in Fig. 4.17c,f.

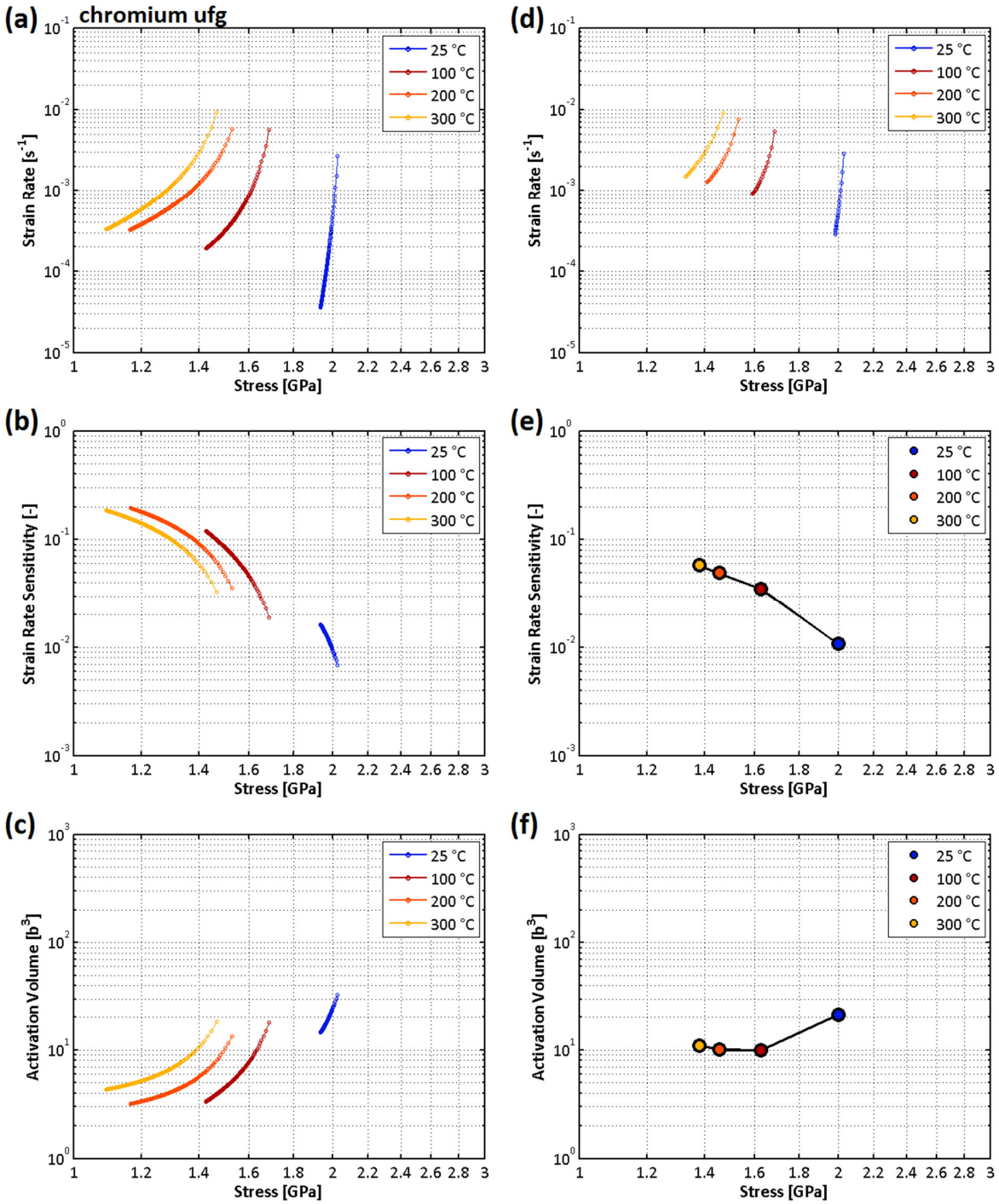

Fig. 4.17: Strain Rate (a), strain rate sensitivity (b) and activation volume (c) of ultrafine grained chromium versus stress measured at 25, 100, 200 and 300 °C. Similar plots showing the analysis of stage A (d), (e), (f).

Chromium: Single Crystalline State

The Norton plots, see Fig. 4.18a and d, reveal creep rates starting in the range of 10^{-3} s^{-1} for all temperatures, being lowest for the 100 °C curve. The lowest creep rate, after 200 s dwell, is in the order 10^{-5} s^{-1} and also relates to the 100 °C measurement.

The SRS plots, Fig. 4.18b and e, show an initial decrease from 0.024 - 0.055 at room temperature to 0.010 - 0.035 at 100 °C, which is eventually followed by an increase of the SRS numbers to nearly identical numbers of 0.023 - 0.101 at 200 and 300 °C. However, there is a noticeable difference for the stage A analysis, proposing different SRS at 200 and 300 °C, namely 0.038 and 0.049, respectively.

The general trend of the activation volume, as presented in Fig. 4.18c and f, is a low quantity of 16 - 31 b^3 at ambient temperature, followed by increased numbers at elevated temperature. The SRS range for the 300 °C measurements is 30 to 111 b^3.

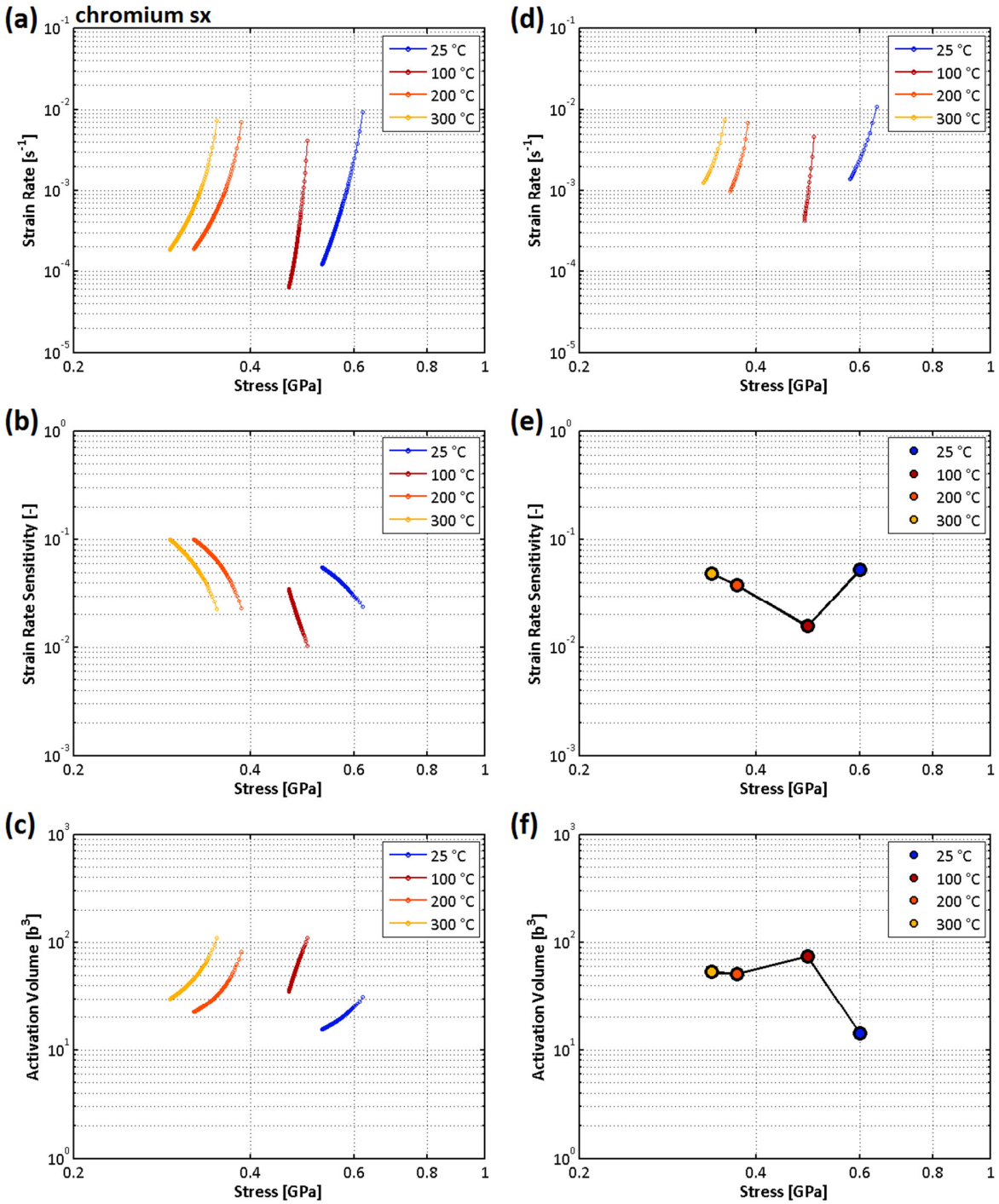

Fig. 4.18: Strain rate (a), strain rate sensitivity (b) and activation volume (c) of single crystalline chromium versus stress measured at 25, 100, 200 and 300 °C. Similar plots showing the analysis of stage A (d), (e), (f).

Tantalum Ultrafine Grained

The highest creep rates, observed at the start of the dwell time, are in the order of several 10^{-3} s^{-1} for all temperatures, as shown in Fig. 4.19a and e. It is remarkable that the creep stress of the 300 °C measurement is situated above those of the 250 °C run, though a continuous decrease with increasing temperature is expected. This behavior seems to correlate with the hardening at elevated temperatures which was already observed in chapter 4.4.1 and will be discussed in chapter 5.7.

The SRS, presented in Fig. 4.19b, is continuously increasing from 0.005 - 0.01 at room temperature to 0.028 – 0.406 at 250 °C. The 300 °C SRS curve ranges from 0.040 to 0.202 and therefore has a higher minimum, but a lower maximum SRS. The SRS stage A analysis, see Fig. 4.19e, shows a steady increase from room temperature to 300 °C of 0.013 to 0.103.

The activation volume exhibits a trend similar to the SRS. The stage A numbers, see Fig. 4.19f, are decreasing in a continuous manner from 16 b^3 at room temperature, to 4.4 b^3 at 300 °C. The continuous curves presented in Fig. 4.19c show the maximum numbers spanning from 22 to 41 b^3 as well at room temperature. The minimum activation volume is, however, 1.5 b^3 at 250 °C.

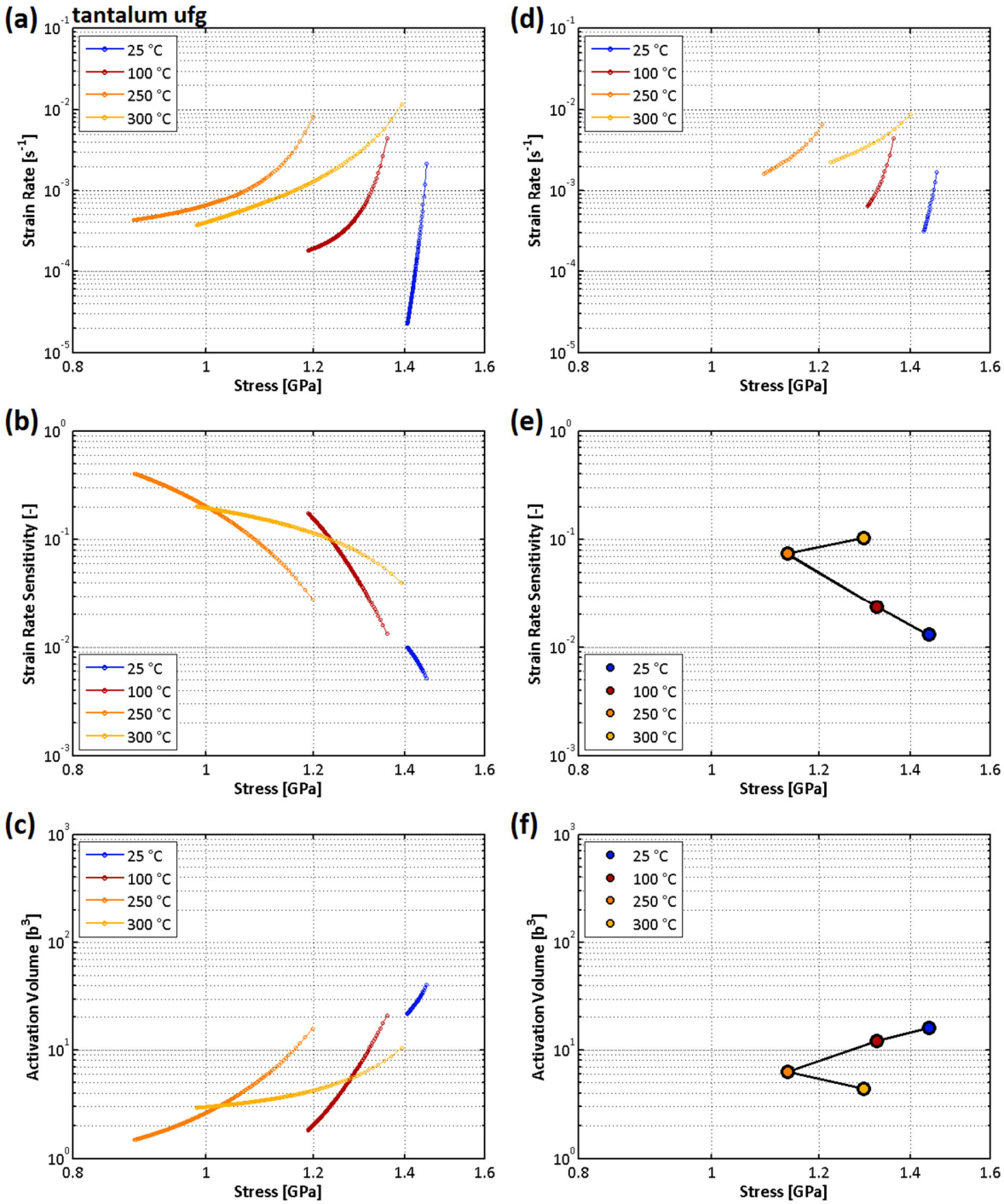

Fig. 4.19: Strain rate (a), strain rate sensitivity (b) and activation volume (c) of ultrafine grained tantalum versus stress measured at 25, 100, 250 and 300 °C. Similar plots showing the analysis of stage A (d), (e), (f).

Tantalum Single Crystalline

Norton plots, presented in Fig. 4.20a and e, reveal starting creep stresses initially decreasing from approximately 0.4 GPa at room temperature to 0.3 GPa at 100 °C. These are eventually succeeded by creep curves starting at 0.5 GPa for the 250 °C and even 0.7 GPa for the 300 °C experiments. As for the ufg material, this hardening effect and its possible consequences for the experimental results are discussed in chapter 5.7.

The SRS is initially decreasing from 0.022-0.055 at room temperature, to 0.011 - 0.022 at 100 °C. The succeeding SRSs at elevated temperatures are eventually increasing to 0.013 - 0.074 at 250 and 0.032 - 0.258 at 300 °C. The trend of the stage A analysis is similar. The corresponding plots are shown in Fig. 4.20b and e.

The activation volume, see Fig. 4.20c and f, is behaving accordingly, increasing from 16 – 35 b^3 at room temperature, to 64 – 116 b^3 at 100 °C. The numbers at 250 and 300 °C are reduced again, being 16 - 80 b^3 and 4.3 - 26 b^3, respectively.

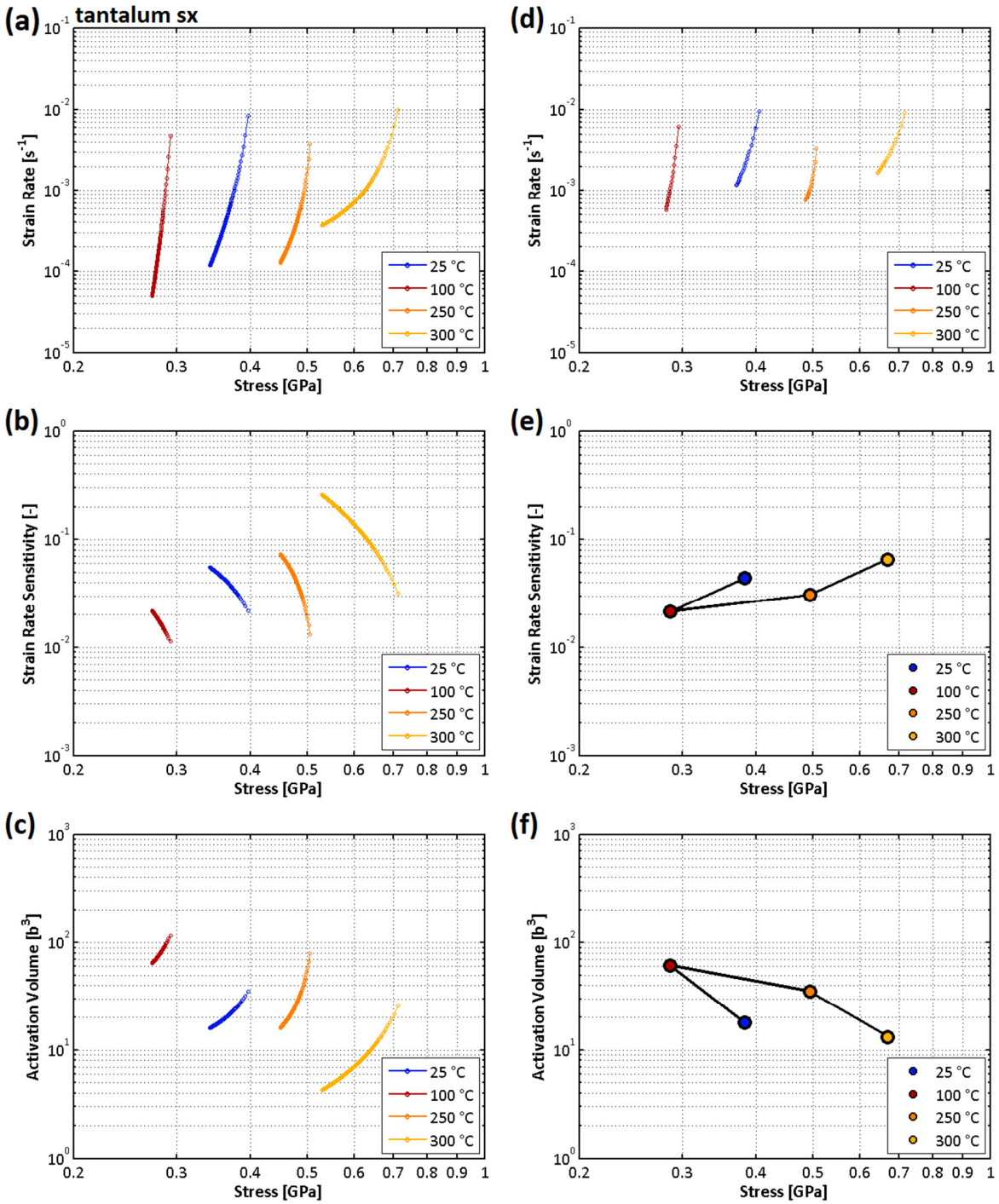

Fig. 4.20: Strain rate (a), strain rate sensitivity (b) and activation volume (c) of single crystalline tantalum versus stress measured at 25, 100, 250 and 300 °C. Similar plots showing the analysis of stage A (d), (e), (f).

4.4.4 Incipient Plasticity

In the following chapter the pop-in behavior of sx chromium and tantalum is presented in terms of pop-in load distribution, pop-in load versus pop-in excursion, and relative strength plots.

In order to compare the shear stress at the occurrence of a pop-in event, τ_{max}, with the theoretical strength of an idealized crystal τ_{th} (see chapter 2.4.7), the radius of the tip of the Berkovich indenter, which was assumed to be spherical, needed to be evaluated. This was eventually done according to chapter 2.4.6 using reduced moduli calculated with Eq.(23) and literature values for chromium, tantalum and diamond, namely 294 GPa, 186 GPa and 1147 GPa [52], respectively. Since the high temperature experiments are more likely to be influenced by thermal drift and decreased moduli of the material, these were not used for the tip radius evaluation. The high temperature runs might even affect the data gained post-experimentally, which is why the evaluation of the tip radius was done with a special focus on results obtained at room temperature before heating. A representative example for the pop-in behavior and according fits of the elastic loading part of an sx tantalum sample at room temperature are shown in Fig. 4.21. The resulting tip radius for these loading curves is 439 ± 30 nm.

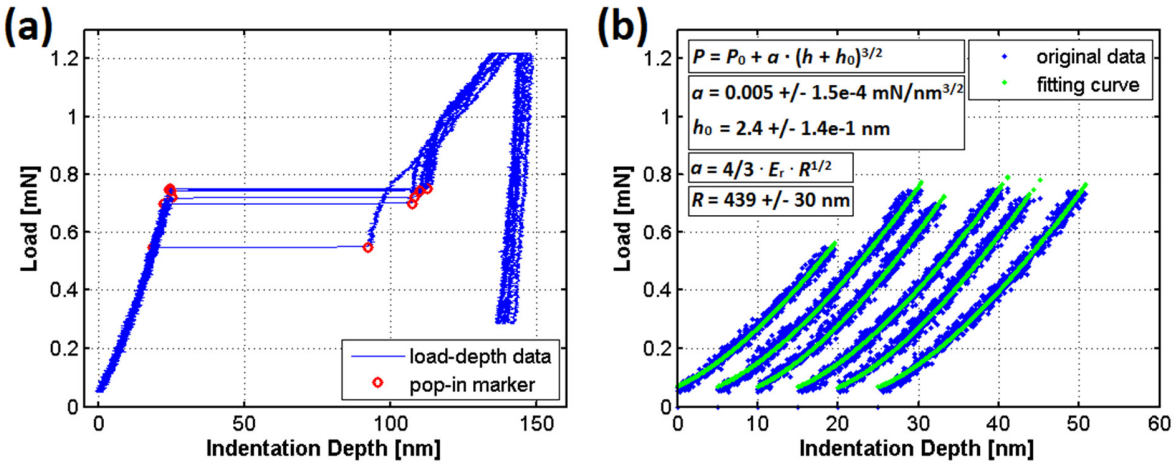

Fig. 4.21: Load versus depth plot of sx chromium at room temperature showing characteristic pop-in behavior (a) and the elastic loading part before the pop-in with the according Hertz fitting (b).

Even with the mentioned restrictions to the used data, the determined effective tip radii were fluctuating between 350 nm and 550 nm for different data. It was furthermore found that the calculated tip radii tend to increase with increasing pop-in load. Finally, the tip radius calculation gives somewhat higher numbers for the 300 °C experiments. However, due to the general scattering of the radii, these effects were hard to quantify. Therefore, an average tip

radius of 450 nm was used for all results presented in the following chapter. A brief discussion, covering possible tip wear, is given in chapter 5.4.

Besides the explicit room temperature sample, pop-in experiments were also carried out at ambient temperature before and after the high temperature runs. But not only is the sheer number of available indents lower at elevated temperatures, also the probability of unambiguous pop-in events decreased for both materials with rising temperature. The results of the explicit room temperature sample and all pre-heating room temperature tests are presented together as “RT” in the following charts. Those made after the high temperature experiments are named “RT*” for the 100 °C sample, “RT**” for the 200 °C and 250 °C samples and “RT***” for the 300 °C sample. The 200 °C and 250 °C data do further contain results gained at the according temperatures obtained on the 300 °C sample from intermediate measurements.

Chromium: Single Crystalline State

Altogether 101 pop-in events were observed on the four different chromium samples. A general trend is that the overall loads at which they occur is decreasing with rising temperature, as shown in Fig. 4.22a. It is also apparent that the variation of the pop-in loads is most pronounced for those at room temperature. These range from approximately 0.1 mN up to 2.5 mN, whereas those at elevated temperatures are less scattering.

Fig. 4.22b demonstrates the relationship between the load at a pop-in event and the according excursion width. Pop-in events at elevated temperatures, as well as those after heating, are presented. There are two apparent trends: The excursion width is continuously increasing with increasing pop-in load, and the excursion width at a given load is increasing with temperature. It should be further noted, that all post high temperature indents are on the same curve as the explicit room temperature and pre heating pop-ins.

Finally, Fig. 4.22c shows the ratio of $\tau_{pop\text{-}in}$ to τ_{th} ($\tau_{th,Cr} \approx 18.3$ GPa) for all individual indents, as well as averaged numbers. Due to the high scattering of $\tau_{pop\text{-}in}$ at room temperature, the minimum (0.30) and maximum (0.88) relative strength values were obtained at this temperature. As for the pop-in loads, the relative shear strength is decreasing with rising temperature, being 0.64 at ambient temperature and 0.44 at 300 °C in average. The indentation runs at room temperature after the high temperature tests revealed strength numbers in the range of those observed at room temperature before heating. This is only with the exception to RT***, where the average relative shear strength is modestly decreased to 0.52.

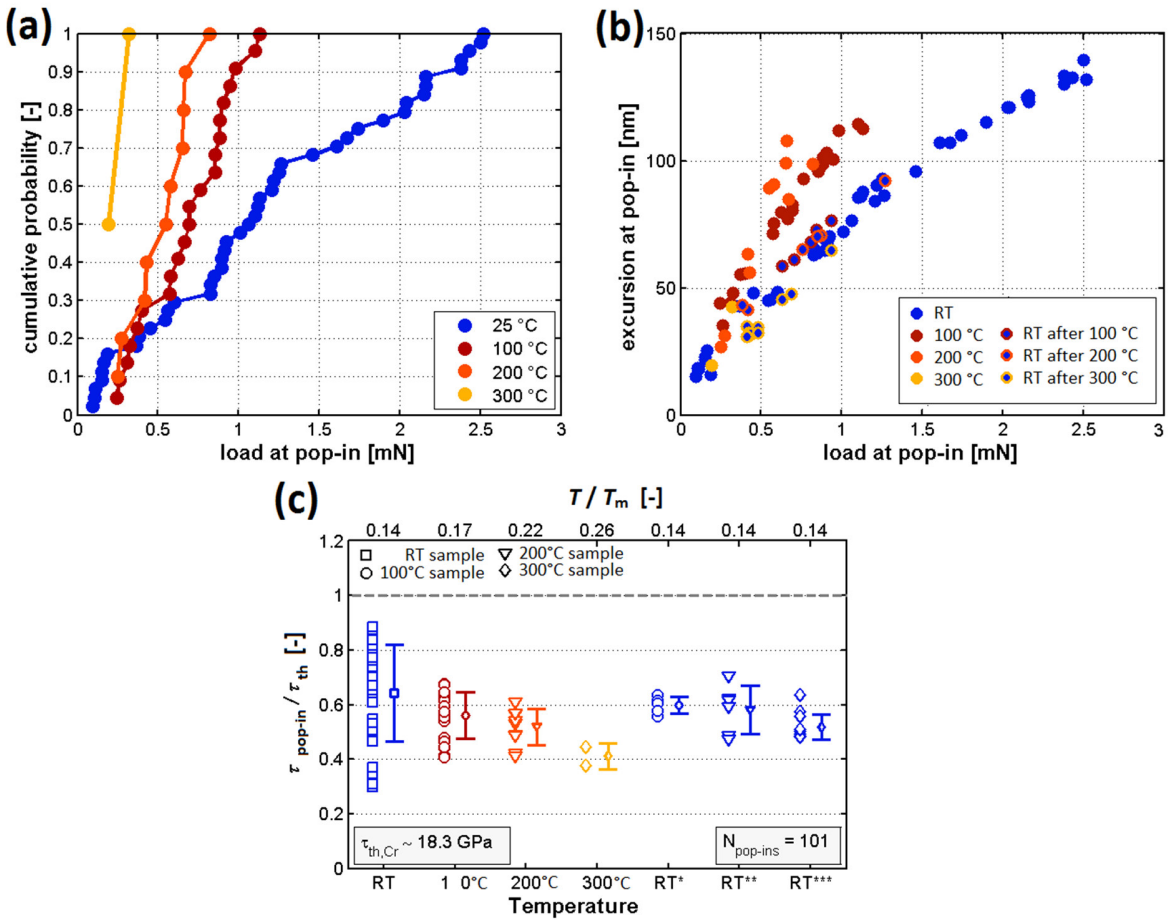

Fig. 4.22: Overview of pop-in events obtained at different temperatures on sx chromium plotted as cumulative probability (a) and pop-in excursion (b) versus pop-in load, as well as relative theoretical strength versus temperature (c).

Tantalum: Single Crystalline State

For the tantalum samples 118 pop-ins were observed at different temperatures. In general, the temperature dependence on the pop-in load, see Fig. 4.23a, is more complex than for the sx chromium samples discussed before. The pop-in load data gained at room temperature and those at 300° C exhibit the most scattering, ranging from approximately 0.2 to 2 mN. It is also apparent, that there is no clear trend of decreasing pop-in load with increasing temperature. Instead, only the 100 °C data show a distinctive decrease of the pop-in load compared to the room temperature data

Excursion width versus pop-in load is plotted in Fig. 4.23b, revealing an interesting behavior. Whereas the ratio of excursion width to load is increased for the 100 °C data, compared to initial room temperature measurements, this ratio is decreased for data acquired at 250 °C and 300 °C. Moreover, the post heating room temperature ratios of the 250 °C and 300 °C samples

are decreased, compared to original room temperature measurements, as well. This is thought to be another aspect of the tantalum hardening effect already mentioned in this work. An in-depth view on that issue will be made in chapter 5.7.

The average relative shear strength ($\tau_{th,Ta}$ ≈ 11 GPa), see Fig. 4.23c, keeps approximately constant for all temperatures, though the high scattering needs to be noticed. At ambient temperature, the relative shear strength is approximately 0.78, which equals 8.6 GPa. In the RT* experiments, only two pop-ins were obtained. However, their shear strength is in very good accordance to the averaged numbers at room temperature. A completely different picture is given by the RT** and RT*** tests, which reveal an enormous increase of shear strength after the 250 and 300 °C tests. Certain pop-ins even exceed the theoretical strength of tantalum. This behavior is again attributed to a tantalum hardening effect discussed in chapter 5.7.

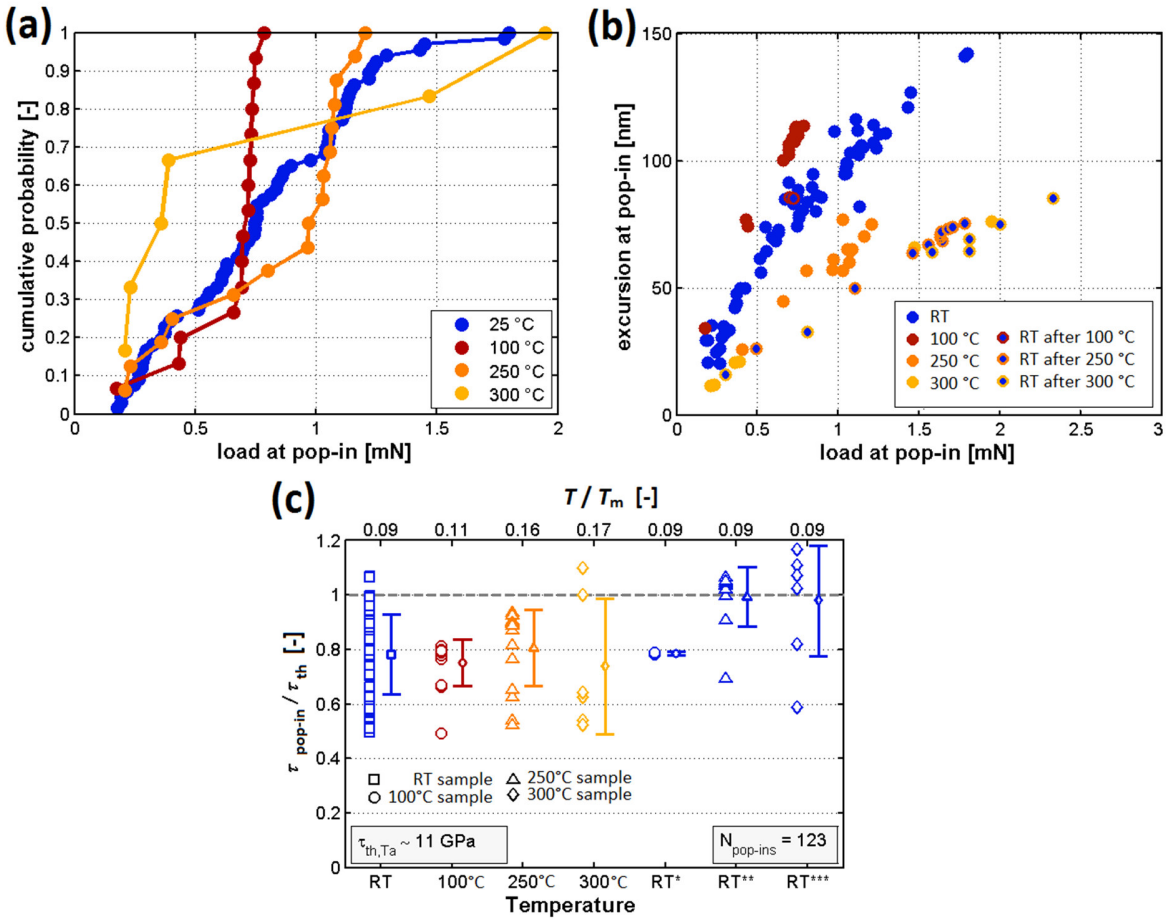

Fig. 4.23: Overview of pop-in events obtained at different temperatures on sx tantalum plotted as cumulative probability (a) and pop-in excursion (b) versus pop-in load, as well as relative theoretical strength versus temperature (c).

4.4.5 Activation Energy

The activation energy Q_a was directly derived from the macroscopic hardness numbers presented in chapter 4.4.2. An overview of the different activation energies is given in Fig. 4.24. It is obvious that the ratio of hardness to Young's modulus is well comparable between the two materials for the corresponding microstructures. Moreover, it is also noticeable that the numbers of the ufg material are lower compared to the sx. It needs to be mentioned that the macroscopic hardness of chromium sx at 300 °C was suspiciously slightly higher than at 200 °C. This issue was already mentioned in chapter 4.4.2. Thus, the activation energy between 200 and 300 °C is a physically not meaningful negative number and hence not depicted. Since the Young's modulus decrease at elevated temperatures is expected to be negligible (see Fig. 2.3), the room temperature values of 294 GPa and 186 GPa were used for chromium and tantalum, respectively.

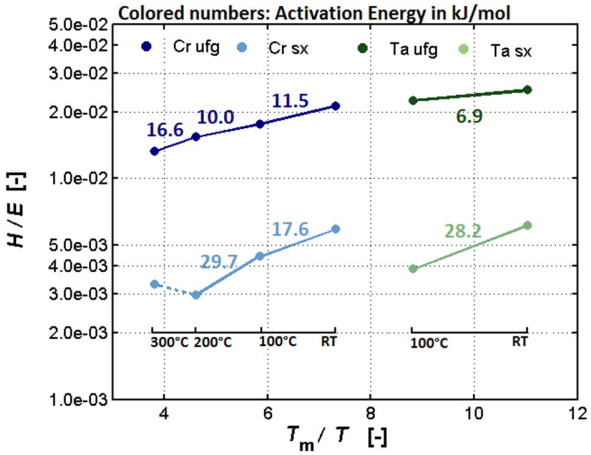

Fig. 4.24: Comparison of the activation energies derived from H_0 values for all materials at different temperatures.

5 Discussion

The main focus of this chapter is to compare the results presented in chapter 4 with available literature data and discuss mismatches and their possible reasons as well as very general issues which might have occurred during the measuring procedures.

5.1 Microhardness

Chromium: Ultrafine Grained State

The microhardness distributions of the ufg hpt samples presented in the chapter 4.1, have different shapes. On one hand, the chromium sample shows, as it is typical for hpt manufactured specimens, a significant hardness minimum of 289 HV 0.5 at the center of the disc. This is caused by the hpt process, which induces plastic strain as a function of the radius, being minimum in the center and maximum at the edge. As reference see Eq.(8). At a material dependent amount of strain, a steady state is reached and no further grain refinement or hardening occurs [61]. This behavior can be seen in Fig. 4.1a, explaining the even hardness distribution of the outer radial regimes. The maximum microhardness of the chromium sample was determined to be 550 HV 0.5, which is about 13 % more than Lee et al. [62] report for their ufg chromium. This difference is strongly believed to emerge from different grain sizes investigated, being as low as 120 nm in this work, but 200 nm in the work of Lee et al. Moreover, the different purity levels of the used materials influence the resulting harndnesses. Though the chromium used for this work exhibits a higher purity of 99.99 % compared to the 99.9 % reported in the reference work - therefore suggesting higher hardness numbers than the samples of this work – the mere impurity level does not necessarily give significant information for such estimations, as Rathmayer et al. [63] showed for hpt processed fcc nickel. Taking these influential parameters into account, a hardness mismatch of close to 10 % seems justifiable.

Tantalum: Ultrafine Grained State

As shown in Fig. 4.1b, the tantalum hpt sample is lacking a hardness minimum in the center. In Table 3 (chapter 2.2.2) several reasons for the disappearance of the characteristic minimum are discussed. In fact, the most probable cause is an acentric cut of the sample.

The average hardness of the tantalum was 420 HV 1, which is approximately 5 % higher compared to literature values [64] which minors the probability of insufficient strain insertion. Thus, the missing minimum is probably caused by an off-centered cut of the sample.

5.2 Microstructure of HPT Samples

Chromium: Ultrafine Grained State

The evaluated steady state grain size of hpt processed chromium was approximately 120 nm and therefore significantly lower than the 200 nm reported by Lee et al. [62], but close to the results of Provenzano et al. [65] which determined about 100 nm. The corresponding hardness numbers of these works are, like the Hall-Petch relation suggests, inversely proportional. Moreover, the incipient strong decline of the grain size from the center position of the sample to a radial position of 1 mm, see Fig. 4.4a, as well as the following moderate decline are in very good agreement with the corresponding hardness numbers depicted in Fig. 4.1a. The noticeable high error bars in the grain size graph are a result of the wide grain size distribution, containing smaller and larger features close to each other. This was already found for hpt processed chromium by Wadsack et al. [66]. A microstructure comparison of hpt chromium of this work and Wadsack et al. is given in Fig. 5.1.

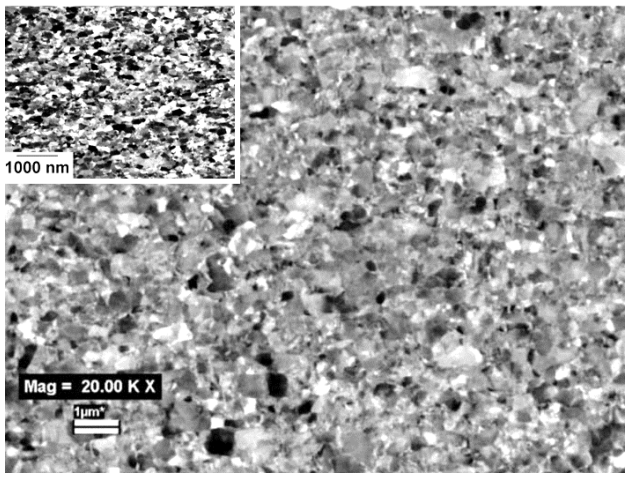

Fig. 5.1: Micrographs showing a hpt saturation microstructures of chromium produced from a 4N sx (this work, small picture) and from a 3N polycrystal ([66], large picture).

The main difference between these micrographs is the presence of larger grains in the sample of Wadsack et al., whereas the small features are of comparable size. This finding is not unexpected, since ten revolutions were applied to the sample in this work, while Wadsack et al. conducted only two.

Tantalum: Ultrafine Grained State

As shown in Fig. 4.4b, the average grain size of the hpt tantalum is only slightly dependent on the radial position, ranging from about 138 nm at central positions to 114 nm at a radial positon of 4.5 mm. Compared to Edalati et al. [64] and Wei et al [20] reporting 180 nm and 40 nm, respectively, the average grain size numbers are situated right in between, showing not only the influence of different production procedures used in these works, but likewise the difficulty of gaining reliable numbers at these small length scales. The 40 nm were observed from an ECAP sample with TEM imaging, allowing for higher resolution compared to the EBSD technique used in this work. Hence it enables the consideration of very small grains and small angle grain boundaries for the average grain size calculation. This fact might have led to a slight overestimation of the presented average grain sizes due to insufficient capabilities in terms of resolution. Some of the EBSD images presented in Fig. 4.3, but especially the one at the center positon, do show a certain degree of elongation. Although Zhilyaev et al. [32] reported about elongated grains in the center of hpt-processed nickel, the high aspect ratio of the grains presented in Fig. 4.3a is more likely to be a result of mechanical drift, rather than a microstructural feature, since the hardness at the center position of the disc (see Fig. 4.1b) is not substantially decreased. Besides that, the small dimension of the grains is of interest and therefore even moderately elongated grains are expected to behave similar.

5.3 Influence of High Temperature Experiments on Microstructure and Possible Oxygen Layer Growth

5.3.1 Vacuum Furnace Annealing Experiments

In order to evaluate possible grain growth during high temperature nanoindentation, annealing experiments were conducted on ufg chromium. It was assumed that, in the case of no grain growth in the concerned temperature range of up to 300 °C for ufg chromium, ufg tantalum, owning a far higher melting temperature, would not be affected either. Furhtermore single crystalline samples are assumed to be non-affected by high temperature experiments. From the conducted annealing tests, see Fig. 4.6, it is concluded that no significant grain growth has occurred up to an annealing temperature of 300 °C to 400 °C. However, after

annealing at 500 °C the grain size was evaluated before and after a subsequent polishing step, whereas no intermediate polishing was conducted for the other temperatures. It is very interesting to note, that the grain sizes measured before and after polishing clearly differed from each other. Consequently, since the sample was only measured in a polished state before annealing and after the 500 °C run, it is hard to determine at which exact temperature grain growth first occurred. Provenzano et al. [65] reported small coarsening for ufg chromium after annealing at 400 °C for 30 min. Keeping the only negligibly different grain sizes up to 300 °C of the recent work in mind, it is most likely that substantial grain growth took first place at the 400 °C or 500 °C annealing steps. In order to affirm this assumption, microstructural investigations were made for high temperature nanoindentation samples.

5.3.2 Cross Section Investigations of Residual Indents

The annealing experiments, which are discussed in the previous chapter, proposed a temperature region of 400 °C to 500 °C at which significant grain growth of the ufg chromium might occur. However, there was a noticeable mismatch in grain sizes for the 500 °C sample after a new polishing step. Hence, a grain growth even at lower temperatures, where no intermediate polishing was conducted, could not be completely excluded. A further concern to be investigated is the possible growth of the natural oxide layer on the surface of tantalum. The chromium is not supposed to be subject to any significant oxide layer growth due to its excellent passivation behavior [67]. For both mentioned interests the investigation on cross sections of room temperature and 300 °C indents is a feasible method. The temperatures in between were not investigated, since it is assumed that the sensitivity for grain and oxygen layer growth is most pronounced at the highest temperatures. All pictures presented in the following chapter are captured with a secondary electron (SE) detector and are only cropped and brightness enhanced.

To obtain SEM images of indents' cross sections, a focused ion beam (FIB) workstation was used. As a first step platinum in a rectangular shape was deposited from a pre-cursor as it can be seen in Fig. 5.2a. This is to protect the material surface and enable the observation of oxide layers with a certain thickness. In Fig. 5.2b the cutting process can be seen in the coarse (high current) setting leading to streaks (vertical lines) in the cross section. A subsequent fine cut step removes the streaks, giving a clean cross-sectional surface as shown in Fig. 5.2c. The grain sizes to be obtained are in the 100 nm range, which is close to the resolution limits of the used detector in the FIB. Thus, an ion beam etching step on the cross sectional surface was subsequently performed. The etching rate of the ion beam is depending on the orientation of the grains, leading to a certain height profile [68]. Eventually, the topography enhances the contrast due to shading effects. The etching current used was 0.3 nA for chromium and 0.1 nA for the tantalum sample.

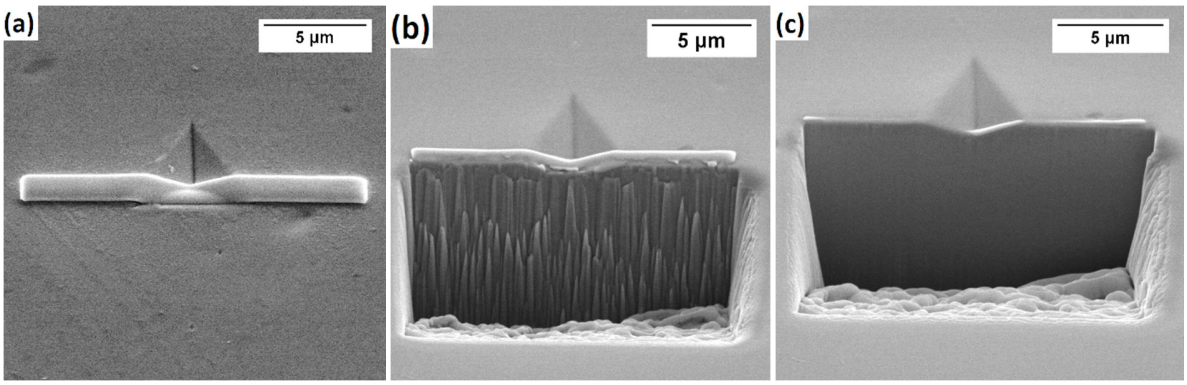

Fig. 5.2: Workflow of a cross-section cut on a chromium ufg sample showing the indent with the platinum depletion (a), the cross section after the coarse (b) and after the fine cut step (c).

Additionally to the mentioned benefits of the cross-section investigation, in theory also the previously discussed pile-ups, see chapter 5.5, should be observable. In practice, this is only hard to accomplish, since the pile-up heights of the ufg materials are supposed to be in the range of 100 nm, whereas the SEM images have a size of several micrometers. Owing to this fact, pile-ups in the cross-section images cannot be precisely identified.

Chromium: Ultrafine grained State

The microstructure beneath the analyzed room temperature indent, see Fig. 5.3a, is well comparable with the microstructure obtained from the BSE measurements presented in chapter 3.5. The deposited platinum layer serves as a well-defined bright boarder to the cross section surface with no further layer in between. The cross section of a 300 °C indent is shown in Fig. 5.3b. One might assume that the grain size in the 300 °C sample is slightly increased. However, due to the fine grain structure and the limited resolution of the available micrographs, a reliable conclusion weather slight grain coarsening took place or not, is hard to make. At this point, it needs to be mentioned that after a detailed review of the original indentation data, obtained before and after the high temperature experiments, no hint regarding a decreased hardness and therefore grain coarsening was found. Furthermore, comparison nanoindentation measurements were conducted on a different system, leading to similar results as obtained for the dedicated room temperature sample. It might be therefore concluded that, even if slight gain growth has occurred for ufg chromium at 300 °C, its effects regarding hardness were in the range of the experimental fluctuations.

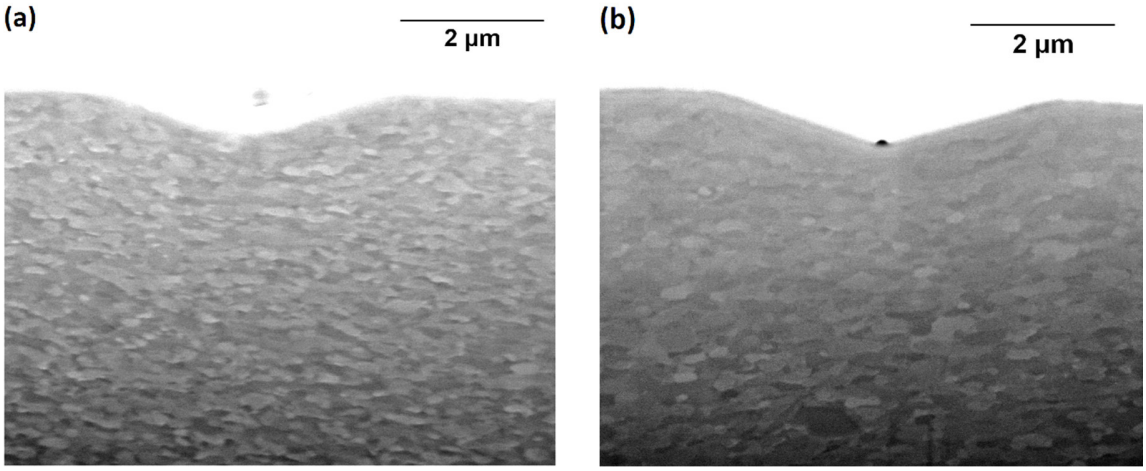

Fig. 5.3: Cross sections on ufg chromium indents conducted at room temperature (a) and at 300 °C (b).

Tantalum: Ultrafine grained State

The investigated cross sections of dedicated room temperature and 300 °C samples showed a similar microstructure, as shown in Fig. 5.4a and b. The shallower appearance of the 300 °C samples cross section, compared to its room temperature counterpart is related to an off centered FIB cut. Moreover, it was resized in order two have scale bars of equal lengths for both images. Although much more of the platinum layer is left after cutting and etching on the room temperature sample, it is also evident for the 300 °C sample that no oxygen interlayer is apparent. However, it needs to be mentioned that the resolution limits of the used SEM probably do not allow to verify the presence of very thin oxygen layers. What in fact can be proven, is that no thick oxide layer in the order of 10 nm was formed.

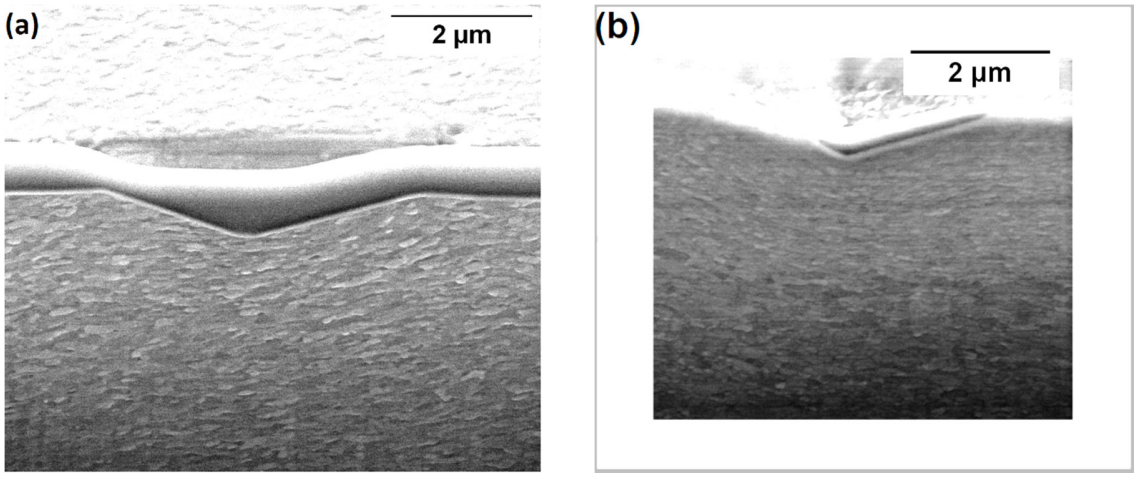

Fig. 5.4: Cross sections on ufg tantalum indents conducted at room temperature (a) and at 300 °C (b).

After the analysis of the cross sections some important statements can be made. For none of the investigated samples an oxide layer was observable between the platinum deposition and the material beneath the indent. Since the formation of oxides is for thermodynamic reasons preferential at higher temperatures, it is assumed that oxide layers have not grown up to a thickness which would be obtainable by the described SEM approach at 300 °C or lower temperatures. Furthermore, there is no hint for a change of microstructure in terms of ufg tantalum, whereas the microstructure of the 300 °C ufg chromium might have been subject to a slight growth. However, the nanoindentation systems used where not able to detect a significant difference regarding hardness.

5.4 Area Function Determination and Usage

In order to receive reliable hardness numbers, the determination of the area function is of crucial importance. Area function calibration measurements were therefore carried out on a fused silica (FS) sample, in order to avoid any influence stemming from ISE or pile-ups. However, some area function measurements suffered from an underestimation of hardness at up to 400 nm depth. These were neglected from further use. For the eventual calculations in this work, two different area functions were used, which do not display deviations above 200 nm indentation depth. The first, referred as "AF_1", was obtained before any other experiments were conducted. The second, "AF_2", was determined for the 300 °C runs. The determined geometry constants C_1 to C_3 are presented in Table 12. It is evident that the negative values of C_3 for both area functions are not physically meaningful. However, since the determination of these coefficients is a mathematical approach, working with the principle of least squares, such solutions occur

Table 12: Overview of the area function coefficients.

	C_1 [-]	C_2 [nm]	C_3 [$nm^{1.5}$]
• **AF_1**	27.64	2348	-7093
• **AF_2**	27.29	3533	-14099

The data from the calibration measurements itself, analyzed by means of the according area functions, are depicted in Fig. 5.5a. As can be seen, an excellent agreement of the data with the 8.8 GPa hardness of FS [69], is achieved, especially above 200 nm contact depth. This is a strong indicator that the used area function are accurate. In Fig. 5.5b, the contact area in a range between zero and 1500 nm are compared, whereas the area of an ideal Berkovich indenter is set to one.

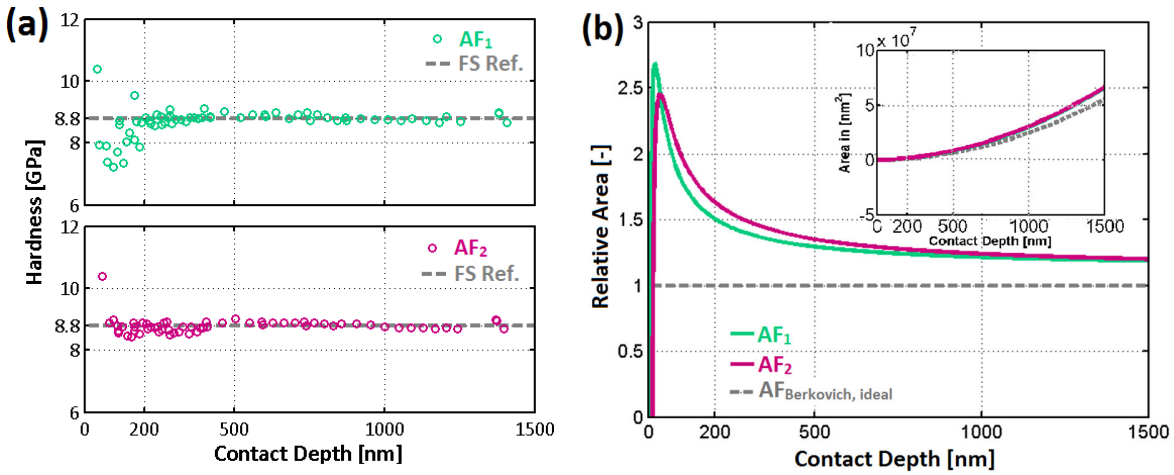

Fig. 5.5: Comparison of the area function determination results (a) and a comparison with and ideal Berkovich tip geometry (b).

It is obvious that both area functions own approximately 20 % more contact area at high depths. This is an indicator for a changed opening angle of the indenter tip, which might be related to a repair, conducted prior to the experiments. A simple error during the area function determination is neglected as cause, since the hardness numbers obtained with these area functions should then be suspiciously low, which is not the case. Moreover, it should be noted that AF_2 shows slightly enlarged contact areas, except for the very shallow depth regime. With increasing contact depth this difference in contact area, compared to AF_1, expires. This behavior is what would be expected for a minor wear of the tip, which seems plausible.

5.5 Pile-up and Sink-in Behavior

The potential influence of pile-ups or sink-ins to the results of nanoindentation measurements was discussed in chapter 2.4.8. AFM-mode measurements of indents made at room temperature for all materials indeed revealed a piling-up behavior which is shown in Fig. 5.6 from a 30° azimuth viewpoint. The lateral resolution was set to 0.2 µm and the scan size was selected to be 12 µm by 12 µm. Since the indenter tip is used as a probe in this method, the maximum depths to be reached are limited and dependent on the relative orientation of tip to indent.

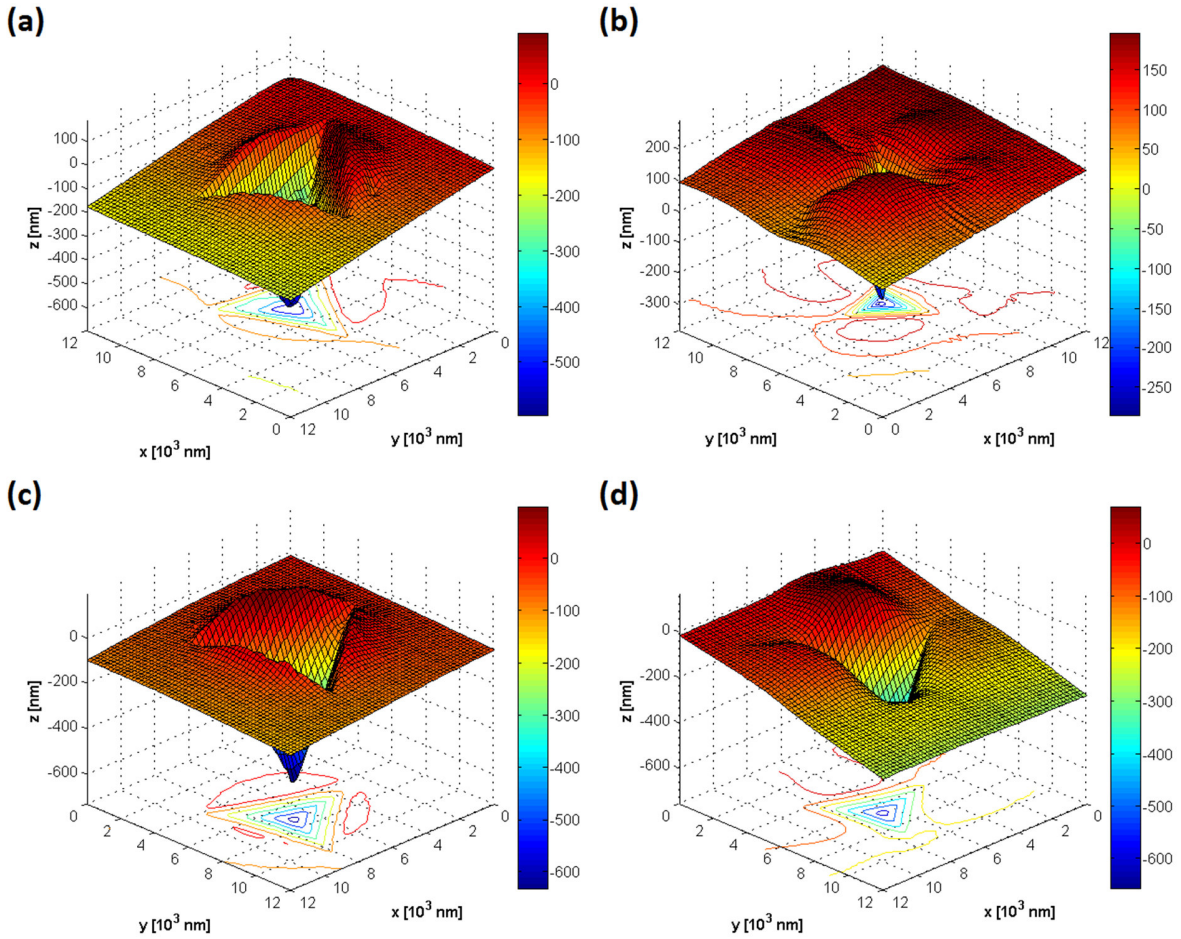

Fig. 5.6: AFM mode scans of ufg chromium (a), sx chromium (b), ufg tantalum (c) and sx tantalum (d).

The goal of this chapter is not to develop a correction approach for all indents made, but a mainly qualitative discussion about how the obtained pile-up behavior might influence the gained results. This is due to the fact that the quantitative correction of pile-ups is still a matter of ongoing debate [70]. Furthermore, all correction approaches known to the author, require post mortem AFM analysis [54] or at least reliable contact stiffness measurements [71]. Since the latter was in fact an issue especially at higher temperatures, these correction approaches are not applicable for the present data. On the other hand, the assessment of indents made on different materials and at different temperatures via AFM imaging would be extremely time-consuming. Besides that, Lee et al. [54] reported that the pile-up behavior might vary for different depths. The fact that the majority of indents to obtain hardness numbers were made with a cyclic loading scheme, limits the possibility of analyzing shallower imprints than the maximum depth by means of AFM. Hence a correction of different depths, which would be needed for the ISE fitting, is not possible. In summary, due to the mentioned constraints, a full correction approach seems not feasible, and only a qualitative discussion of possible influences is given below.

5.5.1 Influence of Pile-ups and Sink-ins

An attempt was made to at least show a trend of the pile-up and sink-in influence based on the indents plastic depths. Therefore, the plastic depth h_{pl} was obtained from load-displacement curves and used to calculate the plastic area with the according area function (blue lines in Fig. 5.7). This area is referred to as "ideal", since it does not take into account the possible presence of pile-ups or sink-ins. Subsequently, LIMI images of the indents were made and the plastic area measured with the free software ImageJ. Since the shape of the residual indents can be taken into account, the measured area is affected by pile-up and sink-in behavior (red and green lines in Fig. 5.7).

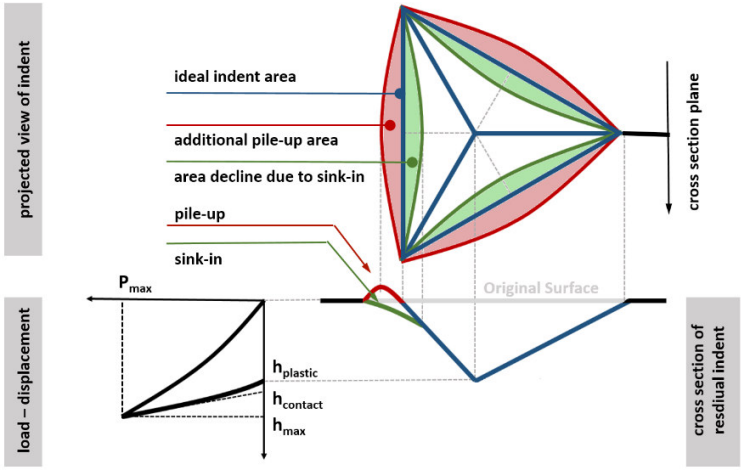

Fig. 5.7: Schematic illustration of ideal and pile-up/sink-in afflicted indent geometry.

In order to make an assumption about the pile-up influence for different materials at different temperatures, the ratio of the area gained by means of using the plastic indentation depth to plastic area measured by LIMI observations ("relative area") is plotted in Fig. 5.8. It is evident that all materials show a pile-up behavior at room temperature. This is consistent with the presented AFM images, see Fig. 5.6. Nevertheless, as it was already discussed in chapter 2.4.8, materials with a high strain hardening potential are more likely to exhibit sink-in than pile-up behavior. In fact, the pile-up behavior of the sx samples was quantitatively not as distinct as for the ufg samples (approximately 10 % compared to 20 % relative area), which is assumed to be indeed due to the different strain hardening potentials of sx and ufg materials. Moreover, according to Wang et al. [72] pile-up behavior of sx samples has been observed in the past. In their study they compare experimental with simulation results of copper sx and conclude, that the geometry of the primary slip dominates the piling-up, rather than a material translation due to strain hardening, as it is supposed in the classical point of view.

With increasing temperature, the relative area decreases for all materials, except for the 300 °C sx tantalum. It is furthermore interesting to note that relative area trends own a distinctive

knee for the first value above the critical temperature. Both sx curves even show an inverted trend of rising relative area at 300 °C. Bearing in mind the unexpectedly high macroscopic hardness of chromium sx at 300 °C compared to 200 °C, the different pile up-behavior might be a possible explanation. LIMI images of the indents of maximum and minimum relative area (marked by * and **) show a very distinctive shape difference, indicating pile-up and sink-in behavior, respectively. It needs to be noted that this comparison was made for load-profile 1 results. For the sake of representability, the sx tantalum image in Fig. 5.8 is from a load-profile 2 indent. However, the relative area values for both load profiles were very similar.

The data presented in Fig. 5.8, were used to discuss the influence of pile-ups at room temperature in chapter 5.6.1. Despite that, a correction at all temperatures based on the relative area discussed in this chapter does not seem fully justifiable, since the hardness numbers at different temperatures would close up in a physically not meaningful manner. Hence, the relative area numbers might be interpreted as a qualitative influencing trend of the pile-ups and sink-ins.

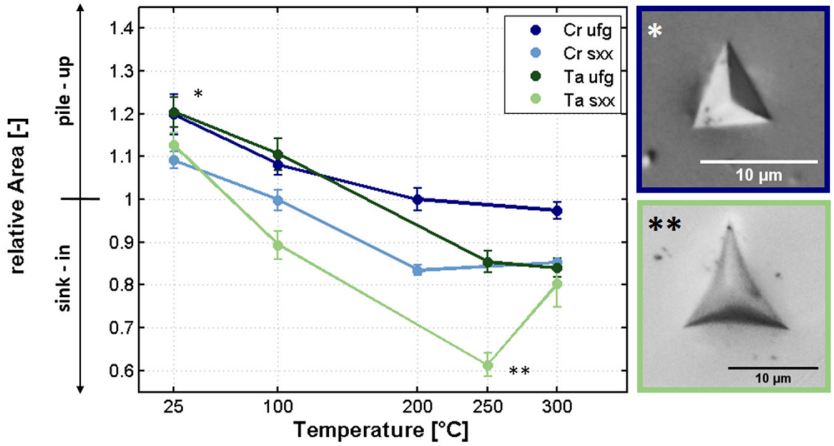

Fig. 5.8: Estimated influence of the pile-up and sink-in behavior for all materials at different temperatures.

5.5.2 Discussion on the Pile-up Appearance

The surfaces of the indents presented in Fig. 5.6 all exhibit a certain degree of tilting. These deviations from a perfectly perpendicular contact between the surface and the vertical axis of the indenter tip can be caused by preparation imperfections or the mounting of the sample on the holder. Sx tantalum (Fig. 5.6d) revealed the highest tilt angle of approximately 1.9 °, which is assumed to not considerably influence the results [73]. However, the formation of pile-ups seems to be favored on the side which is tilted in direction of the indenter tip, see Fig. 5.9a.

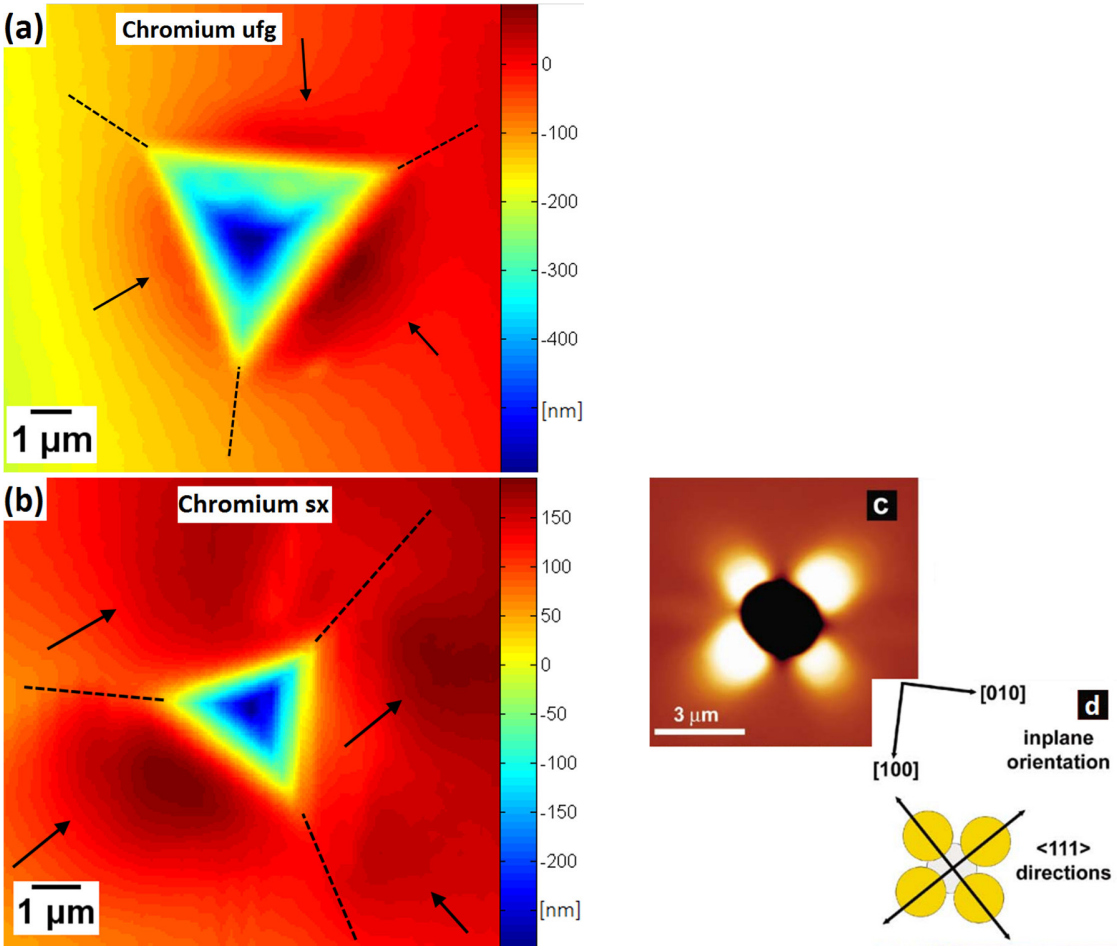

Fig. 5.9: Comparison of pile-up behavior of ufg (a) and sx chromium (b) for a Berkovich indenter. The arrows point on pile-ups, whereas the dashed lines symbolize constraint directions. Pile-up behavior of sx tantalum with a spherical tip [74] (c) and the assumed preferred slip direction [74] (d).

In terms of the pile-up shapes, two different behaviors were obtained. The ufg material piled up along the sides of the triangle shaped projection of the indent in an elliptical shape. Such a pile-up behavior was already described by [53]. Contradictory to that, it was found that sx materials show, due to their anisotropic properties, strongly orientation dependent pile-up behavior [72]. In order to reveal this dependency, it is common to use spherical indenters, rather than Berkovich, since the latter induces geometrical constraints to the pile-up. Nevertheless, it was shown by Kucharski and Jarzabek [75], that at higher loads even for a Berkovich tip the pile-up patterns get dominated by the crystallographic orientation. Since in their work no pile-ups in the direct vicinity of a bisecting line through an edge of the indents triangle were found, except for the (111) surface, these directions are referred to be constrained by the Berkovich indenter geometry. The mentioned findings were all observed on fcc copper. However, Biener et al. [74] report a two-fold geometry for a (001) tantalum sx using a spherical indenter, depicted in Fig. 5.9c. Comparing that AFM image with the chromium sx pile-up appearance in this work, shown in Fig. 5.9b, a strong similarity can be is evident.

Especially the fact that four hillocks are obtained around the indent for both sx, compared to only three on the ufg side, is a strong evidence for the anisotropic flow behavior of the chromium sx sample. Biener et al. [74] furthermore concluded that the dominating slip system was {110} ⟨111⟩. Since the experiments in this work were also carried out on a (100) plane and due to the similarity of the observed hillocks, it is concluded that the slip system leading to the observed pile-up pattern on sx samples might also be {110} ⟨111⟩.

5.6 Mechanical Properties

5.6.1 Hardness and Size Effect at Room Temperature

The following chapter is focused on discussing the reliability of the gained hardness numbers in the light of the ISE and possible error sources. Hence, comparisons are made with literature data and the results obtained from measurements on an Agilent G200 nanoindentation systems. Moreover, a pile-up correction for room temperature data, discussed in chapter 5.5.1, is included. An overview of the discussed hardness numbers can be found in Fig. 5.10.

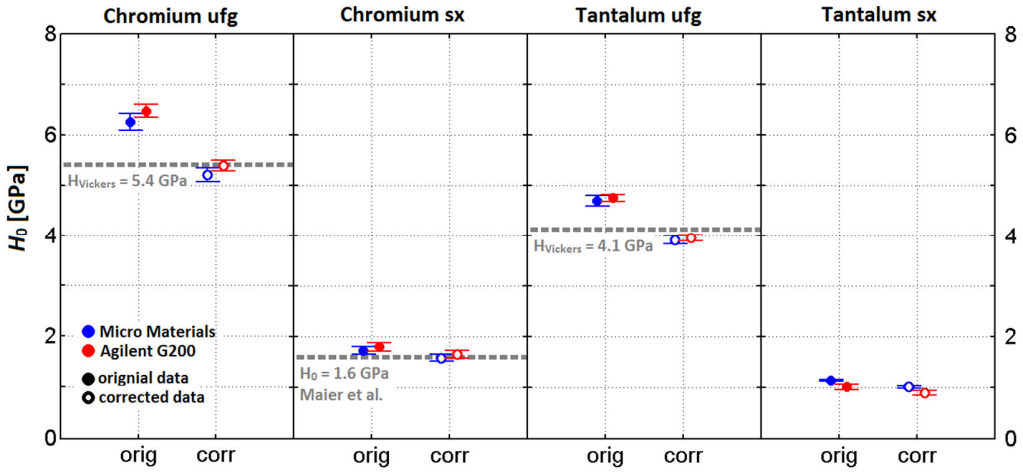

Fig. 5.10: Comparison of macroscopic hardness data gained by nanoindentation with microhardness results and available literature data [7]. Furthermore the figure is separated in original data ("orig") and pile-up corrected results ("corr").

Chromium: Ultrafine Grained State

In order to compare results from microhardness testing with those from nanoindentation, the later need to be analyzed for their size effect in order to provide the macroscopic hardness. This led to a H_0 of 6.25 GPa for ufg chromium which is approximately 16 % higher than the 5.4 GPa gained by microhardness testing for this material. The internal length scale h^* is crucial

for the accurate calculation of H_0 and was found to be only 35 nm. h^* is known do decrease with decreasing grain size and is therefore typically low for ufg materials. Maier et al. [7] found an h^* of 50 nm for an average grain size of 300 nm. Therefore the comparably low 32 nm are well reasonable due to the even lower grain size of 120 nm of the ufg chromium used in this work. Another possible source of error are an imprecise area function or general issues with the nanoindentation set-up. Therefore, comparison measurements were conducted on an Agilent G200 nanoindenter system. The results reveal a comparable H_0 of 6.47 GPa, giving a mismatch of less than 4 % and a h^* = 86 nm. However, it needs to be noticed that for the comparison measurements H_0 and h^* might be slightly overestimated, since a manual contact point finding for some load displacement data was required. The direct comparison of the gained hardness versus depth data is shown in Fig. A.1. In the light of these results, the mismatch between the numbers of microhardness tests and the nanoindentation data are assumed to merge from pile-up behavior of the chromium ufg material. For the same tip-geometry the pile-up behavior is supposed to be similar. Hence the gained hardness numbers of the two different nanoindentation systems should be well matching. This is the case, as discussed above. An in-depth discussion regarding pile-up behavior, including an estimation on the hardness falsifying influence can be found in chapter 5.5.1. The estimated correction factor, to take the pile-ups into account, was found to be 0.83 for ufg chromium at room temperature. Applying this correction leads to a macroscopic hardness mismatch of the original nanoindentation tests with the microhardness tests of less than 4 %. This very good agreement is shown in Fig. 5.10.

Chromium: Single Crystalline State

In general, the hardness numbers of the chromium single crystalline material showed less size effect than what would be expected by means of literature comparison. Maier et al. [7] report an h^* of 324 nm, which is essentially more than the 72 nm found in this work. In fact such low internal length scale numbers would be expected for a very fine grained material, as discussed for ufg chromium above. However, the macroscopic hardness of 1.73 GPa well matches the numbers found by the mentioned authors. Moreover, the H_0 values gained by comparison measurements, see Fig. A.2, are also very similar. An overview of these hardness numbers with and without a pile-up correction can be found in Fig. 5.10. The pile-up correction factor for chromium sx at room temperature was estimated to be 0.92. One might suspect two possible reasons for an unexpectedly low h^* but matching H_0 on the other hand: First, as discussed in chapter 5.4, the determination of the indenter tip area function can be challenging, especially in the shallower depth regime. However, hardness data beneath a contact depth of 200 nm were not used to determine the ISE, attempting to minimize the errors caused by an inaccurate area function at such low depths. Furthermore, if the area function would be the main cause of the low h^* numbers, results gained for the other materials should have unexpectedly low hardness levels at small depths as well. This would especially mean a hardness decrease towards lower contact depths in the case of the ufg materials, which was not observed. Hence, it is concluded that the area function is most likely not the principal cause of the low internal

length scale numbers found for sx chromium. Second, only hardness numbers received from load displacement curves containing a distinctive pop-in event were used. This feature is only present for sx or very coarse grained materials with low surface roughness [74]. This is indicating that no fine grains were present, which might have lowered the h^* numbers. Fine grains would have also increased the hardness significantly which is due to the well matching H_0 with literature very unlikely. The h^* provided by the mentioned nanoindentation comparison measurements is 161 nm in the case of using data above 100 nm, but 236 nm using also data points below. To the authors opinion, the very low internal length scale values gained from original nanoindentation data are caused by two major factors: On one hand as a result of too less reliable data in the low depth regime (≈ 100 nm), and a simple lack of data at the high depth regime (> 1000 nm). And on the other hand, effects which might have emerged from the comparably blunt tip used for the indentation experiments. The latter assumption might be supported by the findings of Swadener et al. [76], which report increasing hardness for spherical indenters with decreasing tip radius.

Chromium: Comparison of Ultrafine Grained and Single Crystalline State

As it was expected, the hpt processed ufg chromium has a significantly increased macroscopic hardness compared to its single crystalline counterpart. At room temperature they are divided by a factor of 3.6 which is a result of the Hall-Petch relation and the Taylor hardening in case of the ufg state [77]. Furthermore, the internal length scale numbers reveal higher values for the sx compared to the ufg microstructure, though the difference is due to the comparably low h^* of the sx not as high as expected.

Tantalum: Ultrafine Grained State

The ISE analysis provides a macroscopic hardness of 4.70 GPa, whereas h^* is 52 nm. These values are matching the 4.75 GPa and 36 nm observed by comparison measurements on the Agilent G200, presented in Fig. A.3. The low internal length scale values are, just as discussed for chromium above, expected for ufg materials. Compared to the 4.12 GPa Vickers microhardness, the H_0 numbers are approximately 15 % raised. A pile-up correction with an estimated correction factor of 0.83, leads to a H_0 of 3.92 GPa for the original nanoindentation data, which is in good agreement with the mentioned microhardness, as shown in Fig. 5.10.

Tantalum: Single Crystalline State

Indentation size effect parameters were found to be H_0 = 1.14 GPa and h^* = 273 nm. The corresponding control measurements delivered 1.02 GPa and 364 nm, respectively. As shown in Fig. A.4, the hardness versus depth curves obtained from the two different nanoindentation systems show comparable slopes at higher depths, but an more pronounced increase in hardness at shallower depths for the control measurements. However, the originally obtained h^* of 273 nm is in the range of what would be expect, see Fig. 5.12, which was not the case for

the very low h^* numbers of the chromium sx. Furthermore, the mismatch between the original and the comparison measurements is not severe, since the internal length scale is extremely sensitive to hardness and contact depth data.

Tantalum: Comparison of Ultrafine Grained and Single Crystalline State

The macroscopic hardness numbers of ufg and sx tantalum are separated by a factor of 4.1. Different to the results of the chromium, the internal length scale numbers of the ufg and the sx state are well apart, being 221 nm higher for the sx.

5.6.2 Hardness and Size Effect at Elevated Temperatures

Chromium

The ufg and the sx samples own their highest hardness numbers at room temperature, as shown in Fig. 4.13. When increasing the temperature, the hardness starts to decrease as well, but in different magnitudes for the different microstructural constitutions. The absolute hardness decrease is always higher in the case of the ufg material compared to the sx. This leads to a declining absolute hardness difference $H_{0,ufg} - H_{0,sx}$ between the two microstructural constitutions at elevated temperatures, which is shown in Fig. 5.11a. The reason for the decreasing hardness is in case of the sx constitutions is the rapidly shrinking contribution of the Peierls stress to the thermal flow stress at elevated temperatures. In case of the ufg material, besides the mentioned contribution from the Peierls stress, further contributors to the thermally activatable part of the flow stress are assumed to play a significant role. Though, the maximum experimental temperature is only 0.26 T/T_m in terms of chromium, it is known that for materials with a high grain size density, grain boundaries might be a major contributor to overall plasticity, even at low homologous temperatures [78, 79]. It is interesting to note that, although the absolute hardness difference $H_{0,ufg} - H_{0,sx}$ between sx and ufg state is decreasing, the ratio between them $H_{0,ufg} / H_{0,sx}$ is increasing up to 200 °C, followed by a drop at 300 °C, see Fig. 5.11a and b. The drop is a result of the expiring influence of the Peierls stress, causing the sx hardness to not decrease further when elevating the temperature. However, the slight hardness increase of the sx sample at 300 °C, compared to the 200 °C measurements is physically not meaningful. Since chromium is known for its excellent oxidation resistant properties [67], hardening in a similar way as it is expected for the tantalum is very unlikely. Therefore experimental flaws, are assumed to have led to the slight overestimation of the hardness at 300 °C.

Tantalum

It was evident from experimental findings that tantalum ufg and sx samples started to harden at temperatures of 250 and 300 °C in a significant way. A meaningful analysis regarding the ISE and macroscopic hardness was hence rendered impossible. Thus, in the following chapter only

a discussion on the numbers gained at 100 °C is given, where no hardening occurred. In a following subchapter the hardening behavior is described, whereas in chapter chapter 5.7 an in depth discussion is given about the possible reasons of the observed hardening phenomenon. The hardness trends of the ufg and sx tantalum up to 100 °C were found to be very similar to those of chromium described above. While the absolute hardness decrease at elevated temperatures of ufg tantalum exceeds that of its sx counterpart, the relative hardness decrease behaves inverse, as depicted in Fig. 5.11a and b. It is worth noting that the absolute hardness difference between the two states is nearly the same at room temperature and 100 °C. This might lead to the assumption that grain boundary associated processes in the ufg state do not play a significant role at the mentioned temperatures.

Comparison of Chromium and Tantalum in Different Microstructural States

The macroscopic hardness decrease of all materials normalized by their room temperature numbers is depicted in Fig. 5.11c. In terms of the ufg materials, the tantalums normalized hardness loss at 100 °C is less than that of the chromium. This seems meaningful, since grain boundary mechanisms contributing to plastic deformation are assumed to be less distinct at 0.11 in terms tantalum compared to 0.17 T/T_m in terms of chromium. Opposite to that, the sx tantalums normalized hardness loss is higher compared to its chromium counterpart. If similar critical temperature and thermal flow stress are assumed for both sx, its diminishing towards higher temperatures would lead to a higher normalized hardness drop in the tantalum, due to its lower overall flow stress. However, this is only a possible explanation for the observed trend for the sx constitutions.

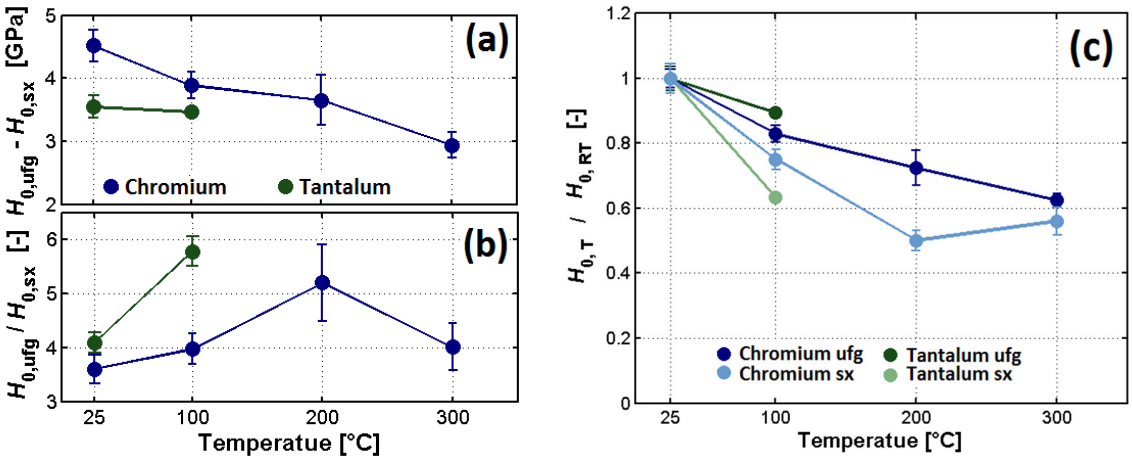

Fig. 5.11: Comparison of the macroscopic hardness values of ultrafine grained materials with the corresponding single crystals for chromium and tantalum.

Temperature Dependence of the Indentation Size Effects Internal Length Scale

To the best knowledge of the author, there is no solely accepted explanation about the influence of temperature changes on h^*. Rather different results and interpretations coexist for single crystalline samples, whereas results from polycrystalline samples are completely lacking. For fcc copper Franke et al. [80] found a decreasing h^* with increasing temperature. So did Lee et al. [81] for aluminum and gold between 160 and 298 K, though the trend for the latter one was not really distinctive. They further found an increasing h^* for bcc niobium, but a decreasing trend for bcc tungsten. Maier et al. [17] measured an increasing h^* with raising homologous temperature via room temperature experiments on bcc materials with different T_c. The latter findings are furthermore supported by microcompression tests conducted by Schneider et al. [59], reporting a matching trend regarding the power law exponent. An overview of the mentioned nanoindentation data regarding h^* for bcc materials is given in Fig. 5.12, including results from this work. In order to calculate homologous temperatures for the data of Lee et al. [81], critical temperatures of niobium and tungsten were set to 350 and 800 K [59], respectively.

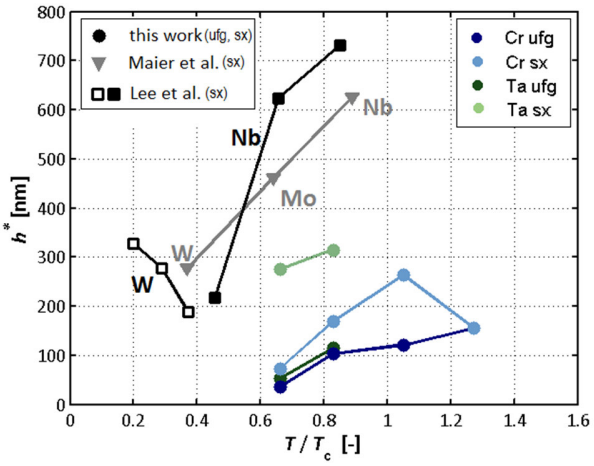

Fig. 5.12: Literature comparison of different temperature dependences of h* for sx bcc metals including the sx and ufg results of the present work [17, 81].

The assumed underestimation of h^* regarding the sx chromium investigated in this work is evident again. Despite that, the sx tantalum numbers are in a range of what would be expected. It needs to be pointed out that this comparison is not able to predict h^* at certain temperatures, nor at which exact rate they change with temperature. Nonetheless, most available data suggest an increase of h^* with temperature, at least up to T_c, in agreement with the data obtained in this work. As mentioned, for polycrystalline materials and temperatures above T_c no published data are known to the author. The decreasing h^* for chromium sx above T_c is, however, an interesting feature. Though no in detail investigation were carried out, an observation based suggestion is made here: Due to the expired influence of the Peierls stress above T_c, bcc sx are known to behave similar to their fcc counterparts, which were reported to

show a decreasing h^* trend with increasing temperature [80]. Therefore it is suggested that bcc sx metals have a bcc-type h^* regime with increasing values below Tc and an fcc-type h^* regime with decreasing values above T_c.

Hardening Behavior of Ultrafine Grained and Single Crystalline Tantalum

In this part of the discussion the general hardening behavior of the tantalum samples is discussed. This is of major importance, since it needs to be derived at which temperature the hardening phenomenon started, not only in order to prove credibility for the numbers gained at lower temperatures, but also to allow for a sophisticated investigation of the underlying principle. In order to give a good overview, the hardening behavior is presented for different materials and temperatures separately, as shown in Fig. 5.13. This gives the opportunity to show the difference between preheating room temperature, high temperature, and post high temperature results, as hardness versus contact depth without cluttering the figures.

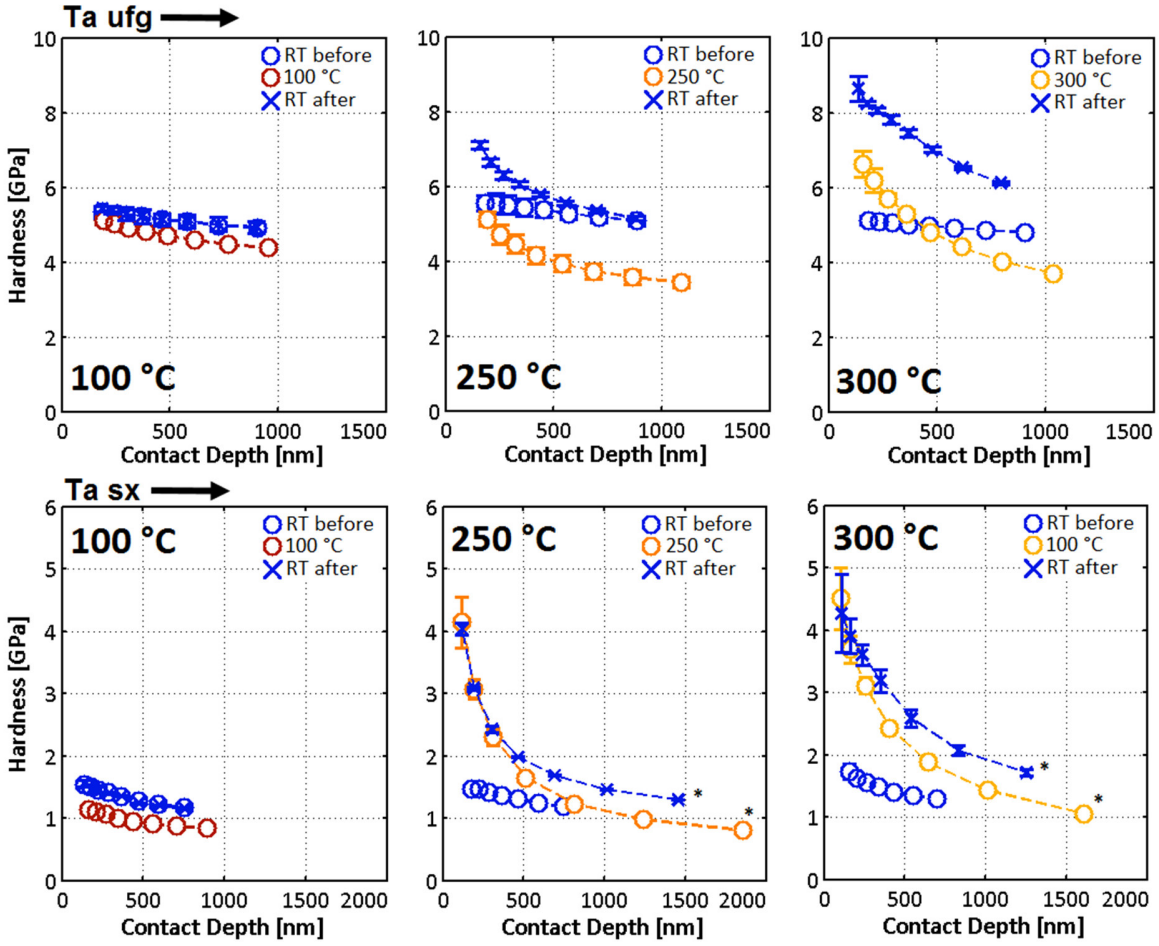

Fig. 5.13: Hardening behavior of tantalum ufg (first row) and sx (second row) at 100, 250 and 300 °C. Curves marked with a star were observed with load profile LP2, whereas for all other curves the according LP1 was used.

From the presented figures it is evident that neither for the ufg nor for the sx state hardening occurred at 100 °C. This is clearly demonstrated by identical curves observed for pre and post heating experiments. From 250 °C on very distinctive hardening is observed for both microstructural constitutions, which is even more increased at 300 °C. When comparing hardness gains between ufg and sx materials, it needs to be considered that the lowest contact depths of the ufg are higher than those of the sx results. Regarding the contact depth it needs to be mentioned that, though no lower limit was set, the first load cycles of the 250 and 300 °C sx curves were not used, since they were in the fully elastic regime. Finally, it is very interesting to note that, though the hardness gap between high temperature and post high temperature measurements is very pronounced, those for the sx material are very similar for 250 and 300°C.

5.6.3 Young's Modulus

Room Temperature

The measurement of the Young's modulus turned out to be a challenging task, especially at elevated temperatures. The room temperature Young's modulus numbers for the ufg materials stayed, as expected, constant with respect to indentation depth as it is depicted in Fig. 4.9b and Fig. 4.11b for chromium and tantalum, respectively. The chromium ufg average number of 320 ± 10 GPa is approximately 9 % higher compared to literature data [18]. Whereas tantalum ufg reveals 198 ± 6 GPa, which is an elevation of 6 % compared to [52]. Due to the low mismatch with literature numbers, the ufg room temperature results seem plausible.

The sx Young's moduli of chromium and tantalum, both exhibit low values at low indentation depths. This behavior is shown in Fig. 4.10b and Fig. 4.12b and leads to lower averaged Young's moduli compared to their ufg counterparts. However, they are with 312 ± 26 GPa for chromium and 189 ± 15 GPa for tantalum still well in the range of what would be expected. An overview of averaged numbers can be found in Fig. 5.14.

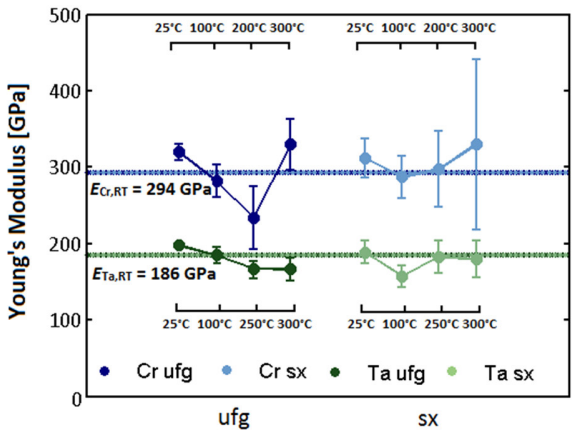

Fig. 5.14: Overview of the averaged Young's moduli at different temperatures for all materials.

Elevated Temperatures

The decrease of the Young's moduli at temperature up to 300 °C is expected to be negligible, as it is shown in Fig. 2.3. In fact some tests at elevated temperatures showed a noticeable decrease, some even experience an increase compared to the room temperature measurements (see Fig. 5.14). In the case of a notable decrease, it was evident that the Young's moduli at low indentation depths were comparable to those measured at room temperature. However, at elevated depths, the numbers start to decline. This behavior was not observed for the experiments conducted at ambient temperature before heating, but for those made after high temperature tests. Machine stiffness issues at high temperature would only affect the experiments at elevated temperature, but not those made subsequently at room temperature. Hence, this possible origin is neglected. Moreover, a possible thermal drift is not expected to be high enough to cause such a behavior. Thus, it is suggested that the use of high-temperature cement to mount the sample, described in chapter 3.7.2, for the elevated temperature experiments is the primary origin of the unexpected depth-dependence of the Young's moduli for some experiments. The suspicion is that the cement cracks at elevated temperatures and thus the contact stiffness, which is used to determine the Young's moduli, drops. At higher depths and hence higher loads, the influence of this effect is most pronounced and leads to an underestimation of the samples Young's modulus. To underline this estimation, reliable comparison measurements, carried out on an Agilent G200 nanoindenter, were used to theoretically approach this issue. Therefore the obtained Young's moduli data were altered by the addition of 0.3 nm / mN compliance which is equivalent to a lowered stiffness. The influence on the Young's moduli, as well as on the hardness is shown in Fig. 5.15.

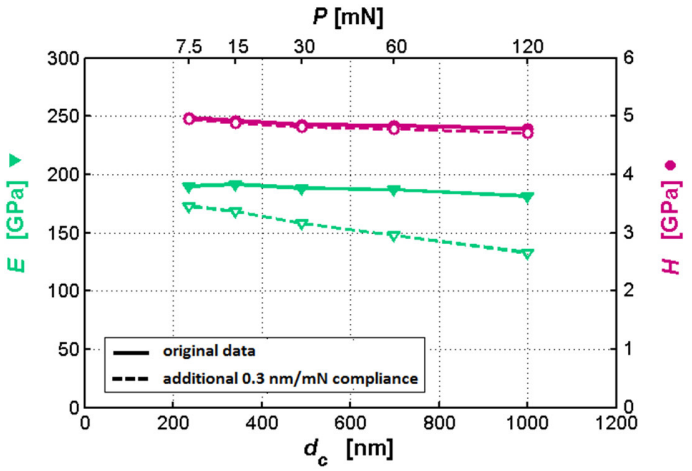

Fig. 5.15: Young's modulus and hardness of Ta ufg as measured at room temperature and with artificial compliance added.

It is evident that the change regarding the Young's modulus is severe and comparable to the shapes obtained in some high temperature nanoindentation experiments. Despite that, the hardness numbers do show only a very slight dependence on the altered compliance. Hence,

it is concluded that the depth dependence of some Young's moduli presented in chapter 4.4.1 are caused by the mentioned stiffness issues of the cement. It is further assumed, based on the above observation, that the hardness numbers are thereby not falsified in a significant manner.

Finally, it is interesting to note that the standard deviation of the chromium samples, both sx and ufg, were systematically higher than those observed for the tantalum samples. It is suspected that the higher the materials Young's modulus and analogous its stiffness, the more sensitive they react to the mounting issues described above.

5.6.4 Rate Dependent Properties

Procedure

The general approach of presenting the SRS and V^* results as a function of stress for the entire creep curve and next to it the analysis of stage A, was chosen for the following reasons: On one hand the usage of the entire creep curve shows the dependency of the SRS on the strain rate and hence stress it was obtained at. On the other hand, the complete creep curve is expected to be more susceptible for the influence of thermal drift and fitting issues, compared to the 20 s stage A analysis. In the following chapters, discussing the rate dependent properties, the results of both approaches are compared and discussed under the consideration of findings presented in literature.

General Discussion on Recent Findings

It is very well known that for sx and cg bcc materials the thermally activated nucleation of double kinks in screw dislocation dominates the deformation behavior [82]. In a recent work Maier et al. [7] investigated the SRS of ufg (≈ 300 nm) and sx chromium by conducting strain rate jump-tests. There findings (see Fig. 5.16) were a substantially higher SRS for the sx compared to the ufg state, which is an already well established finding for bcc materials [21, 23]. Moreover, a decreasing SRS with increasing temperature for sx, explained by the diminishing thermal component of the flow stress was found. Additionally, they report for the ufg state a slight decrease from RT to 100 °, but a subsequent increase at 300 °C. This trend was explained by the conclusion that in case of an ufg constitution the thermally activated component of the flow stress consists of the Peierls stress and contributions from grain boundary dislocation interactions. Whereas the influence of the Peierls stress decreases with temperature and eventually diminishes at T_c, the contribution of grain boundary dislocations is increasing.

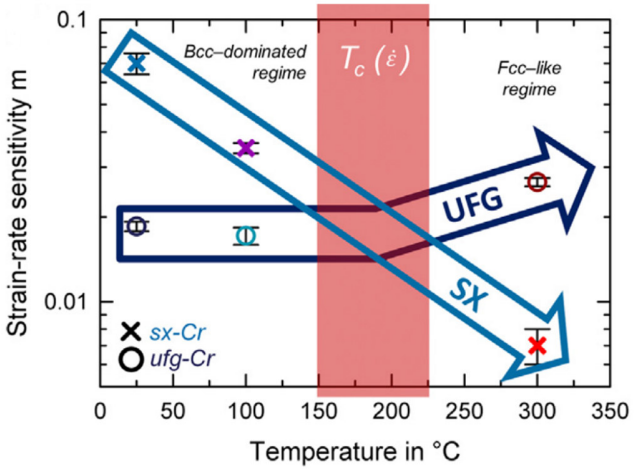

Fig. 5.16: SRS of ufg and sx chromium as a function of temperature [7].

Keeping in mind the importance of screw dislocations and the associated kink pair mechanism not only for the SRS of bcc sx or cg materials, but also for the lower SRS of bcc ufg materials, the findings of Cheng et al. [83] are highly interesting. They found a diminishing density of screw dislocations, but an increasing density of edge and mixed dislocations beneath a certain grain size as depicted in Fig. 5.17. It is concluded by them that the low SRS of bcc nc materials is primarily caused by the dominance of edge and mixed dislocation. Though their results were reported only for molybdenum, it might be concluded that the ufg materials investigated in this work (≈ 100 nm) are situated in the transition region.

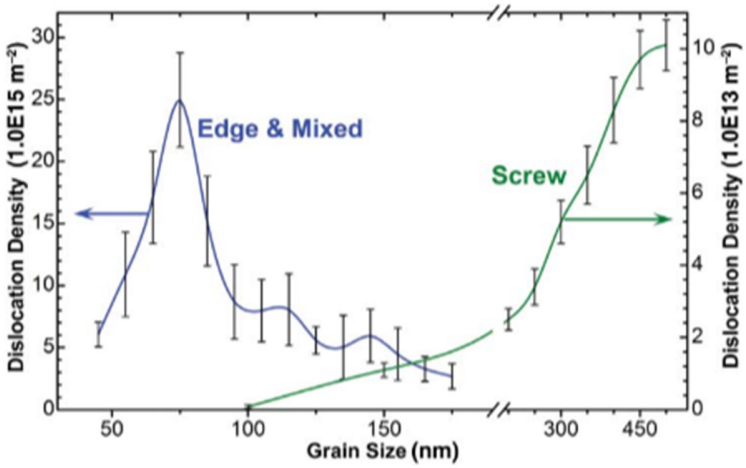

Fig. 5.17: Variation of dislocation density and type as a function of grain size obtained HPT processed molybdenum [83].

Room Temperature

Both ufg materials were found to have a factor four to five lowered SRS compared to their sx counterparts. Except for grain sizes in the range of 10 nm, the decreasing SRS with decreasing grain size for bcc metals is a generally accepted observation [21, 23]. Moreover, the results gained at ambient temperature are not only well comparable to comparison measurements on the same samples, but also with available literature, as shown in Table 13. For slightly differing numbers of the SRS range for the full creep curve compared to the stage A analysis, the different fit ranges in terms of time are accounted for.

Table 13: Overview of room temperature SRS values obtained from creep curve analysis, strain rate jump-test comparison measurements, and available literature data.

SRS [-]	full creep curve	stage A	SRJ Agilent G200	literature findings (grain size in nm)
ufg chromium	0.007 – 0.016	0.011	0.015	0.02 (300) [7]
ufg tantalum	0.005 – 0.010	0.013	0.013	0.007 (150) [23]
sx chromium	0.024 – 0.055	0.053	0.054	0.07 (sx) [7]
sx tantalum	0.022 – 0.055	0.044	0.045	0.046 (cg) [23]

The physical explanation for the observed trends is assumed to be the following: The SRS of sx is high due to a high share of the thermally activatable flow to the overall flow stress. Contrary to that, the share of thermal flow stress for ufg is lower, since the athermal stress component is significantly raised by grain boundary strengthening [84]. However, another possible source of the low SRS at room temperature of nc bcc metals might be the influence of an increasing edge and mixed dislocation density, as discussed above, which would increase the dislocation mobility.

The activation volume V^* is often used as an indicator for the predominant deformation mechanism. Hence very similar activation volumes can be assumed independent of grain size if the deformation mechanisms are the same [84]. This is in fact what was observed at room in this work, as presented in Table 14. The monotonous slightly higher numbers obtained by the stage A analysis, compared to the strain rate jump tests, are expected to be caused by higher hardness numbers observed due to the nature of the latter procedure.

Table 14: Overview of room temperature V^* values obtained from creep curve analysis, strain rate jump-test comparison measurements, and available literature data.

V^* [b^3]	full creep curve	stage A	SRJ Agilent G200	literature findings (grain size in nm)
ufg chromium	14 – 33	21	13	14 (57) [21]
ufg tantalum	2 – 21	16	13	12 (150) [23]
sx chromium	16 – 31	14	11	18 (cg) [21]
sx tantalum	16 – 35	18	14	-

Remarks on the Discussion of Elevated Temperature Results

Since the general behavior of ufg samples was similar to each other, but different to their sx counterparts, the discussion on the high temperature trends will be separated by means of microstructural constitutions. Since the SRS is expected to have a strong dependence on the homologous testing temperature T/T_c, this relation is added as a second scale on the top of the graphs presented in the following. This is only possible since the latest findings known to the author reveal a very similar T_c for chromium and tantalum of approximately 450 K [7, 59]. Finally it should be mentioned that the SRS and V^* numbers discussed for room temperature are incorporated in the elevated temperature graphs for reference.

Elevated Temperature: Ultrafine Grained States

The SRS and V^* ufg states of chromium and tantalum depict a comparable dependency on temperature, as shown in Fig. 5.18. For both the SRS is in the range of 0.01 at room temperature and steadily increases up to approximately 0.06 and 0.10 regarding stage A at 300 °C for chromium and tantalum respectively. At high dwell times, the analysis of the complete creep curve proposes an even higher SRS. This regime of the creep curve, however, is assumed to be very susceptible for thermal drift influences [42]. Despite that, even the stage A SRS seems to be high, compared to the approximately 0.03 at 300 °C reported for chromium ufg by Maier et al. [7]. They also report a constant SRS of 0.02 at ambient temperature and 100 °C respectively. The main difference between the chromium ufg microstructures of this and the mentioned work is the grain size, which are 100 and 300 nm respectively. This might lead to the assumption that for the ufg chromium investigated in this work, the contribution of grain boundary-dislocation interactions might become already dominant at temperatures beneath T_c, which would explain the continuous increase of the SRS with temperature. In general the ufg tantalum is assumed to behave in a similar way as the ufg chromium. Nevertheless, it needs to be mentioned again, that at 250 and 300 °C the tantalum showed a distinctive hardening which influenced the SRS as well. The according curves are marked with a star in the presented graphs. Despite the mentioned assumptions to explain the higher numbers obtained in this work, it cannot be precluded that thermal drift at elevated temperatures had significant influence on it. A further discussion on that is given in a following subchapter.

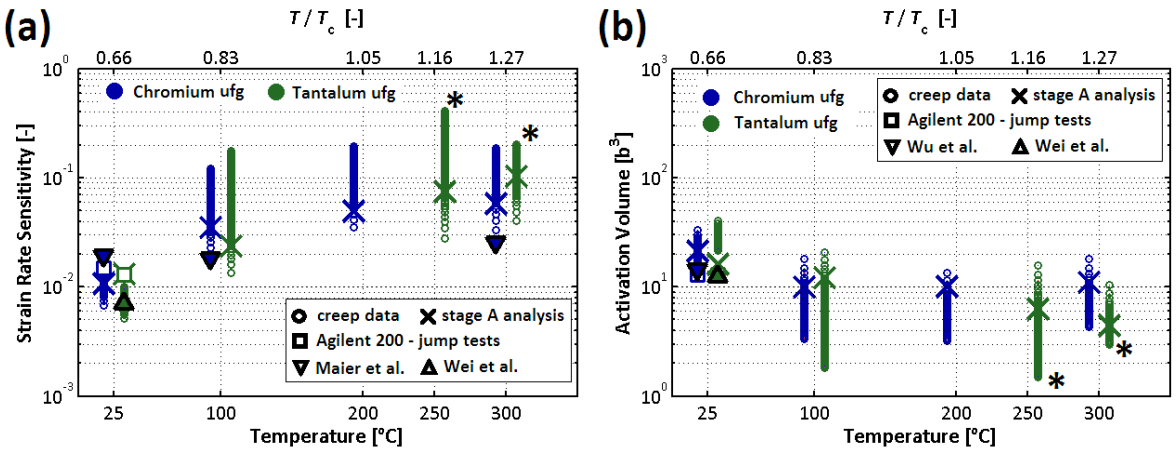

Fig. 5.18: SRS (a) and V^* (b) of ufg chromium and tantalum. Data presented are obtained from creep experiments, Agilent G200 strain rate jump-tests and available literature [7, 21, 23]. Tantalum numbers assumed to be influenced by hardening are marked with a star. For presentational reasons, chromium is offset to the left of the temperature indicating line, tantalum to the right.

The activation volumes, which are assumed to give hints on the governing deformation processes are, except for the hardening influenced tantalum curves, only slightly decreasing from room to elevated temperatures. This might be interpreted as a sign of a consistent deformation process.

Elevated Temperature: Single Crystalline States

Both single crystals, chromium and tantalum are expected to behave in a very similar way, since there is no influence of grain boundaries, and the homologous temperatures are well comparable. The experiments indeed showed a good agreement between those, which is shown in Fig. 5.19. The general temperature dependence of the SRS might be described as follows. From room temperature to 100 °C a noticeable drop was obtained, from there on the SRS is increasing again. The already mentioned work of Maier et al. also investigated the SRS of sx chromium at a similar temperature range. They found a continuous SRS decrease with increasing temperature. They linked that with the decreasing thermal flow stress towards T_c, leading to a diminishing hardness difference for various strain rates. This conclusion is reasonable, since for single crystals no further contributions from grain boundaries are expected. Keeping the different measuring methods in mind, the numbers up to 100 °C gained in this work seem very reasonable. However, the increase of the SRS from 100 to 300 °C is unexpected and is assumed to be the result of drift influence, rather than an intrinsic material property. This is further discussed in a following subchapter.

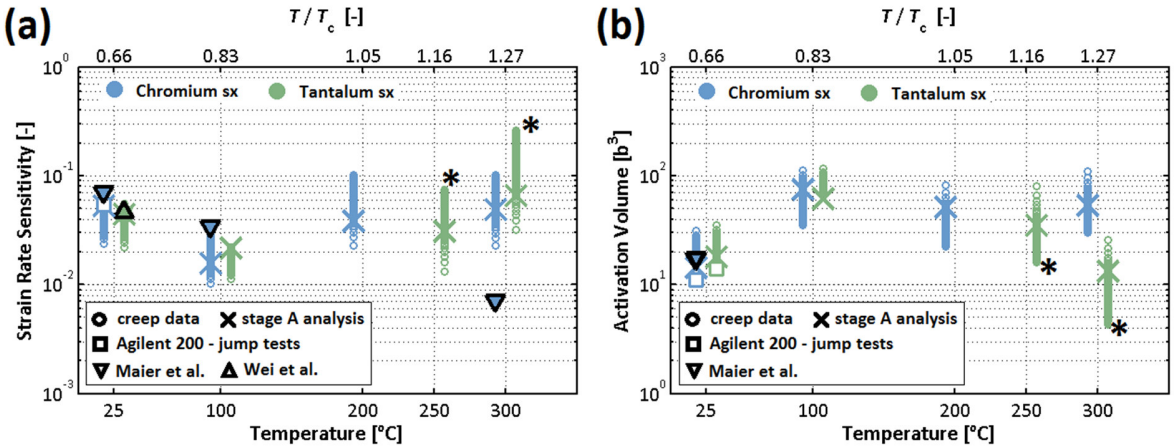

Fig. 5.19: SRS (a) and V^* (b) of sx chromium and tantalum. Data presented are obtained from creep experiments, Agilent G200 strain rate jump-tests and available literature. Tantalum numbers assumed to be influenced by hardening are marked with a star. For presentational reasons, chromium is offset to the left of the temperature indicating line, tantalum to the right.

For the activation volume, no comparable elevated temperature numbers are known to the author. Despite that, some conclusions might be made based on the known change of SRS and hardness at elevated temperatures, as proposed by Eq.(9). Since hardness and SRS for bcc sx are expected to decrease significantly towards T_c, V^* is assumed to continuously increase. This expected trend matches the results up to the results at 100 °C. The numbers at 200, 250 and 300 °C are influenced by the assumed overestimation of SRS in this temperature regime and hardening in the case of tantalum, as discussed above.

Remarks on the Possible Influence of Thermal Drift

Thermal drift is expected to have influenced the relaxation experiments and thus the rate dependent properties at temperatures above 100 °C. This is especially evident since the SRS of sx chromium is expected to continuously decrease with increasing temperature, which was not found at high temperatures in this work. The following discussion is based on the idea to access the drift rate required to bring the SRS of chromium sx at 300 °C in the range of the reported 0.01 [7]. Therefore, an artificial drift of varying amount was added to the originally obtained displacement data. A positive artificial drift is related to higher creep rates and vice versa. It needs to be mentioned that the original data was already corrected by the nanoindentation systems drift correction. Hence, curves signed with 0.0 nm /s artificial drift were already corrected for a certain amount of thermal drift by the system.

The results of adding different drift rates to the sx chromium creep curve at 300 °C are presented as Norton and SRS versus stress plots in Fig. 5.20. For comparison reasons, the results from measurements at room temperature and 100 °C are incorporated in the figures as well. It can be clearly seen that a positive artificial drift leads to even higher SRS and is hence not plausible. Adding negative drift on the other hand delivers a trend pointing in the direction

of lower SRS numbers expected. For -0.3 nm/s added drift, a SRS in the range reported by Maier et al. can be found [7]. The correction applied by the nanoindentation system for this 300 °C creep curve was 0.05 nm/s. Based on these results, it is concluded that the creep curve of sx chromium was strongly influenced by thermal drift. A further conclusion is that the nanoindentation system was not capable of correcting the assumed thermal drift based on a single point drift determination. In general this type of drift measurement and correction was recently reported to be inaccurate in many cases [85].

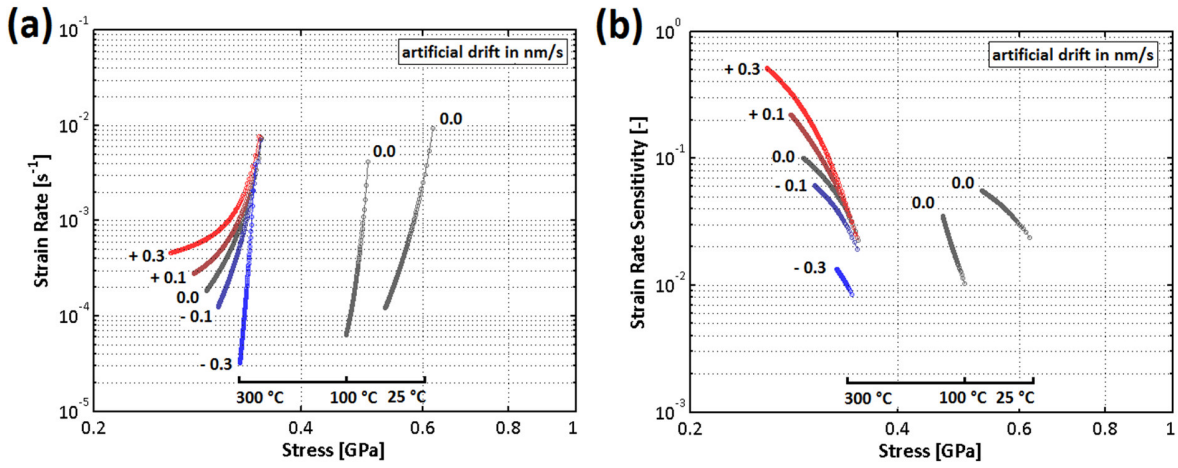

Fig. 5.20: Sx Chromium, an overview of the influence of artificial drift on Norton plots (a) and the final SRS (b).

Since measurements for sx and ufg materials were conducted with the same settings, the possible influence of thermal drift is also investigated for the latter. Again, to avoid any influence from hardening occurred on the tantalum sample, the chromium sample was chosen for this discussion again. It is evident that the SRS is again decreasing by adding negative drift. Furthermore, it is apparent that -0.3 nm/s artificial drift leads to an even lower SRS than what was observed at 100 °C. This might be interpreted as a sign of overcorrection of the 300 °C curve, or as an indicator for the significant influence of drift even at 100 °C. Moreover, it is very interesting to note, that the highest negative artificial drift applied again resulted in SRSs well comparable to those obtained by Maier et al. [7]. The thermal correction applied by the nanoindenter system was 0.23 nm/s, again directing the SRS towards unexpected higher numbers.

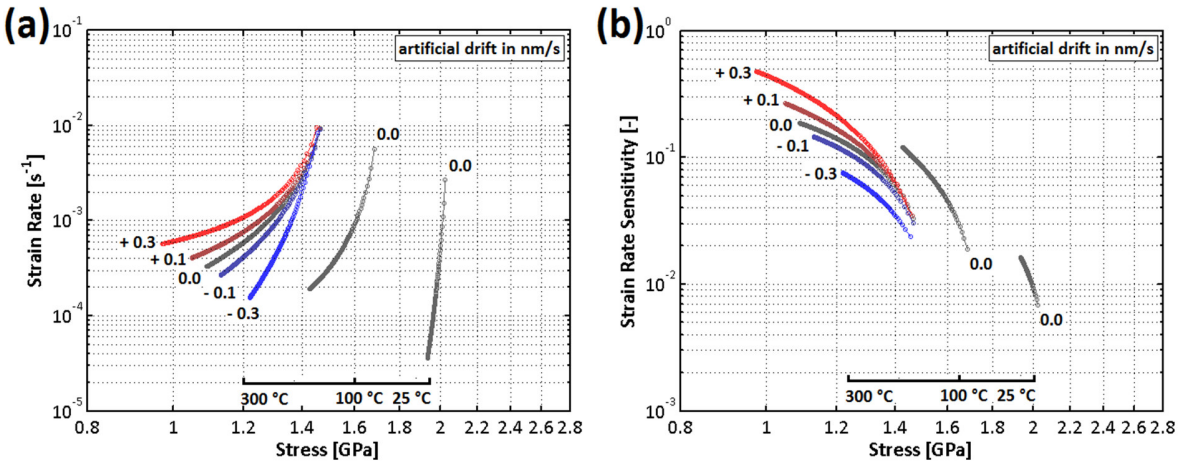

Fig. 5.21: Ufg Chromium, an overview of the influence of artificial drift on Norton plots (a) and the final SRS (b).

Influence of Tantalum Hardening on Rate Dependent Properties

At temperatures of 250 °C and 300 °C experiments revealed a hardening for the tantalum samples, which reduces with increasing depth. Creep experiments at the mentioned temperatures are hence influenced by this unexpected effect. It was found that the flow stress of the creeping process was significantly raised. This is except for the 250 °C ufg, where no increase in the flow stress was found at the 850 nm depth the creep test starts. It is concluded that the flow stress decrease outpaces the hardening at this temperature and depth, which is in good agreement with hardness versus depth numbers presented in chapter 4.4.1.

In order to investigate the influence of the hardening on SRS and V^*, in Fig. 5.22 creep results at room temperature are presented alongside with results from high temperature measurements. The room temperature measurements were obtained on the dedicated room temperature sample, which was not used for high temperature experiments, and on the 300 °C sample after the high temperature runs. The latter were made with the standard maximum load for these tests of 20 mN and with an increased load of 80 mN, respectively.

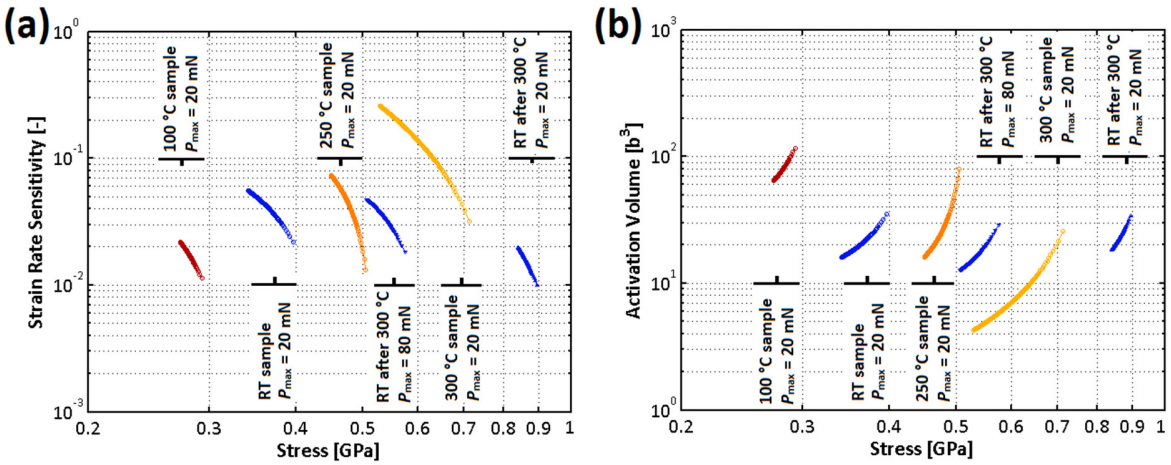

Fig. 5.22: Comparison of sx tantalum SRS (a) and V^* results (b) containing hardening affected (RT after high temperature, 250 °C and 300 °C) an non-affected data (RT, 100 °C).

It is evident that the flow stress is dramatically increased in the case of the 250 °C and even more for the 300 °C. It is furthermore coherent that the room temperature results on the 300 °C sample, gained after the high temperature experiments, are higher than those observed at 300 °C. The use of a higher maximum load of 80 mN leads to a higher indentation depth. The resulting flow stress is situated in between the dedicated room temperature findings and those made with the 20 mN load profile. This indicates a flow stress decrease with increasing indentation depth, as it was already found in previous chapters. From the available results it is assumed that the SRS might only be influenced by the hardening effect through the shift to higher stress numbers. This leads to a slight decrease of the SRS as it is depicted for room temperature findings in the figure above. V^* values kept approximately constant, since the hardness increase and the SRS decrease compensate each other. However, at high temperatures it is expected that the dramatic increase in hardness led to a shrinking V^*.

5.6.5 Incipient Plasticity

Chromium: Single Crystalline State

It is obvious, see Fig. 4.22a, that the overall spreading of the pop-in loads is most pronounced for the room temperature numbers. This might be due to the fact that the room temperature curve contains of pop-ins of all samples prior to heating. The curves, demonstrating the loads at which the pop-in event was observed, show a distinctive shift to lower loads with increasing temperature, indicating lower stresses at the pop-in events.

Fig. 4.22b shows that pop-in excursion and load do have a strong, close to linear relation as proposed by [86]. Moreover, it is noticeable that the slope, which is basically the ratio between pop-in excursions to pop-in loads, is increasing with temperature. This has already been reported by [87] for sx tantalum and was attributed to the decreasing friction stress.

The average room temperature shear stress at pop-in was found to be 11.7 GPa, which is somewhat lower than the approximately 15 GPa for cg chromium found by Wu et al. [88]. However, Shim et al. [49] reported that the tip radius might have a strong influence on the pop-in load and strength. A recent work of a similar kind for cg chromium is by Wu et al. [50]. It is therein suggested that with increasing tip radius the strength might decrease due to a higher probability of activating preexisting dislocations. The mentioned 15 GPa [66] for cg chromium were measured with a 210 nm radius bercovich indenter. The experiments of the present work, however, were conducted with an bercovich indenter as well, but with a significantly higher tip radius of approximately 450 nm. Since a higher tip radius leads to higher volumes affected by its stress field, the probability of an vacancy or an inpurity enabling heterogenous dislocation nucleation [88] or even the activation of an preexisting dislocation might be distinctivly increased. Hence, the above described mismatch of shear strenghts seems reasonable when taking the different tip radii into account. This suggestion is further supported by the fact, that though the average shear strength might be decreased in the case of a higher tip radius, the maximum values should be somehow matching. The maximum shear stress found at room temperature in this work is close to 16.5 GPa, whereas Wu et al [88] found approximately 17 GPa, which is in fact a good agreement.

The shear strength of the tested sx chromium is decreasing with respect to temperature, which has been widely reported for this and other materials in the past [88, 89]. However, the strength drop of 10 % at 100 °C compared to room temperature might be an overestimation, since [88] report a drop of close to 5 % at 150 °C. The critical shear strength at 200 °C was measured to be 20 %, the 300 °C tests revealed even 36 % lower numbers than the according room temperature measurement. However, the indents made on the high temperature samples after they reached room temperature again show, except for the 300 °C sample, similar values compared to the pre-heating tests. This indicates that the strength drop at elevated temperatures might in fact be material behavior, combined with poor statistics due to the low number of pop-ins observed. The suspiciously low strength for the 300 °C sample might have been further influenced by a wearing indenter tip that caused an increasing radius.

Tantalum: Single Crystalline State

Compared to chromium, tantalum does not show a consistent trend of lowered pop-in loads, especially at temperatures above 100 °C, as shown in Fig. 4.23a. The 100 °C numbers are less scattering compared to those obtained at room temperature. As expected, they show a decreased average pop-in load compared to their room temperature counterparts. The ambiguous numbers at 250 °C and 300 °C are expected to be influenced by the hardening effect described in chapter 5.7.

A further indicator for this suspicion is shown in Fig. 4.23b. While the 100 °C numbers exhibit an increased pop-in excursion at a certain load (which is described by the slope of the curve), compared to room temperature, the 250 °C and 300 °C slopes are decreased. Furthermore, the post high temperature indentation runs expose that only the pop-ins of the 100 °C sample

own a similar behavior in terms of pop-in excursion versus load as those obtained before heating. This might be interpreted as a hindering of the dislocation movement and or multiplication at the actual pop-in event for the 250 °C and 300 °C experiments.

The shear strength at room temperature (Fig. 4.23c) is approximately 8.5 GPa, which is 78 % of the theoretical shear strength. Biener et al. [74] report a shear strength of 7.5 GPa, which is approximately 12 % lower than what was observed in this work. For their experiments a Berkovich indenter with a tip radius of 190 nm was used. The lower tip radius would actually support a higher average shear strength. However, the evaluation of the tip radius with Hertzian contact mechanics is only considering a perfectly spherical tip and is hence an approximation [51]. Since 66 pop-ins were observed for sx tantalum at room temperature prior to high temperature experiments in this work and even over 100 in the work of Biener et al. a major influence due to statistical issues appear not to be the case. It seems therefore more reasonable that the precision of determining the tip radius might have played a major role, contributing to the mismatch between the gained results.

The behavior at elevated temperatures can again be divided into two regions. The 100 °C measurements show a strength decrease of approximately 4 %, which seems reasonable, since the shear strength is not expected to decrease rapidly, as discussed for chromium in a previous section of this chapter. Furthermore, the room temperature indentation of the 100 °C sample after cooling down was exactly the same as those obtained prior to heating. The shear strength at 250 °C is slightly increased to 80 %, the numbers at 300 °C drop to approximately 74 % of the theoretical strength. However, the latter experiments might have been influenced through the diffusion of oxygen into the sample and therefore the possible formation of a thin oxide layer. This is believed, since the hardness decrease at elevated temperatures is not continuous and particularly because of the unexpectedly high shear strengths obtained for the 250 °C and 300 °C samples after high temperature runs. The highest numbers observed where 117 % of the theoretical shear strength. A very pronounced increase of the pop-in load due to the presence of a thin oxide layer was already reported by Bahr et al. [46] for (100) tungsten. In their study, the pop-in load increased in the presence of a 30 Å oxide layer, shown in Fig. 5.23. It is interesting to note, that in their work the scattering of the loads increased after the oxide layer growth, just as it was the case for at least the 300 °C tantalum results in this work.

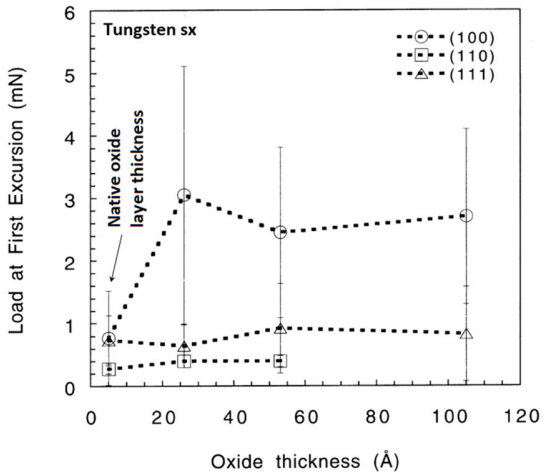

Fig. 5.23: Pop-in load as a function of oxide layer thickness in the case of sx tungsten for different crystallographic planes. Adopted from [46].

5.6.6 Activation Energy

As depicted in Fig. 4.24, Q_a is increased for the sx states, compared to the according ufg materials. Since the Young's modulus is not expected to decrease in a significant manner up to 300 °C and was therefore set constant, this is expected to be a direct consequence of the fact that at low temperatures the athermal flow stress is more distinctively contributing to the overall flow stress in terms of the sx. Close to the critical temperature, where the athermal part of the flow stress of sx is vanishing, Q_a is expected to strongly decrease for sx materials. However, the slight increase of the flow stress, equivalent to a negative Q_a, as exhibited by sx chromium, is physically not meaningful and the result of an unexpectedly high macroscopic flow stress.

Diffusion processes, such as lattice diffusion and grain boundary diffusion, can contribute to plastic deformation, especially at high temperatures and low stress levels. An overview of literature numbers is presented in Table 15.

Table 15: Overview of activation energies for different diffusion types and materials.

Q_a [kJ/mol]	Chromium	Tantalum
lattice diffusion	306 [90]	413 [91]
boundary diffusion	192 [92]	280 [92]

It is evident that the activation energies for diffusional processes are far higher than the approximately 5 – 30 kJ/mol observed in this work. In order to enable further conclusions, the macroscopic hardness numbers used for the calculation of Q_a, are transformed into flow stress values by means of Eq.(2). If the flow stress is treated as an equivalent stress σ_v, and pure shear is assumed, the shear stress σ_s can be estimated with the van Mises criterion, as shown in Eq. (34).

$$6_s = \frac{6_v}{\sqrt{3}} \tag{34}$$

The obtained shear stresses can then be plotted in deformation maps of Frost and Ashby [93] for 0.1 mm grain sized chromium and tantalum, see Fig. 5.24.

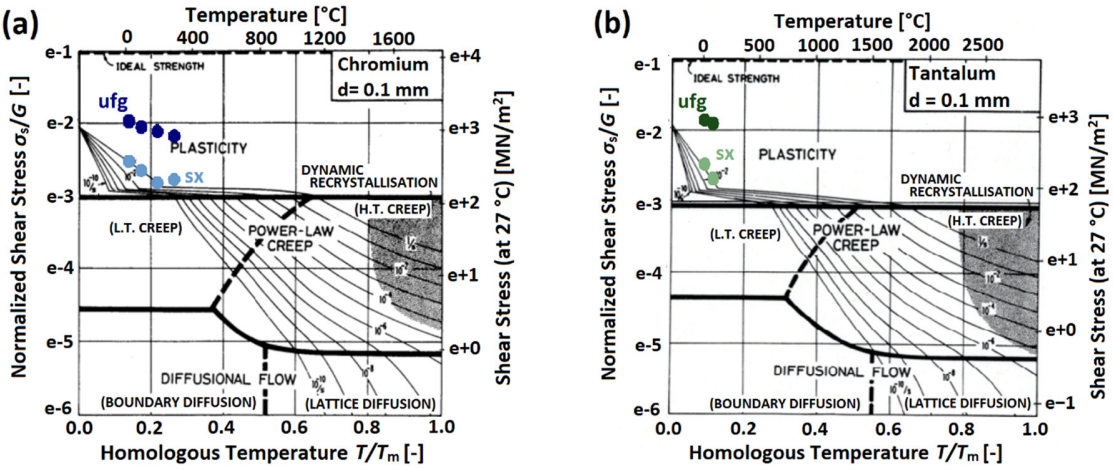

Fig. 5.24: Deformation maps for chromium (a) and tantalum (b) with grain sizes of 0.1 mm including normalized shear stresses obtained in this work. Adopted from [93].

It is evident from these illustrations that all shear stresses are situated in a region of the deformation map denoted as “plasticity”. This part of the deformation map is related with dislocation gliding processes, and far off the areas which are related to diffusion. This is expected from the previously discussed activation energies, since for diffusion much higher Q_a values would be expected. Furthermore, it is interesting to note that the sx shear stress is very well matching those proposed by the according deformation map for high strain rates (≈ 1 s^{-1}). This is expected, since a grain size of 0.1 mm, as presented in Fig. 5.24, is several orders of magnitude closer to the sx, compared to the ufg samples. Since to the best knowledge of the author, no Q_a values related with obstacle or lattice resistance controlled dislocation gliding are reported in literature, it is hard to distinguish between different processes in the “plasiticity” region, based on the calculated activation energies.

5.7 Tantalum Hardening at Elevated Temperatures

5.7.1 General Discussion on the Possible Origins of the Observed Hardening Phenomenon

As it was mentioned various times in this work that, the tantalum samples, both ufg and sx, exhibited a severe hardening phenomenon when temperature was raised up to 250 and 300 °C. Experimental failures such as abrupt area function degradation can be neglected as a possible explanation, since their influence is expected to be less reproducible. Furthermore, tests on non-heated samples led to expected hardness numbers again. Since the observed numbers showed a distinctive temperature dependence the growth of the natural oxygen layer might be cited as a possible explanation. It was already found that for high temperature measurements on this type of nanoindenter oxide growth might occure [94], despite the enabled purging gas system. In the following, a short discussion is given about the reasonability of explaining the observed hardening with the shear growth of the oxygen layer:

Vermilyea [95] reports about oxide growth in 99.5 % pure oxygen atmosphere at temperatures up to 300 °C for 278 hours. Although these are more severe conditions compared to those experiments are conducted at in this work, the oxygen growth is only in the several 10 Å range, as shown in Fig. 5.25a.

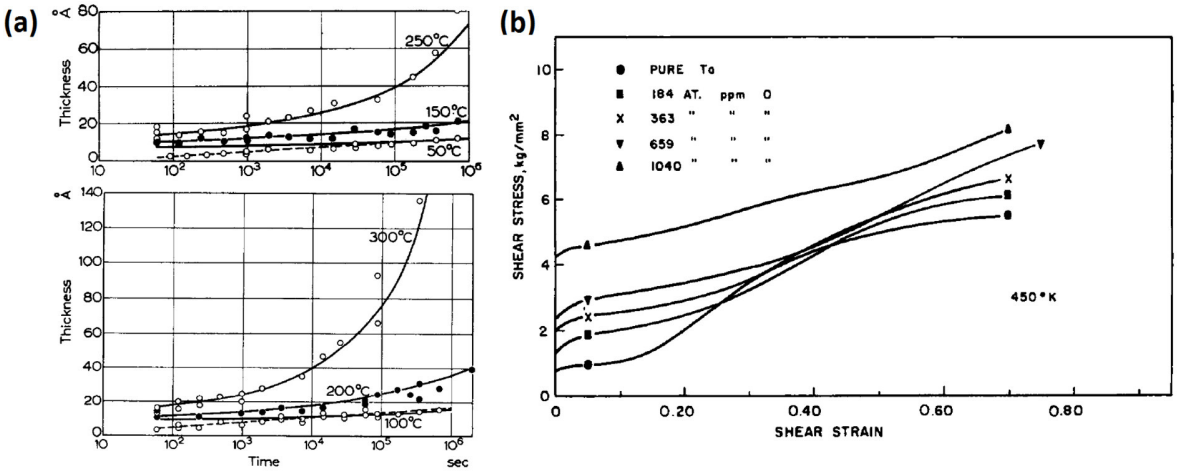

Fig. 5.25: Oxidation behavior of tantalum in 99.5 % 0_2 atmosphere (a) and effect of interstitial solid solution hardening for sx tantalum at 177 °C (b) adopted from [95] and [97], respectively.

Hardness tests conducted on sx tantalum (Fig. 4.12a) furthermore suggest influenced depths of approximately 2000 nm, which is far deeper than a several Å thick oxide layer is expected to influence. Moreover, Dub and Starikov [96] report about tantalum oxide films and find distinctively increased hardness only from 100 nm on. Oxide layers capable of influencing the

hardness in such a distinctive way as observed in this work are expected to be clearly visible when investigating the cross-sections of affected intents. This was not the case, as it is shown in Fig. 5.4b for an indent made on ufg tantalum at 300 °C. Finally, a considerable decrease of the Young's modulus would be expected in the presence of tantalum oxide [74]. This is also not observed as shown in Fig. 4.12b.

Different to the growth of a thick surface oxide layer, the oxygen presence might also lead to a diffusion of oxygen into the sample material, and eventually to solid solution hardening of the tantalum. This might also take place in the case of limited oxygen layer growth, since tantalum-oxide is known to not form dense protective layers [98]. The hardness decline with respect to depth might be an evidence for such a diffusion controlled hardening. In fact, tantalum was used as a reference material in the past to show this mechanism in bcc metals due to its good solubility for nitrogen and oxygen [99]. Furthermore, Schmitz et al. [100] report increased hardness for tantalum coatings exposed to oxygen at 350 °C and 450 °C, whereas Smialek et al. [97] present data showing a shear stress increase by the factor of four at low strains for an oxygen content of 1040 ppm, see Fig. 5.25b. However, all these works have in common that the solution of oxygen in tantalum was accompanied by some effort to gain samples with certain amounts of dissolved oxygen. Different to that Hosemann et al. [101] annealed their tantalum samples at 1200 °C in a vacuum of 10^{-4} Torr increasing the oxygen concentration by approximately 400 ppm. In order to prove solid solution hardening as the primary reason for the hardening observed unequivocally, it would be required to measure the oxygen concentration at different depths. The oxygen concentrations in the literature quoted above are in the 0.1 at.% regime. Common methods to measure the concentration of certain amounts of an element in a sample which are based on physical principles, such as energy dispersive x-ray spectroscopy, do not have sufficient resolution to obtain such low fractions. Alternatively, chemical methods would be capable, but would mean the sacrifice of a sample due to the nature of their working principles.

5.7.2 Modelling of the Hardening Phenomenon

To gain further evidence for or against the possibility of solid solution hardening without conducting additional destructive experiments, the diffusion of oxygen in tantalum was calculated for different temperatures. Subsequently, the hardening at different depths was estimated using the gained oxygen concentration profile and hardening values due to Oxygen incorporation reported by Hosemann et al. [101]. For the calculation itself, some assumptions are made which are summarized in Table 16.

Table 16 : Overview of made assumptions for the diffusion calculation an their corresponding justifications.

assumption	reasoning
• Constant concentration of oxygen in the gas within the chamber	○ volume of the chamber compared to the sample is very high
• Diffusion coefficient is independent from the concentration	○ [102] reports comparable values of the activation energy for different concentrations
• The nature of the diffusion process does not change for different temperatures	○ [102] gives comparable numbers of activation energy for different temperatures
• The hardening is assumed linear correlated with oxygen concentration	○ [99] reports that case for over 1000 ppm oxygen in tantalum

For a constant surface concentration c_R of an arbitrary material, one can assume its equilibrium concentration profile in the neighboring material as described by Eq. (35) [103], where *c* is the concentration at a certain place *x* at a certain time *t,* and *D* is the diffusion coefficient.

$$c = c_R \cdot \operatorname{erfc}\left(\frac{x}{2 \cdot \sqrt{D \cdot t}}\right) \tag{35}$$

The time represents the duration the sample was at the experimental temperature and needs to be considered as an approximationMoreover, the diffusion coefficient *D* is related to its maximum value at infinite temperature D_0, the activation energy of the diffusion process E_A, the absolute temperature *T*, and the ideal gas constant R by Eq. (36).

$$D = D_0 \cdot e^{-(E_A/R \cdot T)} \tag{36}$$

With Eq. (35) and (36), and literature values from Table 17, concentration profiles are plotted for oxygen and nitrogen, since the latter's presence is also known to cause hardening [97]. The results are presented in Fig. 5.26.

Table 17 : Variables and constants used during the diffusion calculations. Numbers referring to oxygen are marked with "O", whereas numbers related to nitrogen are marked with "N".

magnitude	value	unit
t	10	h
D_0	0.0044 (O), 0.0056 (N) [102]	cm^2 / s
E_A	106.483 (O) 158.550 (N) [102]	kJ / mol
R	8.314	J / mol K

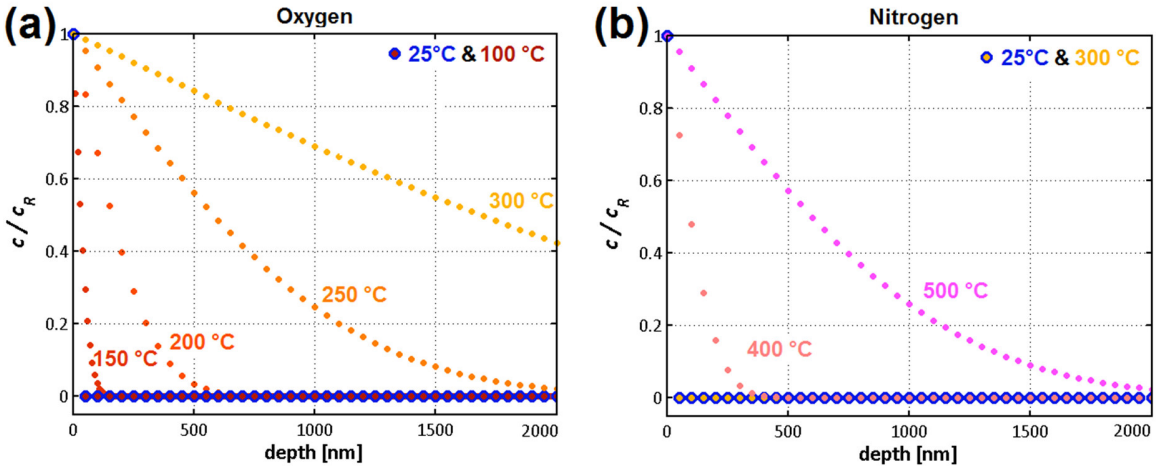

Fig. 5.26: Comparison of the calculated concentration profiles for oxygen (a) and nitrogen (b) after 10 h at room temperature, 100, 200 and 300 °C.

As it can be instantly seen, the higher activation energy of the nitrogen leads to no enrichment on the sample side, with the 10 h measurement period. This is an important finding, since both gases are present in the chamber. However, based on Fig. 5.26b we can exclude Nitrogen for our considerations. The results are even more interesting for oxygen: The calculation predicts the same temperatures for noticeable diffusion processes, where experimental findings suggested hardening behavior, namely 250 °C and 300 °C. Meanwhile, the room temperature and 100 °C curve stay unaffected. However, it needs to be noticed that, according to these calculations, significant diffusion starts already in the 150-200 °C region.

In order to obtain the hardness increase as a function of depth due to oxygen incorporation, only the pre high temperature hardness needs to be subtracted from the one obtained after high temperature experiments. Since experimental hardness numbers are, due to the nature of the nanoindentation technique, situated at different depths, one of the curves needs to be fitted. This is done according to the Nix-Gao-model in this work. An overview of this procedure is presented in Fig. 5.27.

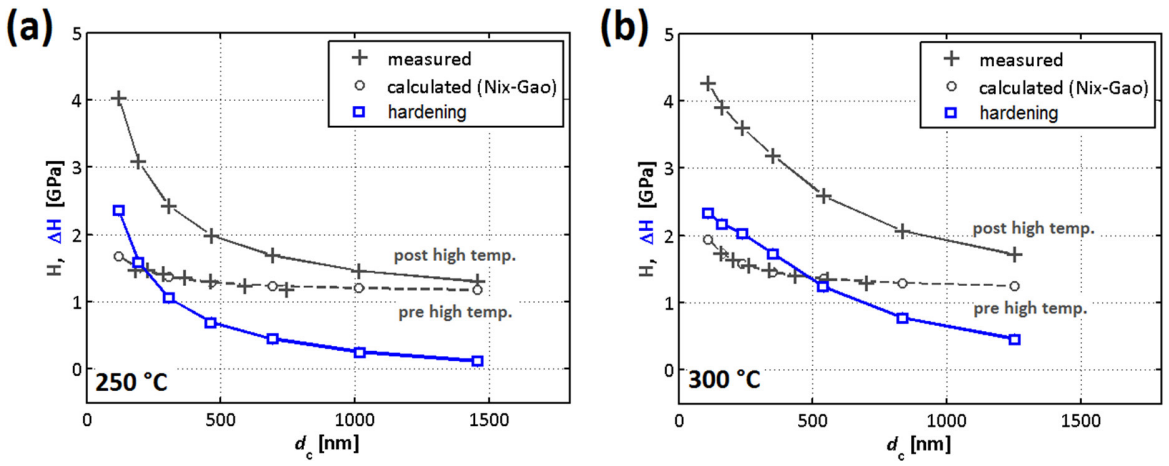

Fig. 5.27: Workflow of gaining the absolute hardness difference between pre and post 250 °C (a) and 300 °C (b) experiments.

If now a law is established to relate the calculated concentration profiles with a hardening or strength increase, one is able to compare calculated with measured hardness increases. As mentioned above, for concentration in the range of 1000 ppm it was found that tantalum hardens in a linear relation with the concentration of oxygen [99]. This relation is also known as Suzuki relation and might be written as

$$\Delta\tau = f \cdot c \tag{37}$$

where $\Delta\tau$ is the increase in strength and f is a correlation factor [104]. However, since this discussion is focused on hardness, $\Delta\tau$ will be treated as hardness increase due to solid solution hardening. Hosemann et al. [101] found a hardness increase of approximately 1 GPa for an oxygen increase of 300 ppm. Using this number enables a concentration estimation, by matching the calculated with the measured hardness increase. The results of this approach are depicted in Fig. 5.28. In order to match the hardness numbers from calculation with those gained by experiments, a concentration of 800 ppm, which is equivalent to 0.08 at.-% was needed. This is close enough to 1000 ppm from whereon a linear relation between hardness and oxygen concentration was assumed. Moreover it is in a concentration range which might have easily remained in the chamber of the nanoindenter. The prediction of the slope differences between the 250 and 300 °C curves, the right prediction of affected temperatures and the explanation for the comparable hardness increases in the case of 250 and 300 °C at low indentation depths between the affected curves are the outstanding features of this comparison. The slight overestimation of the influence depth regarding the 300 °C calculation,

might stem from effects decreasing the effective diffusion coefficient, as the growth of the natural oxide layer, or a lack of thermodynamic equilibrium.

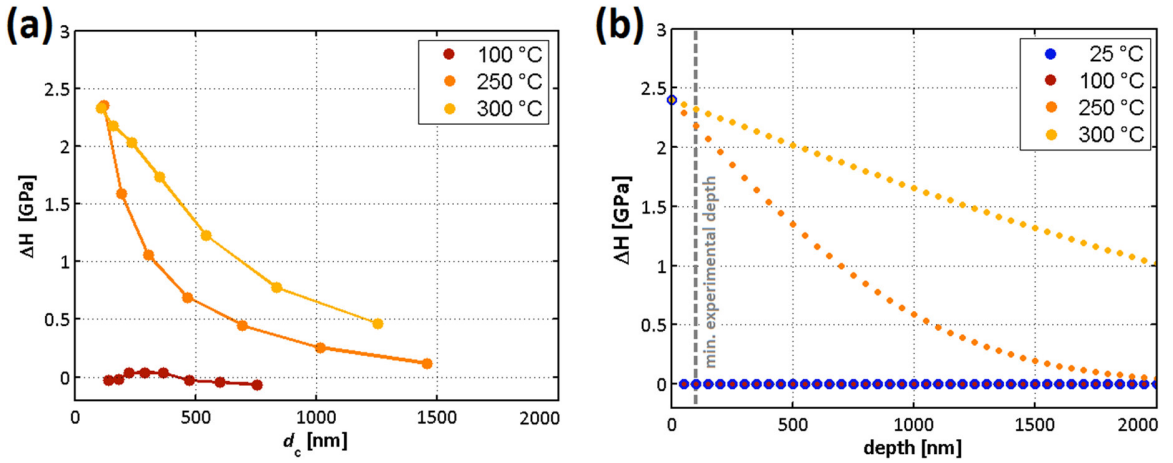

Fig. 5.28: Comparison between the calculated and measured hardening through oxygen diffusion for the input parameters listed in Table 17.

Finally, it is interesting to investigate the time dependence of the experimental results, since these are expected to change due to the diffusion process. The hardness increase with time for at 300 °C for an ufg tantalum sample is shown in Fig. 5.29a. It is evident, that the influence of time is not as strong as that of temperature. This is reasonable, since the temperature is an exponential influence as shown in Eq. (36). A comparison calculation can be found in Fig. 5.29b, which is also predicting only modest increases for the discussed amount of time.

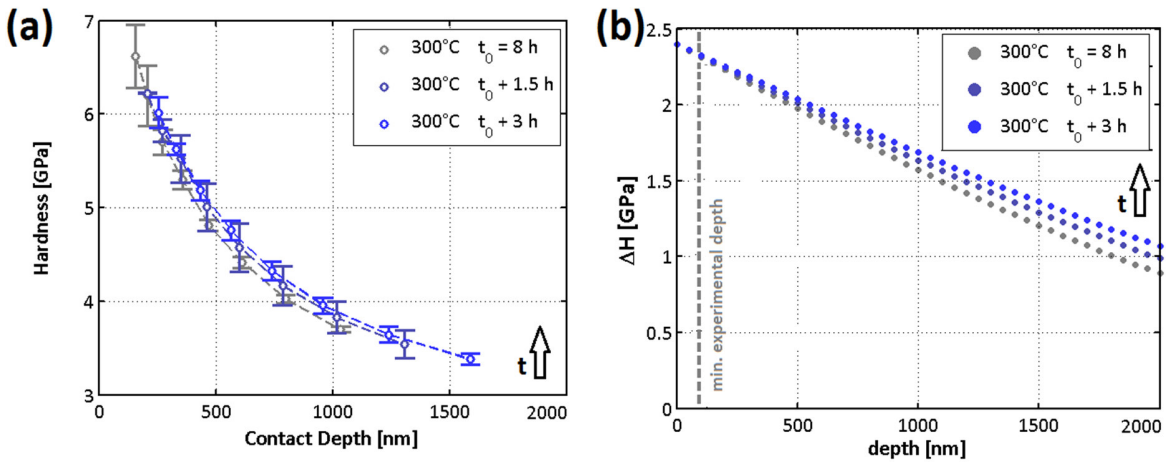

Fig. 5.29: Comparison of measured hardness increase at 300 °C (a) and according calculation results (b).

The proposed model of oxygen diffusion and linear hardening presented in this chapter is capable of predicting hardening trends regarding different temperatures, as well as the

according hardness evolution as a function of time. Therefore, it is concluded that the observed hardening of tantalum samples at temperatures of 250 C and 300 °C are based on the solid solution hardening by oxygen which is supplied by means of diffusion from the chamber atmosphere.

6 Summary and Conclusions

As demonstrated, HPT provides a feasible method to produce chromium and tantalum samples in the transition between ufg and nc microstructure (≈ 100 nm) from sx starting material. Nanoindentation measurements revealed that grain refinement and plastic deformation introduced by this process increased the hardness of these materials by a factor of approximately 3.5-4 at room temperature. Hardness and creep experiments were also conducted at temperatures up to 300 °C, whereas all tantalum samples showed a severe hardening phenomenon from 250 °C on and were therefore precluded from the ordinary analysis procedure. The chromium and remaining tantalum data at elevated temperatures revealed a general hardness decreases with increasing temperature. The behavior of the ufg and sx samples differed in such a way that the sx materials hardness decline stopped at the assumed critical temperature, whereas that of the ufg sample further decreased. From this observation it is concluded that additional to the Peierls stress for the sx, the ufg owns further contributors to the flow stress which are thermally activatable, such as grain boundary interactions.

The analysis of the ISE showed that all ufg materials have h^* numbers well below 100 nm which is typical for this grain size regime. However, h^* for the sx samples seemed to be underestimated at least in the case of chromium, also being < 100 nm at room temperature. This mismatch to the higher numbers found in literature for sx and cg materials is concluded to be the result of to less or the absence of data points in the low (< 200 nm) and high depth (> 1000 nm) regime. At elevated temperatures ufg microstructures were obtained to show an increased h^*. This is except for the chromium sx at 300 °C, which is decreased compared to the 200 °C measurements. At least the majority of literature available reports an increasing h^* with increasing temperature for bcc samples up to T_c, matching the trend observed in this work. However, no literature is available for the ISE above T_c or for ufg materials, which is why the according numbers cannot be directly compared.

The Young's moduli obtained with hardness measurements were at room temperature independent from depth and the comparison with literature revealed a good agreement, with a mismatch of less than 10 %. However, at elevated temperatures the Young's moduli became depth dependent in some cases, leading to unexpectedly low numbers at high depths. This

phenomenon was attributed to compliance issues arising from the mounting method used. It was furthermore shown, that this has no significant effect on the corresponding hardness numbers.

The creep experiments, conducted at room temperature affirmed the expected decreased SRS for the ufg compared to the sx microstructural states. It is concluded that this difference directly merges from the increased hardness of the ufg materials, not by a change of the primary deformation mechanism. This opinion is based on the very similar V^* numbers observed for ufg and sx material at room temperature, which are in the range known for kink-pair nucleation, as it is general expected for bcc materials . The decrease of the SRS for chromium and tantalum sx at 100 °C is expected as well, since the thermal, compared to the athermal part of the flow stress is strongly decreasing towards T_c and no contributions from grain boundaries are feasible. However, the increase of SRS at temperatures above 100 °C for the sx states is physically unexpected and assumed to be related to thermal drift. The continuous SRS increase in case of the ufg materials can be explained by the contribution of grain boundary interactions, leading to higher thermal flow stresses though the contribution of the Peierls stress is, just as for the sx, strongly decreasing with temperature. Despite that, the ufg SRS numbers at elevated temperatures are comparably high and are hence also assumed to be influenced by thermal drift.

Incipient plasticity was investigated for the sx samples and the according shear stress was found to be a substantial part of the theoretical stress for chromium and tantalum, respectively. Due to the wide range of pop-in loads and hence maximum shear stresses observed at room and at elevated temperatures, it might be concluded that the comparably high tip radius of approximately 450 nm enabled different mechanisms causing plasticity, such as homogenous and heterogeneous dislocation nucleation and the activation of preexistent dislocations. The expected continuous decrease of the maximum shear stress with temperature was only obtained for the chromium sx, though the decrease might be overestimated. The maximum shear stress trend at elevated temperatures in case of the tantalum sx was of more complex, even depicting numbers above the theoretical shear strength. This behavior is concluded to merge from the growth of a very thin (< 50 nm) oxide layer on the surface of the sample tantalum sx sample.

Annealing experiments on chromium ufg, as well as cross section investigations on chromium and tantalum 300 °C do not reveal a significant growth of the microstructure after the treatments. However, the mentioned chromium samples might have been subject to slight grain growth, which is, due to the matching hardness numbers compared to pre high temperature experiments, concluded to have not influenced the measurements in a substantial manner. Regarding the cross sections, no visible oxygen layer was found on room or high temperature samples of chromium or tantalum.

AFM mode measurements conducted on the nanoindentation system depicted substantial piling-up for the ufg as well as for the sx materials at room temperature. Light microscopy studies of the residual indents for all materials at all indents were used to calculate a ratio between the optically measured plastic area and the one gained by the according load-displacement curve. It revealed that from a pile-up trend at room temperature, the behavior is changing to a more sink-in like appearance. The shape of the pile-ups itself was found to be distinctive for ufg and sx materials. Whereas the ufg material piled-up in an elliptical shape in the vicinity of each side of the residual triangular indent, the sx showed a very noticeable orientation dependent piling-up behavior. This led to four pile-ups around the residual indent, corresponding to the slip system {110} ⟨111⟩, instead of three as observed for the ufg microstructure.

The tantalum hardening at temperatures from 250 °C on, is concluded to be the result of oxygen diffusion causing solid solution hardening, which explains the vanishing influence towards higher indentation depths. This oxygen diffusion into the material is further concluded to have taken place simultaneously with a gentle growth of the natural oxygen layer on the surface explaining the increased pop-in loads observed at the onset of plasticity of the according 250 and 300 °C tantalum samples. A diffusion calculation of oxygen into tantalum, coupled with an assumed linear hardening behavior was found to match the described behavior very properly, estimating a residual oxygen concentration of approximately 800 ppm.

It has been the attempt of this work to verify the source of unexpected results when they occurred. One of the major experimental issues was thermal drift, especially influencing the obtained creep data. A possibility to minimize such issues is the use of a constant stiffness measurement system, obtaining the true indentation depth continuously [41]. However, another way is to switch to experimental approaches less susceptible to thermal drift due to the absence of long dwell times, such as nanoindentation jump tests [60]. Another severe drawback of common nanoindentation systems is that they only provide a purging gas system instead of working in vacuum. However, this proves testing materials susceptible to oxidation or diffusion at least challenging if not impossible.

Appendix

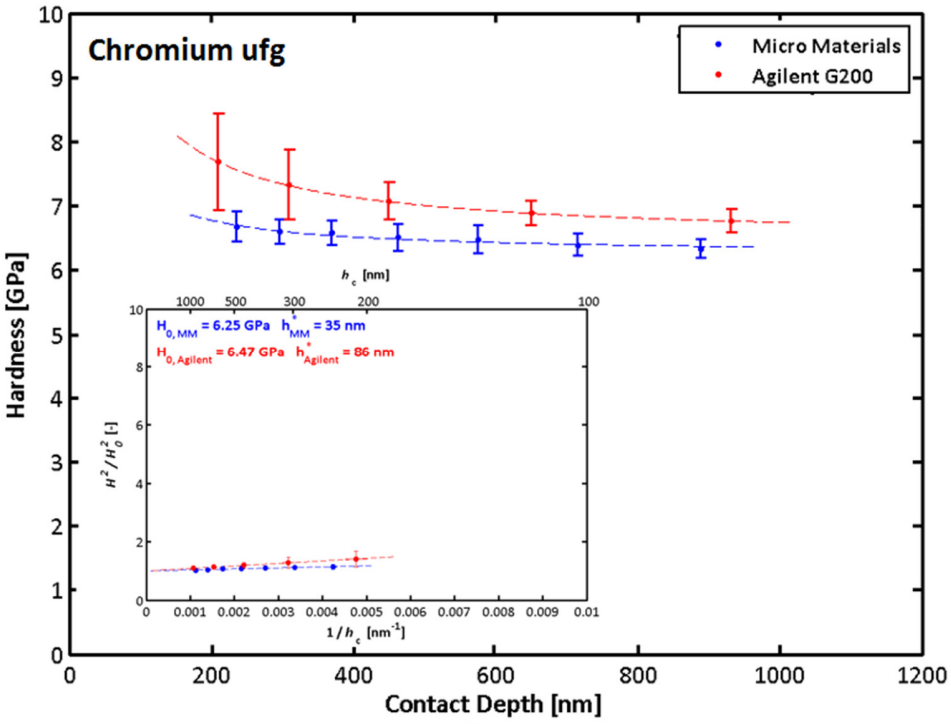

Fig. A.1: Comparison of ufg chromium experimental results gained by the Micro Materials and the Agilent G200 nanoindentation systems.

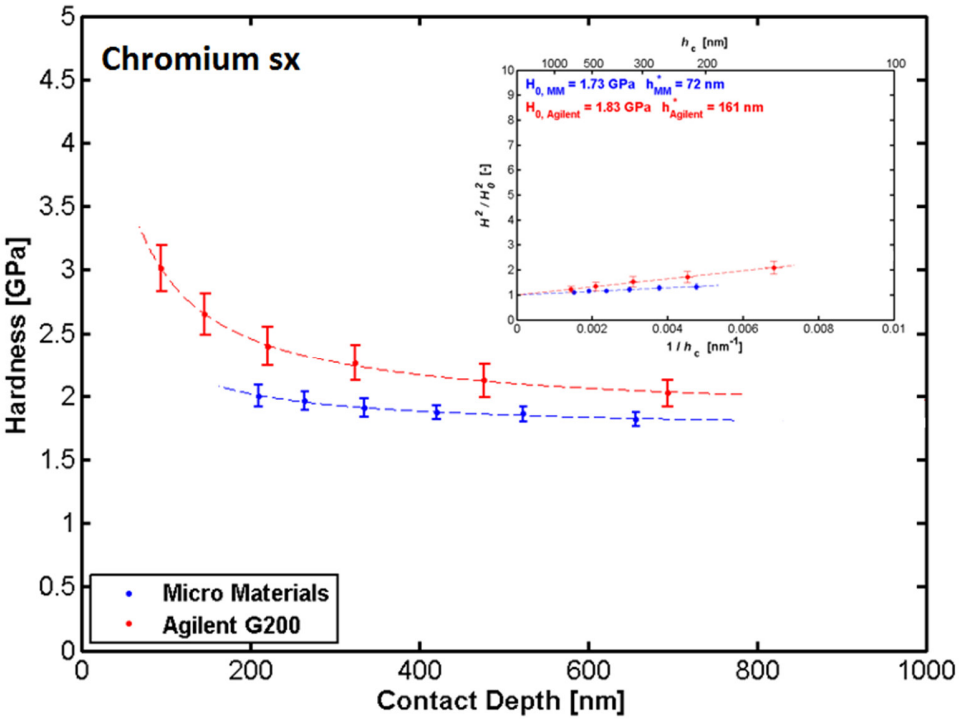

Fig. A.2: Comparison of sx chromium experimental results gained by the Micro Materials and the Agilent G200 nanoindentation systems.

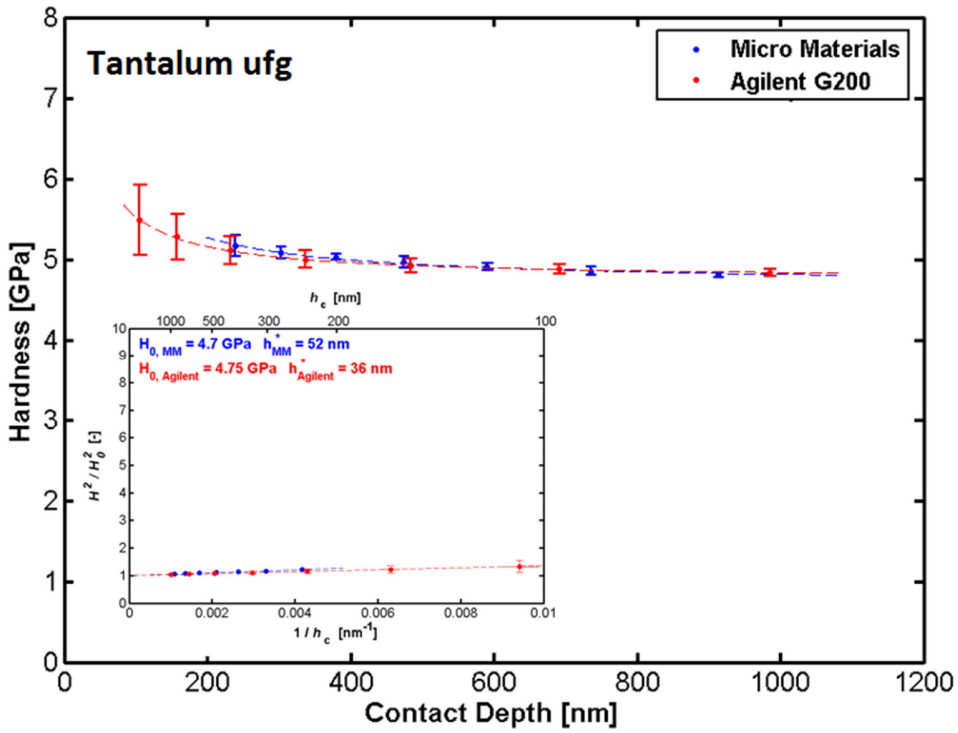

Fig. A.3: Comparison of ufg tantalum experimental results gained by the Micro Materials and the Agilent G200 nanoindentation systems.

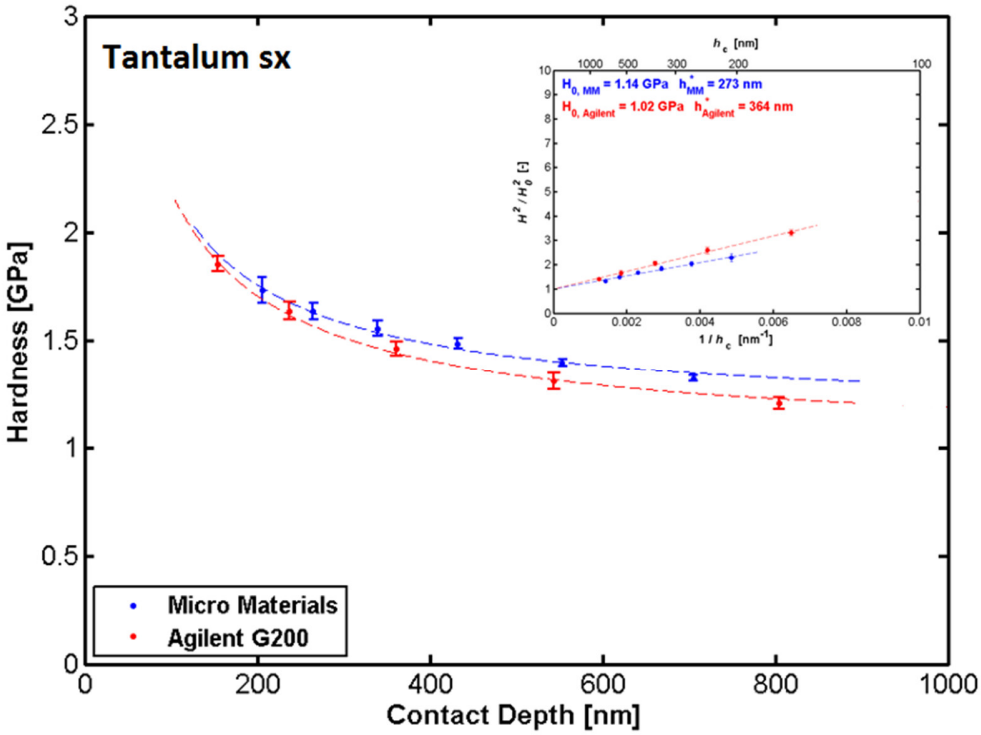

Fig. A.4: Comparison of sx tantalum experimental results gained by the Micro Materials and the Agilent G200 nanoindentation systems.

References

[1] J. Rößler, H. Harders and M. Bäker, Mechanisches Verhalten der Werkstoffe, B. G. Teubner, 2006.

[2] R. Z. Valiev, A. P. Zhilyaev and T. G. Langdon, Bulk Nanostructured Materials: Fundamentals and Applications, John Wiley & Sons, Inc, 2014.

[3] C. Sun, K. Y. Yu, J. H. Lee, Y. Liu, H. Wang, L. Shao, S. A. Maloy, K. T. Hartwig and X. Zhang, "Enhanced radiation tolerance of ultrafine grained Fe-Cr-Ni alloys," *Journal of Nuclear Materials,* vol. 420, pp. 235-240, 2012.

[4] K. Y. Yu, Y. Liu, C. Sun, H. Wang, L. Shao, E. G. Fu and X. Zhang, "Radiation damage in helium ion irradiated nanocrystalline Fe," *Journal of Nuclear Materials,* vol. 425, pp. 140-146, 2012.

[5] M. J. Zehetbauer and Y. T. Zhu, Bulk Nanostructured Materials, WILEY-VCH Verlag GmbH & Co. KGaA.

[6] A. Schneider, D. Kaufmann, B. Clark, C. Frick, P. Gruber, R. Mönig, O. Kraft and E. Arzt, "Correlation between Critical Temperature and Strength of Small-Scale bcc Pillars," *Physical Review Letters,* vol. 103, 2009.

[7] V. Maier, A. Hohenwarther, R. Pippan and D. Kiener, "Thermally activated deformation processes in body-centered cubic Cr – How microstructure influences strain-rate sensitivity," *Scripta Materialia,* vol. 106, pp. 42-45, 2015.

[8] E. Hornbogen, Werkstoffe - Aufbau und Eigenschaften von Keramik-, Metall-, Polymer- und Verbundwerkstoffen, Springer, 2006.

[9] A. Atkins and D. T. Plastic, "Plastic indentation in metals with cones," *Journal of the Mechanics and Physics of Solids,* vol. 13(3):149–164, 1965.

[10] K. L. Johnson, *Contact Mechanics. Cambridge University Press,* 1985.

[11] N. Petch, *J Iron Steel Inst,* vol. 174:25, 1953.

[12] E. Hall, *Proc Soc London,* vol. B64:747, 1951.

[13] N. Hansen, "Hall–Petch relation and boundary strengthening," *Scripta Materiala,* vol. 801–806, 2004.

[14] T. Volpp, E. Göring, W.-M. Kuschke and E. Arzt, "Grain Size Determination and Limits to Hall-Petch Behavior in Nanocrystalline NiAl Powders," *NanoStructured Materials,* pp. 855-866, 1997.

[15] C. E. Carlton and P. J. Ferreira, "What is behind the inverse Hall–Petch effect," *Acta Materialis,* p. 3749–3756, 2007.

[16] A. H. Chokshi, A. Rosen, J. Karch and H. Gleiter, "On the validity of the hall-petch relationship in nanocrystalline materials," *Scripta Metallurgica,* p. 1679–1683, 1989.

[17] V. Maier, C. Schunk and M. D. K. Göken, "Microstructure-dependent deformation behaviour of bcc-metals - indentation size effect and strain rate sensitivity," *Philosophical Magazine,* 2014.

[18] "www.plansee.com," [Online]. Available: http://www.plansee.com/de/Werkstoffe-Chrom-939.htm. [Accessed 6 11 2014].

[19] J. May, H. W. Höppel and M. Göken, "Strain rate sensitivity of ultrafine-grained aluminium processed by severe plastic deformation," *Scripta Materiala,* p. 189–194, 2005.

[20] Q. Wei, Z. L. Pan, X. L. Wu, B. E. Schuster, L. J. Kecskes and R. Z. Valiev, "Microstructure and mechanical properties at different length scales and strain rates of nanocrystalline tantalum produced by high-pressure torsion," *Acta Materialia,* vol. 59, pp. 2423-2436, 2011.

[21] D. Wu, X. L. Wang and T. G. Nieh, "Variation of strain rate sensitivity with grain size in Cr and other body-centred cubic metals," *Journal of Physics D: Applied Physics,* vol. 47, 2014.

[22] V. Maier, "Verformungsverhalten von ultrafeinkörnigen Metallen untersucht mittels neu entwickelter Nanoindentierungsmethoden," *PhD Thesis,* 2013.

[23] Q. Wei, S. Cheng, K. T. Ramesh and E. Ma, "Effect of nanocrystalline and ultrafine grain sizes on the strain rate," *Materials Scienece & Engineering A,* vol. 381, pp. 71-79, 2004.

[24] W. D. Nix and H. Gao, "Indentation Size Effects in Crystalline Materials: A Law for Strain Gradient Plasticity," *1998,* vol. 46, no. 3, pp. 411-425, J. of Mech. Phys. Solids.

[25] Y. Huang, F. Zhang, K. Hwang, W. Nix, G. Pharr and G. Feng, "A model of size effects in nano-indentation," *Journal of the Mechanics and Physics of Solid,* p. 1668–168, 2006.

[26] A. S. Schneider, C. P. Frick, B. G. Clark, P. A. Gruber and E. Arzt, "Influence of orientation on the size effect in bcc pillars with different critical temperatures," *Materials Science & Engineering A,* vol. 528, pp. 1540-1547, 2011.

[27] H. Yuan, J. Chen, K. Krompholz and F. H. Wittmann, "Investigation of size effects in tensile tests based on a nonlocal micro-mechanical damage model," *Computational Materials Science,* vol. 26, pp. 230-243, 2003.

[28] T. R. Malow, C. C. Koch, P. Q. Miraglia and K. L. Murty, "Compressive mechanical behavior of naocrystalline Fe investigated with an automated ball indentation technique," *Materials Science and Engineering A,* vol. 252, pp. 36-43, 1998.

[29] A. Vorhauer and R. Pippan, "On the homogenity of defomration by high pressure torsion," *Scripta Materialia,* vol. 51, no. 9, pp. 921-925, 2004.

[30] T. Hebesberger, H. Stüwe, A. Vorhauer, F. Wetscher and R. Pippan, "Structure of Cu deformed by high pressure torsion," *Acta Materialia,* vol. 53, pp. 393-402, 2005.

[31] A. P. Zhilyaev and T. G. Langdon, "Using high-pressure torsion for metal processing: Fundamentals and applications," *Progress in Materials Science,* vol. 53, pp. 893-979, 2008.

[32] A. P. Zhilyaev, G. V. Nurislamova, B.-K. Kim, M. D. Baro, J. A. Szpunar and T. G. Landon, "Experimental parameters influencing grain refinement and microstructural evolution during high-pressure torsion," *Acta Materialia,* vol. 51, pp. 753-765, 2003.

[33] A. P. Zhilyaev, S. Lee, G. V. Nurislamova, R. Z. Valiev and T. G. Langdon, "Microhardness and Microstructural Evolution in Pure Nickel during High-Pressure Torsion," *Scripta Materialia,* vol. 44, pp. 2753-2758, 2001.

[34] H.-J. Bargel and G. Schulze, Werkstoffkunde, Berlin: Springer-VDI-Verlag, 2005.

[35] A. C. Fischer-Cripps, Nanoindentation, Springer Science+Business Media New York, 2002.

[36] B. N. Lucas, "PhD. Thesis An Experimental Investigation of Creep and Viscoelastic Properties Using Depth-Sensing Indentation Techniques," *University of Tennessee, Knoxville,* 1997.

[37] W. C. Oliver and G. M. Pharr, "An improved technique for determining hardness and elastic modulus using load and displacement sensing indentation experiments," *Journal of Materials Research,* vol. 7, no. 6, pp. 1564-1583, 1992.

[38] N. M. Everitt, M. I. Davies and J. F. Smith, "High temperature nanoindenation - the importance of isothermal contact," *Philosophical Magazine,* vol. 91, pp. 1221-1244, 2010.

[39] K. R. Gadelrab, F. A. Bonilla and M. Chiesa, "Densification modeling of fused silica under nanoindentation," *Journal of Non-Crystalline Solids,* pp. 392-398 , 2012.

[40] M. J. Mayo, R. W. Siegel, A. Narayanasamy and W. D. Nix, "Mechanical properties of nanophase TiO2 as determined by nanoindentation," *Journal of Materials Research,* pp. 1073-1082, 1990.

[41] V. Maier, M. Benoit, M. Göcken and K. Durst, "An improved long-term nanoindentation creep testing approach for studying the local deformation processes in nanocrystalline metals at room and elevated temperatures," *Journal of Materials Research ,* vol. 28, no. 9, pp. 1177-1188, 2013.

[42] D. Peykov, M. Etienne, R. R. Chromik, R. Gauvin and M. Trudeau, "Evaluation of strain rate sensitivity by constant load nanoindentation," *Journal of Materials Science,* vol. 47, no. 20, pp. 7189-7200, 2012.

[43] H. Li and A. H. W. Ngan, "Size effect of nanoindentation creep," *Journal of Materials Research,* vol. 19, no. 2, pp. 513-522, 2004.

[44] O. Sherby and P. Armstrong, "Prediction of Activation Energies for Creep and Self-Diffusion from Hot Hardness Data," *Metallurgical Transactions ,* vol. 2, 1971.

[45] J. Wheeler, V. Maier, K. Durst, M. Göken and J. Michler, "Activation parameters for deformation of ultrafine-grained aluminium as determined by indentation strain rate jumps at elevated temperatures," *Materials Science & Engineering A,* pp. 108-113, 2013.

[46] D. F. Bahr, D. E. Kramer and W. W. Gerberich, "Non-linear deformation mechanism during nanoindentation," *Acta Materialia,* vol. 46, no. 10, pp. 3605-3617, 1998.

[47] Y. L. Chiu and A. H. W. Ngan, "Time-dependent characteristics of incipient plasticity in nanoindenation of a Ni3Al single crystal," *Acta Materialia,* vol. 50, pp. 1599-1611, 2002.

[48] J. K. Mason, A. C. Lund and C. A. Schuh, "Determining the activation energy and volume for the onset of plasticity during nanoindentation," *Physical Review B,* vol. 73, 2006.

[49] S. Shim, H. Bei, E. George and G. Pharr, "A different type of indentation size effect," *Scripta Materialia,* p. 1095–1098, 2008.

[50] D. Wu, J.R. Morris and T. G. Nieh, "Effect of tip radius on the incipient plasticity of chromium studied by nanoindentation," *Scripta Materialia,* vol. 94, pp. 52-55, 2015.

[51] H. Bei, E. P. George, J. L. Hay and G. M. Pharr, "Influence of Indenter Tip Geometry on Elastic Deformation during Nanoindentation," *Physical Review Letters,* 2005.

[52] "Kaye&Laby - Tables of Physical & Chemical Constants," NPL - National Physical Laboratory, 2015. [Online]. Available: www.kayelaby.npl.co.uk. [Accessed 2015].

[53] K. Kese and Z. C. Li, "Semi-ellipse method for accounting for the pile-up contact area during nanoindentation with the Berkovich indenter," *Acta Materialia,* vol. 55, pp. 699-702, 2006.

[54] Y. H. Lee, J. H. Hahn, S. H. Nahm, J. I. Jang and D. Kwon, "Investigations on indentation size effects using a pile-up corrected hardness," *Journal of Physics D,* vol. 41, 2008.

[55] F. J. Humphreys, "Review - Grain and subgrain characterisation by electron backscatter diffraction," *Journal of Materials Science,* vol. 36, pp. 3833-3854, 2001.

[56] R. Bürgel, Handbuch der Hochtemperatur-Werkstofftechnik: Grundlagen, Werkstoffbeanspruchung, Hochtemperaturlegierungen und -beschichtungen, Vieweg+Teubner Verlag, 2006.

[57] J. M. Wheeler and J. Michler, "Invited Article: Indenter materials for high temperature nanoindentation," *Review of Scientific Instruments,* vol. 84, p. , 2013.

[58] B. Sestak and A. Seeger, "Gleitung und Verfestigung in kubisch-raumzentrierten Metallen und Legierungen," *Zeitschrift für Metallkunde ,* vol. 69, pp. 195-202, 1978.

[59] A. Schneider, D. Kaufmann, B. Clark, C. Frick, P. Gruber, R. Mönig, O. Kraft and E. Arzt, "Correlation between Critical Temperature and Strength of Small-Scale bcc Pillars," *Physical Review Letters,* pp. 105501 1-4, 2009.

[60] V. Maier, K. Durst, J. Mueller, B. Backes, H. Höppel and M. Göken, "Nanoindentation strain-rate jump tests for determining the local strain-rate sensitivity in nanocrystalline Ni and ultrafine-grained Al," *Journal of Materials Research,* vol. 26, pp. 1421-1430, 2011.

[61] A. Hohenwarter, A. Bachmaier, B. Gludovatz, S. Scheriau and R. Pippan, "Technical parameters affecting grain refinement by high pressure torsion," *International Journal of Materials Research,* pp. 1653-1661, 2009.

[62] S. Lee and Z. Horita, "High-Pressure Torsion for Pure Chromium and Niobium," *Materials Transactions,* vol. 53, no. 1, pp. 38-45, 2012.

[63] B. G. Rathmayr and R. Pippan, "Influence of impurities and deformation temperature on the saturation microstructure and ductility of HPT-deformed nickel," *Acta Materialia,* vol. 59, pp. 7228-7240, 2011.

[64] K. Edalati and Z. Horita, "Correlation of Physical Parameters with Steady-State Hardness of Pure Metals Processed by High-Pressure Torsion," *Materials Science Forum,* Vols. 667-669, pp. 683-688, 2011.

[65] V. Provenzano, R. Valiev, D. G. Rickerby and G. Valdre, "Mechanical Properties of Nanostructured Chromium," *Nanostructured Materials ,* vol. 12, pp. 1103-1108, 1999.

[66] R. Wadsack, R. Pippan and B. Schedler, "Structural refinement of chromium by severe plastic deformation," *Fusion Engineering and Design,* Vols. 66-68, pp. 265-269, 2003.

[67] E. McCafferty, Inctroduction to Corrosion Science, 2010, Springer New York.

[68] C.A. Volkert and A.M. Minor, "Focused Ion Beam Microscopy and Micromachining," *MRS Bulletin,* vol. 32, pp. 389-399, 2007.

[69] B. Beake and J. Smith, "High-temperature nanoindentation testing of fused silica and other materials," *Philosophical Magazine A,* pp. 2179-2186, 2002.

[70] W.C. Oliver and G.M. Pharr, "Measurement of hardness and elastic modulus by instrumented indentation: Advances in understanding and refinements to methodology," *Journal of Materials Research,* pp. 3-20, 2004.

[71] K. Kese, Z. Li and B. Bergmann, "Method to account for true contact area in soda-lime glass during nanoindentation with the Berkovich tip," *Materials Science and Engineering A,* pp. 1-8, 2005.

[72] Y. Wang, D. Raabe, C. Klüber and F. Roters, "Orientation dependence of nanoindentation pile-up patterns and of nanoindentation microtextures in copper single crystals," *Acta Materialia,* p. 2229–2238, 2004.

[73] M. Laurent-Brocq, E. Bejanin and Y. Champion, "Influence of Roughness and Tilt on Nanoindentation Measurements: A Quantitative Model," *Scanning ,* pp. 1-11, 2015.

[74] M. M. Biener, J. Biener, A. M. Hodge and A. V. Hamza, "Dislocation nucleation in bcc Ta single crystals studied by nanoindentation," *Physical Review B,* vol. 76, pp. 98-121, 2007.

[75] S. Kucharski and D. Jarzabek, "Depth Dependence of Nanoindentation Pile-Up Patterns in Copper Single Crystals," *Metallurgical and Materials Transactions A,* pp. 4997-5008, 2014.

[76] J. Swadener, E. George and G. Pharr, "The correlation of the indentation size effect measured with indenters of various shapes," *Journal of the Mechanics and Physics of Solids,* pp. 681-694, 2002.

[77] R. Valiev, R. Islamgaliev and I. Alexandrov, "Bulk nanostructured materials from severe plastic deformation," *Progress in Materials Science,* vol. 45, pp. 103-189, 2000.

[78] I. Sabirov, Y. Estrin, M. Barnett, I. Timokhina and P. Hodgson, "Tensile deformation of an ultrafine-grained aluminium alloy: Micro shear banding and grain boundary sliding," *Acta Materialia,* vol. 56, p. 2223–2230, 2008.

[79] A. Vinogradov, S. Hashimoto, V. Patlan and K. Kitagawa, "Atomic force microscopic study on surface morphology of ultra-fine grained materials after tensile testing," *Materials Science and Engineering A,* Vols. 319-321, p. 862–866, 2001.

[80] O. Franke, J. Trenkle and C. Schuh, "Temperature dependence of the indentation size effect," *Journal of Materials Research,* pp. 1225-1229, 2010.

[81] S.-W. Lee, L. Meza and J. Greer, "Cryogenic nanoindentation size effect in [0 0 1]-oriented face-centered cubic and body centered cubic single crystals," *Applied Physics Letters,* pp. 101906 1-5, 2013.

[82] A. Schneider, C. Frick, E. Arzt, W. Clegg and S. Korte, "Influence of test temperature on the size effect in molybdenum small-scale compression pillars," *Philosophical Magazine Letters,* pp. 331-338, 2013.

[83] G. Cheng, W. Jian, W. Xu, H. Yuan, P. Millett and Y. Zhu, "Grain Size Effect on Deformation Mechanisms of Nanocrystalline bcc Metals," *Materials Research Letters,* pp. 26-31, 2013.

[84] Q. Wei, "Strain rate effects in the ultrafine grain and nanocrystalline regimes—influence on some constitutive responses," *Journal of Materials Science,* p. 1709–1727, 2007.

[85] V. Maier, A. Leitner, R. Pippan and D. Kiener, "Thermally activated deformation behavior of ufg-Au - environmental issues during long-term and high temperature nanoindentation testing," *The Journal of The Minerals, Metals & Materials Society,* 2015.

[86] M. Cordill, N. Moody and W. Gerberich, "The role of dislocation walls for nanoindentation to shallow depths," *International Journal of Plasticity,* vol. 25, p. 281–301, 2009.

[87] K. V. Rajulapati, M. M. Biener, J. Biener and A. M. Hodge, "Temperature dependence of plastic flow behavior of tantalum," *Philosophical Magazine Letters,* vol. 90, no. 1, pp. 35-42, 2010.

[88] D. Wu and T. Nieh, "Incipient plasticity and dislocation nucleation in body-centered cubic chromium," *Materials Science & Engineering A,* vol. 609, pp. 110-115, 2014.

[89] C. Zhu, Z. Lu and T. Nieh, "Incipient plasticity and dislocation nucleation of FeCoCrNiMn high-entropy alloy," *Acta Materialia,* vol. 61, pp. 2993-3001, 2013.

[90] W. Hagel, "Self-Diffusion in solid chromium," *Trans. AIME,* vol. 22, p. 430, 1962.

[91] R. Pawel and T. Lundy, "The diffusion of Nb95 and Ta182 in tantalum," *Journal of Physics and Chemistry of Solids,* vol. 26, no. 6, pp. 937-942, 1965.

[92] A. Brown and M. Ashby, "Correlations for diffusion constants," *Acta Metallurgica,* vol. 28, no. 8, pp. 1085-1101, 1980.

[93] H. Frost and M. Ashby, Deformation-Mechanism Maps, The Plasticity and Creep of Metals and Ceramics, Oxford, UK: Pergamon Press,, 1982.

[94] M. Kreuzeder, M.-D. Abad, M.-M. Primorac, P. Hosemann, V. Maier and D. Kiener, "Fabrication and thermo-mechanical behavior of ultra-fine porous copper," *Journal of Materials Science,* p. 634–643, 2014.

[95] D. A. Vermilyea, "The oxidation of tantalum at 50-300°C," *Acta Metallurgica,* vol. 6, no. 3, pp. 166-171, 1958.

[96] S. Dub and V. Starikov, "Elasticity module and hardness of niobium and tantalum anode oxide films," *Functional Materials ,* pp. 347-350, 2007.

[97] R. L. Smialek and T. E. Mitchell, "Interstitial Solution Hardening in Tantalum Single Crystal," *Philosophical Magazine,* vol. 22, no. 180, pp. 1105-1127, 1970.

[98] R. Bürgel, H. Maier and T. Niendorf, Handbuch Hochtemperatur- Werkstofftechnik, Vieweg+Teubner Verlag, 2011.

[99] J. Puhr-Westerheid and C. Elssner, "On the solid solution hardening of tantalum by nitrogen and oxygen," *Journal of Less-Common Metals,* vol. 20, pp. 371-374, 1970.

[100] T. Schmitz, C. Hertl, E. Werner, U. Gburek, J. Groll and C. Moseke, "Oxygen diffusion hardening of tantalum coatings on cp-titanium for biomedical applications," *Surface & Coatings Technology,* vol. 216, pp. 46-51, 2013.

[101] P. Hosemann, S. A. Maloy, R. R. Greco and J. G. R. T. Swadener, "Oxygen effects on irradiated tantalum alloys," *Journal of Nuclear Materials,* vol. 384, pp. 25-29, 2009.

[102] N. L. Peterson, "Diffusion in Refractory Metals," Air Research and Development Command, United States Air Force, 1961.

[103] J. Crank, The Mathematics of Diffusion, Oxford University Press, 1979.

[104] I. Wesemann, A. Hoffmann, T. Mrotzek and U. Martin, "Investigation of Solid Solution Hardening in Molybdenum Alloys," 17th Plansee Seminar 2009, 2009.

[105] Q. Wei, T. Jiao, S. Mathaudhu, E. Ma, K. Hartwig and K. Ramesh, "Microstructure and mechanical properties of tantalum after equal channel angular extrusion," *Materials Science and Engineering A,* pp. 266-272, 2003.